

**High Transverse Momentum
 π^0 Production from π^- and p beams
at 530 GeV/c on Be and Cu**

by

John Philip Mansour

Submitted in Partial Fulfillment
of the
Requirements for the Degree

DOCTOR OF PHILOSOPHY

Supervised by: Professor Thomas Ferbel

Department of Physics and Astronomy
College of Arts and Sciences

University of Rochester
Rochester, New York

1989

CURRICULUM VITAE

John Philip Mansour

The author was born in Woburn, Massachusetts on May 13, 1961. He attended Worcester Polytechnic Institute where he received his Bachelor of Science degree in Physics. At WPI he was nominated to Sigma Pi Sigma and Tau Beta Pi. He graduated with honors in addition to winning the Salisbury Prize.

After graduating WPI, he attended the University of Rochester where he spent his first year as a teaching assistant, for which he won the graduate teaching assistant of the year award. He then joined the high energy physics group working on E706 at the Fermi National Accelerator Laboratory. In addition to receiving his Master of Arts degree in Physics, he was awarded the Rush Rhees Fellowship his fourth year at Rochester.

Acknowledgements

First I wish to apologize to anyone who may feel slighted by my acknowledgements. All have meant a great deal to me and surely this thesis would not have been completed without all their guidance and support.

First on the list are my parents, Tom and Gilda Mansour. Without their support and self sacrifice I would never have been able to achieve the goals I have set for myself. I thank both of you for all you've ever done for me.

Next on my list comes the E706 collaboration. A project the size of E706 could not have been accomplished by one man nor, in many cases, by the same number of people as on our experiment. In particular, I would like to express great thanks to: Dane Skow, Chris Lirakis, Eric Prebys, and Bill DeSoi whose friendship has made living in Batavia a pleasant experience; Tara Chand, from St. Stephen's College in Delhi, India, whose help on the assembly of our calorimeter was greatly appreciated as was his friendship during the many months he stayed with us. As far as guidance in experimental particle physics, I would like to thank George Ginther, Fred Lobkowicz and Tom Ferbel for all their help over the years. I wish to thank Paul Slattery, for his dazzling show as spokesman for this experiment. His constant arbitration with Fermilab has made an impossible job merely difficult. I wish to thank Marek Zielinski for all his thoughtful guidance in the analysis of our data.

Special thanks should also be given to Bud Koecher, Jerry Sasek, Bob Maly, and Roger Hiller who helped us out of more tight spots than I can ever describe. I would also like to thank all the techs from Labs 6 and 8 who contributed to our experiment.

I wish to thank Betty Bauer, Sue Brightman, Betty Cook, Ovide Coriveau, Connie Jones, Judy Mack and Debbie Shannon-Mryglod of the University of Rochester for all the help and support they have provided while I was at Rochester and Fermilab. I would also like to thank Phyllis Hale and Joy Perington, from the Fermilab Users Office, for their support and friendship during my stay at Fermilab.

I would like to thank Jeff Owens from Florida State University who has provided us with an algorithm which was used to compare our data to QCD predictions. I would also like to thank Patrick Aurenche for taking time to answer my questions on QCD.

To use a cliché; last but not least, I wish to thank my wife, Sarah, for all her understanding when I work late at the lab, for all her understanding when I work at home, and most of all for being my friend.

This research has been supported in part by a grant from the Department of Energy.

Abstract

The π^0 inclusive cross section for π^- and p interactions on nuclear targets at 530 GeV/c has been measured as a function of transverse momentum (p_T) and rapidity, using the E706 spectrometer at FNAL. The photon detector used was a large liquid argon sampling calorimeter with an energy resolution of $\sim 15\%/\sqrt{E}$. The experiment employed a high p_T trigger formed by weighting the energy deposited in the calorimeter by the sine of the production angle as measured in the laboratory. The kinematic range studied is $4.0 \text{ GeV}/c < p_T < 10.0 \text{ GeV}/c$ and -0.7 to 0.7 in rapidity. Beryllium and copper targets were used to measure the atomic number (A) dependence of the cross section. The measurements are compared with other published results, as well as with leading order predictions from Quantum Chromodynamics (QCD).

Table of Contents

Curriculum Vitae	ii
Acknowledgements	iii
Abstract	v
Table of Contents	vi
Figure Captions	viii
Table Captions	xiv
1. Theoretical Motivation	1
1.1 Overview	1
1.2 QCD: An Introduction	2
1.3 Direct Photon Physics	3
1.4 π^0 Production and Background	7
1.5 Nuclear Dependence	9
2. Experimental Setup	10
2.1 Beamline/Target	10
2.2 Tracking System	12
2.3 Liquid Argon Calorimeters	15
2.4 Forward Calorimeter	29
3. Operation of the LAC	31
3.1 Shower Evolution and Charge Collection	31
3.2 Data Acquisition System	33
3.3 Trigger	34
3.4 Readout Electronics	36
4. Event Reconstruction	39
4.1 Overview	39
4.2 Tracking Reconstruction	40
4.3 Electromagnetic-Shower Reconstruction	44
4.4 Hadron Reconstruction	57
5. Data Analysis	59
5.1 Data Selection	59

5.2 Two- γ Mass Distributions	74
5.3 Acceptance and Reconstruction Efficiency	84
5.4 Trigger Corrections	86
5.5 Beam Particle Identification	89
5.6 Live Beam Count	89
5.7 Normalization of the Cross Section	91
6. Results and Conclusions	94
6.1 Cross Sections	94
6.2 Nuclear Dependence of Cross Sections	105
6.3 Ratio of Cross Sections for π^- and Proton Beams	111
6.4 Comparison to other Experiments	113
6.5 Comparison with Phenomenological Predictions	116
6.6 Conclusions	123
References	128

FIGURE CAPTIONS

- 1) Leading order diagrams for direct photon production.4
- 2) Layout of experimental apparatuses at the MWEST hall. Note the liquid nitrogen and liquid argon storage dewars located outside the building. Vacuum insulated transfer lines are used to supply the cryostat of either liquid as needed.11
- 3) Schematic of the E706 tracking system showing the SSDs surrounding the target region prior to the magnet. The PWCs are located downstream of the magnet.13
- 4) View of the Liquid Argon Cryostat being supported by the gantry. Located within the cryostat are located the electromagnetic and hadronic calorimeters, the filler vessel and beam pipe. Also shown are the rabbit crates, located on the top outer perimeter of the gantry.16
- 5) Geometry for the radial anode boards.17
- 6) Geometry for the azimuthal anode boards.17
- 7) Readout board for the azimuthal anode boards. The channels are connected, via braided wire, to all corresponding channels in the front or back sections. The tabs support connectors for the readout cables which are routed to the top of the gantry.19
- 8) Readout board for the radial anode boards. The channels are connected, via braided wire, to all corresponding channels in the front or back sections. The tabs support connectors for the readout cables which are routed to the top of the gantry.20
- 9) Exploded view of the EMLAC. Shown are the alternating layers of radial and azimuthal geometries as well as the slotted plates used to support springs which in turn support the lead plates.22
- 10) Compression spring support system used to apply a uniform supporting force to the slotted plates during contraction of the EMLAC.23

- 11) Pad geometry used in the hadronic calorimeter. Each triangle represents an isolated copper pad with small strips running from the bottom of the pad to readout boards on either side of the detector.25
- 12) Temperature of the front G-10 plate plotted as a function of time from the start of the cooldown process. The flat levels at 125 and 325 hours into cooldown indicate times at which cooldown was stopped in order to allow the temperature of the detector to equalize. 28
- 13) Temperature difference between the front G-10 plate and layer 33 plotted as a function of time from the start of the cooldown process.29
- 14) Spatial distribution of photons for events when the veto wall had a signal in the quadrant corresponding to the trigger quadrant of the EMLAC. 61
- 15) Spatial distribution of photons for events when the veto wall had no hit in the quadrant corresponding to the trigger quadrant of the EMLAC. ..62
- 16) Directionality expected for a muon from the halo of the beam and for a photon originating in the target.64
- 17) p_T dependence of directionality for events when the veto wall had a signal in the quadrant corresponding to the triggering quadrant of the EMLAC. At large p_T , the majority of photons have large directionalities, indicating that the background for large p_T photons are objects not originating from the target. 65
- 18) p_T dependence of directionality for events when the veto wall had no signal in the quadrant corresponding to the triggering quadrant of the EMLAC. The background at large p_T seen in Fig. 5.4 is removed by the requirement that the veto wall have no signal as mentioned above.66
- 19) p_T dependence for the time of arrival of photons for events when the veto wall had a signal in the quadrant corresponding to the triggering quadrant of the EMLAC. A large number of out of time events can be seen at ~ -45 ns for all p_T68

- 20) p_T dependence for the time of arrival of photons for events when the veto wall had no signal in the quadrant corresponding to the triggering quadrant of the EMLAC. The out of time events seen in Fig. 5.6 have been removed by this veto wall cut, indicating a correlation between out of time events and muons. 69
- 21) Directionality vs photon time of arrival for events when the veto wall had a signal in the quadrant corresponding to the triggering quadrant of the EMLAC. Out of time objects tend to have large directionalities, consistent with the assumption that they are muons from the beam halo. 70
- 22) Directionality vs photon time of arrival for events when the veto wall had no signal in the quadrant corresponding to the triggering quadrant of the EMLAC. In time objects are seen to originate from the target (small directionality). 71
- 23) Maximum uncorrelated energy per event. Events with zero uncorrelated energy are not plotted. 72
- 24) Distribution of vertices from high $p_T \pi^0$ events. The 20 beryllium targets and 2 copper targets are clearly visible. 74
- 25) Uncorrected number of events, having a high $p_T \pi^0$, per beryllium target. The dotted crosses represent the corrected number of events per target. Corrections being applied were for lost π^0 s due to photon conversions within the target and beam particle absorption within the target. 75
- 26) Two photon mass distribution near the π^0 mass for $p_T \geq 3.0 \text{ GeV}/c$. The dotted line represents the two photon mass distribution with an energy asymmetry cut of 0.75. 77
- 27) π^0 asymmetry distribution. The dotted line represents the asymmetry distribution for Monte Carlo generated π^0 s 78
- 28) Reconstructed π^0 mass per octant. 80
- 29) Corrected number of reconstructed π^0 s per octant. Corrections applied are for live beam and trigger efficiency. 81

- 30) Reconstructed π^0 mass as a function of radius. The drop at ~ 40 cm is due to reconstruction inefficiency at the inner/outer Φ boundary. The drop at ~ 90 cm is not yet understood. 82
- 31) Reconstructed π^0 mass as a function of azimuth angle, projected to quadrant one. The drop at $\sim \frac{\pi}{4}$ is due to energy loss into the neighboring octant. 84
- 32) Number distribution of reconstructed π^0 s as a function of azimuth angle, projected to quadrant one. The drop at $\sim \frac{\pi}{4}$ is due to trigger losses at octant boundaries. 85
- 33) Invariant differential cross sections as functions of p_T for different rapidity intervals. The cross sections are for π^- interactions on beryllium, divided by $A_{Be} = 9$ (per nucleon). The topmost data have the correct normalization, while the rest of the y intervals have progressive shifts by factors of 10. The curves represent integrations of Eq. (6.1) over the appropriate p_T and rapidity ranges. 100
- 34) Invariant differential cross sections for π^- interactions on beryllium, divided by $A_{Be} = 9$, as functions of rapidity averaged over several p_T ranges. The cross section for p_T between 5.0 and 8.0 GeV/c has been scaled by a factor of 10. The curves represent integrations of Eq. (6.1) over the appropriate p_T and rapidity ranges. 101
- 35) Invariant differential cross section as a function of p_T averaged over the full rapidity range. The cross section is for π^- interactions on beryllium, divided by $A_{Be} = 9.0$. The curve represents an integration of Eq. (6.1) over the appropriate p_T and rapidity ranges. 102
- 36) Invariant differential cross section as a function of p_T averaged over the full rapidity range. The cross section is for π^- interactions on copper, divided by $A_{Cu} = 63.5$. The curve represents an integration of Eq. (6.1) over the appropriate p_T and rapidity ranges. 103
- 37) Invariant differential cross sections as functions of p_T for different rapidity

- intervals. The cross sections are for p interactions on beryllium, divided by $A_{Be} = 9$ (per nucleon). The topmost data have the correct normalization, while the rest of the y intervals have progressive shifts by factors of 10. The curves represent integrations of Eq. (6.1) over the appropriate p_T and rapidity ranges. 104
- 38) Invariant differential cross sections for p interactions on beryllium, divided by $A_{Be} = 9$, as functions of rapidity averaged over several p_T ranges. The cross section for p_T between 5.0 and 8.0 GeV/c was scaled by a factor of 10. The curves represent integrations of Eq. (6.1) over the appropriate p_T and rapidity ranges. 106
- 39) Invariant differential cross section as a function of p_T averaged over the full rapidity range. The cross section is for p interactions on beryllium, divide by $A_{Be} = 9.0$. The curve represents an integration of Eq. (6.1) over the appropriate p_T and rapidity ranges. 107
- 40) Invariant differential cross section as a function of p_T averaged over the full rapidity range. The cross section is for p interactions on copper, divide by $A_{Cu} = 63.5$. The curve represents an integration of Eq. (6.1) over the appropriate p_T and rapidity ranges. 108
- 41) α , as a function of p_T , determined from the ratio of π^0 cross sections from π^- interactions on beryllium and copper. 109
- 42) α , as a function of p_T , determined from the ratio of π^0 cross sections from p interactions on beryllium and copper. 110
- 43) Ratio of the π^0 cross section measured from π^- interactions to that measured from p interactions. The cross sections are averaged over the full rapidity interval ($|y| < 0.7$). 112
- 44) π^0 cross sections as a function of p_T , for π^- interactions, from several experiments. The magnitude of the cross section is seen to increase with increasing center of mass energy. Cross sections from nuclear targets have been scaled using the value of α previously determined. 114

- 45) π^0 cross sections as a function of x_T , for π^- interactions, from several experiments. Cross sections from nuclear targets have been scaled using the value of α previously determined. The curve represents Eq. (6.3), with the parameters listed in the text.117
- 46) π^0 cross sections as a function of p_T , for p interactions, from several experiments. The magnitude of the cross section is seen to increase with increasing center of mass energy. Cross sections from nuclear targets have been scaled using the value of α previously determined.118
- 47) π^0 cross sections as a function of x_T , for p interactions, from several experiments. Cross sections from nuclear targets have been scaled using the value of α previously determined. The curve represents Eq. (6.3), with the parameters listed in the text.119
- 48) Comparison of π^0 data from π^- interactions on Be to that predicted from the integration of Eq. (1.7). Duke-Owens set 1 for nucleons and Owens Set 1 for pions were used with $\Lambda = 200$ MeV. Two choices of Q^2 are used to compare to data.121
- 49) Comparison of π^0 data from π^- interactions on Be to that predicted from the integration of Eq. (1.7). Duke-Owens set 1 for nucleons and Owens Set 1 for pions were used with $\Lambda = 200$ MeV. A modified version of the WA70 optimized Q^2 was used.122
- 50) Comparison of π^0 data from p interactions on Be to that predicted from the integration of Eq. (1.7). Duke-Owens set 1 for nucleons and Owens set 1 for pions were used with $\Lambda = 200$ MeV. Two choices of Q^2 are used to compare to data.124
- 51) Comparison of π^0 data from p interactions on Be to that predicted from the integration of Eq. (1.7). Duke-Owens set 1 for nucleons and Owens set 1 for pions were used with $\Lambda = 200$ MeV. A modified version of the WA70 optimized Q^2 was used.125

TABLE CAPTIONS

1: Shower shape parameters.	48
2: Breakdown of data sets used in this analysis.	59
3: Table of the events remaining after applying various cuts. Data sets B, E, and F are not shown because they were not available for this analysis.	60
4: Absolute π^0 acceptance as a function of p_T and rapidity.	87
5: Absolute π^0 reconstruction efficiency as a function of p_T and rapidity.	88
6: Corrections to normalization of cross sections.	92
7: Parameters for fits of relation (6.1) to experimental cross sections.	94
8: Invariant cross section in pbarn/GeV ² for $\pi^- + \text{Be} \rightarrow \pi^0 + \text{anything}$. Cells with no entries correspond to kinematic regions where either no π^0 s were detected or to regions where the background exceeded the detected number of π^0 s	95
9: Invariant cross section in pbarn/GeV ² for $p + \text{Be} \rightarrow \pi^0 + \text{anything}$. Cells with no entries correspond to kinematic regions where either no π^0 s were detected or to regions where the background exceeded the detected number of π^0 s	97
10: α dependence on rapidity for positive and negative beams.	111
11: Selected experiments to have published π^0 production cross sections.	115

1. Theoretical Motivation

1.1. OVERVIEW

The main goal of Fermilab experiment E706 is to measure direct photon cross sections for π^- , π^+ and proton beams interacting with several types of nuclear targets. In order to properly measure this cross section, all possible background to the direct photon signal must be understood. One of the main sources of background comes from the decay of π^0 s. A π^0 that is not properly reconstructed can produce two photons which may be misinterpreted as direct photons. It is the purpose of this thesis to measure the π^0 cross section to test aspects of QCD perturbation theory, as well as to assess the background that π^0 s present to the direct photon signal.

Particle production at large p_T is well described by the currently favored theory of strong interactions, namely Quantum Chromodynamics or QCD. Introductory reviews of QCD can be found in Pennington^[1](1983), R. Ellis^[2](1987), S. Ellis^[3](1987), and Reya^[4](1978). In the past ten years, much effort has gone into the theoretical calculation and experimental measurement of direct photons, and I shall present, in the next section, some of the motivation for studying processes such as direct photon production. A theoretical review of direct photon physics can be found in Owens^[5] (1987). Experimental reviews can be found in Ferbel and Molzon^[6] (1984), Ferbel^[7](1988) and Camilleri^[8] (1988). As we will see, compared to direct photons, production of high p_T single hadrons and jets present additional challenges for the calculation of cross sections; this is because of the complication of having another parton in the final state. Jets are produced when partons fragment into various hadrons; experimental results are

therefore sensitive to algorithms that are used to define such jets. Single-particle production is simple from an experimental viewpoint, but involves the fragmentation of a constituent into some specific particle; this is difficult to calculate, but experimental results can be used to determine fragmentation functions of partons.

1.2. QCD: AN INTRODUCTION

The parton model has been used to account for the pointlike particles which electron scattering experiments at SLAC have revealed to be present in hadrons. Quarks, proposed by Gell-Mann^[9] (1964), are fermions with spin $1/2$, that seem to have the same properties as the partons. Consideration of the quark content of hadrons leads us to introduce a new quantum number, color, in order to be consistent with the Pauli exclusion principle.* Since colored particles have never been observed free, partons must undergo a transformation into color neutral objects (hadrons) before they can be detected.

To understand interactions of colored partons, a Yang-Mills gauge theory (QCD) with an internal color $SU(3)$ symmetry group, was introduced. In QCD, partons refer to either the quarks proposed by Gell-Mann or to spin 1, electrically neutral, gluons. Gluons in QCD play a role analogous to photons in QED, in that they are the mediators of the strong force. QCD is unlike QED in that gluons have color charge, while photons do not carry electric charge. Mathematically, this property is a result of the commutation relations of the generators of the

* For example, the quark content of the Δ^{++} resonance is (uuu) , which, without color, is a symmetric state of three fermions in violation of the Pauli exclusion principle.

SU(3) symmetry group. Gauge theories having this property are known as non-Abelian. An important feature of QCD is asymptotic freedom. Asymptotic freedom, defined below, allows us to use perturbative techniques for calculating cross sections at high energies.

In QCD, the coupling constant for strong interactions is, to leading-log in Q^2 (Ref. 5),

$$\alpha_s(Q^2) = \frac{4\pi}{(11 - \frac{2}{3}n_f)\log(\frac{Q^2}{\Lambda^2})} \quad (1.1)$$

where Q^2 is a measure of the momentum transfer in the collision, Λ is a scale parameter required by the theory, and n_f is the number of quark flavors available at the energy of the collision. Equation (1.1) shows that as Q^2 increases $\alpha_s(Q^2)$ decreases: this is referred to as asymptotic freedom. In fact, at $Q^2 \geq 10\text{GeV}^2$, α_s decreases to the point where the coupling is weak enough so that perturbative techniques for cross section calculations[†] can be used. Because high p_T interactions can be treated perturbatively, it is important to study such interactions to obtain a quantitative comparison with experiment.

1.3. DIRECT PHOTON PHYSICS

Direct photons are photons produced in parton interactions, and not photons that originate from the decay of particles such as π^0 s and η s. Such parton collisions, involving one electromagnetic vertex, are simpler in the sense that the photon is produced free of other particles, thus the photon carries away all the p_T of the interaction. In the scattering of two partons to two partons

[†] Perturbative calculations are necessary because non-perturbative calculations are not available at present.

at some p_T , the final state partons fragment into hadrons of lower p_T . As mentioned previously, studying such interactions is relatively difficult since all fragments of the original parton must be detected and then associated with the correct parton. Direct photons consequently provide a far cleaner probe of parton-parton interactions.

The leading order graphs for direct photon production are shown in Fig. 1.1. The graphs are of the annihilation and Compton scattering processes and correspond to order α_s terms.

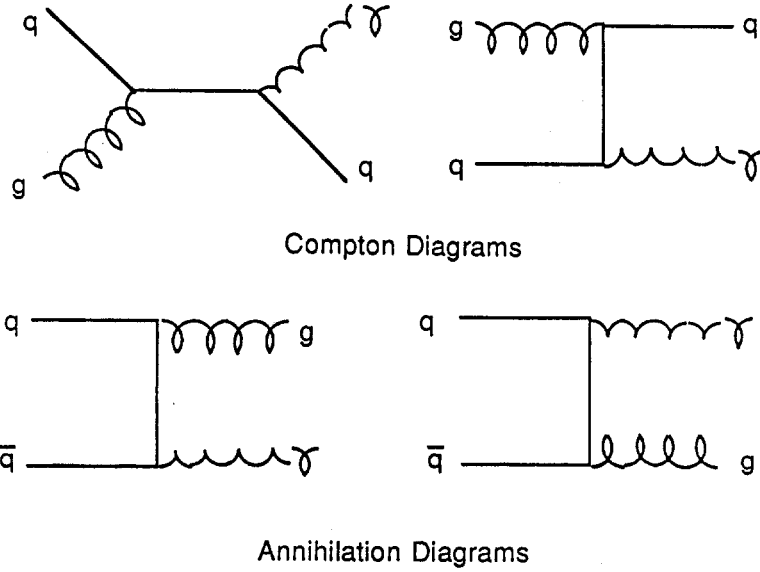


Figure 1.1 Leading order diagrams for direct photon production.

The invariant inclusive cross section for direct photon production, $A + B \rightarrow \gamma + X$, can be written in terms of leading order in α_s as follows:

$$E \frac{d\sigma}{d^3p} = \sum_{ab} \int dx_a dx_b G_{a/A}(x_a, Q^2) G_{b/B}(x_b, Q^2) \times \frac{\hat{s}}{\pi} \frac{d\sigma}{d\hat{t}}(ab \rightarrow \gamma d) \delta(\hat{s} + \hat{t} + \hat{u}) \quad (1.2)$$

where \hat{s} , \hat{t} and \hat{u} are the Mandelstam variables for the point-like scattering, given by $\hat{s} = (p_a + p_b)^2$, $\hat{t} = (p_a - p_\gamma)^2$, and $\hat{u} = (p_a - p_d)^2$; p representing the four momenta of the parton or photon, and a , b , and d identifying the two colliding and one emitted quark. $G_{i/I}$ is the number distribution for parton i in hadron I with a momentum fraction between x and $x + dx$. The function G is related to the structure function by factor of $\frac{1}{x}$ ($F = xG$, where F is the structure function). Since calculation of these functions requires knowledge of the wave functions within the hadrons, a region where perturbation theory is not applicable, at present, they must be determined experimentally. For the processes shown in Fig. 1.1, the elementary cross sections are (Ref. 6)

$$\frac{d\sigma}{d\hat{t}}(qg \rightarrow q\gamma) = -\frac{\pi\alpha\alpha_s}{2\hat{s}^2}e_q^2\frac{\hat{u}^2 + \hat{s}^2}{\hat{s}\hat{u}} \quad (1.3)$$

$$\frac{d\sigma}{d\hat{t}}(\bar{q}q \rightarrow g\gamma) = \frac{8\pi\alpha\alpha_s}{9\hat{s}^2}e_q^2\frac{\hat{u}^2 + \hat{t}^2}{\hat{t}\hat{u}}. \quad (1.4)$$

The Q^2 dependence in the distribution function is attributed to collinear gluon emission (higher order α_s processes), in which mass singularities are absorbed into the distribution function through the application of the factorization theorem (Ref. 5). This is known as scaling violation, that is, the distribution functions no longer scale with x (as predicted in the parton model), but evolve with Q^2 , as given by the Altarelli-Parisi equations.^[10] One should note that Eq. (1.2) looks like the Born term for the lowest order processes convoluted with Q^2 dependent distribution functions.^[11]

Through the Compton-scattering graph, direct photon interactions involve gluon structure in leading order. Because of this fact, direct photon cross sections are ideal for obtaining information on gluon structure functions of hadrons.

Deep-inelastic lepton-nucleon experiments do not constrain the gluon content of hadrons as well as direct photon experiments do, because gluons enter that cross section only through higher order terms in α_s . The Compton graph contributes equally to π^+ and π^- interactions, but the annihilation term can be isolated by subtracting the direct photon cross section for π^+ beam from the cross section obtained from π^- beam. After the annihilation graph has been isolated the compton contribution can be extracted in order to measure the gluon structure function.

Higher Order Calculations

One of the main concerns of the leading order cross section is the definition used for the momentum scale, Q^2 . QCD does not restrict Q^2 to any particular form, but just suggests it should be of the order of p_T^2 . In fact, a different momentum scale can be chosen for distribution functions, fragmentation functions, and α_s . The distinction between scales arises only when one considers higher order terms in α_s .

Calculations of direct photon cross sections to order α_s^2 were first performed by the group of P. Aurenche, et. al.^[12] These calculations indicated that the cross section calculated to next order becomes less sensitive to the choice of momentum scales. This happens because the behavior of the higher-order correction is opposite to that of the leading term; that is, the leading-log part decreases with increasing Q^2 , whereas the effect of the higher order part is to increase with increasing Q^2 , thereby diminishing the dependence on the choice of Q^2 relative to that in the leading-log approximation.

Aurenche et. al. then applied an optimization procedure to their calcula-

tions, known as the principle of minimum sensitivity (PMS),^{[13][14][15]} in the hope of choosing the momentum scales for the distribution functions and α_s so as to minimize the variation of the cross section with small changes in scales. This procedure has met with some criticism, because the momentum scales often take on forms that have an unappealing dependence on p_T^2 . In fact, one experiment published the following optimized scales:

$$Q_{s.f.}^2 = 0.35(1 - 2p_T/\sqrt{s})p_T^2 \quad (1.5)$$

$$Q_{\alpha_s}^2 = (0.55678p_T - 1.6254)^2 + 0.16807, \quad (1.6)$$

where $Q_{\alpha_s}^2$ and $Q_{s.f.}^2$ refer to scales for α_s and for the structure function, respectively. Although the PMS procedure is controversial, it has been applied with great success to direct-photon processes.

1.4. π^0 PRODUCTION AND BACKGROUND

Direct photon background

π^0 decays represent a major component of the background to the direct photon signal. In order to account for this background, the π^0 cross section must be measured precisely. It has been shown in many experiments that, for large p_T , production of direct photons can be comparable to that of π^0 s. Consequently, at the highest p_T , any uncertainty in the π^0 cross section, or background from π^0 s to the direct-photon yield, are not very important. At lower p_T ($< 4.0 \text{ GeV}/c$), however, the π^0 subtraction is delicate and must be done with great care.

π^0 production

Production of π^0 s involves additional convolutions not present in Eq. (1.2), known as fragmentation functions. Fragmentation functions contain information about how partons share momenta when they fragment into hadrons. Such functions are not predicted by QCD, and have to be determined experimentally. Predicted π^0 cross sections are consequently sensitive to the form of fragmentation functions, and therefore provide a means of measuring such functions. The cross section for inclusive hadron production, expressed to leading-log, is given by (Ref. 5)

$$E \frac{d\sigma}{d^3p} = \sum_{abcd} \int dx_a dx_b dz_c G_{a/A}(x_a, Q^2) G_{b/B}(x_b, Q^2) D_{C/c}(z_c, Q^2) \times \frac{\hat{s}}{z_c^2 \pi} \frac{d\sigma}{d\hat{t}}(ab \rightarrow cd) \delta(\hat{s} + \hat{t} + \hat{u}) \quad (1.7)$$

where $D_{C/c}$ is the fragmentation function, giving the probability density of finding hadron C with a momentum fraction between z and $z + dz$ from the fragmentation of parton c . In Eq. (1.7) the parton-level cross sections involve two strong vertices, and are therefore of order α_s^2 . The next-to-leading-log cross section, would then be of order α_s^3 . Such a calculation has recently been made by F. Aversa et. al.^[16] Predictions based on this calculation are not available at this time, but are expected shortly. Calculations using the leading-log approximation for π^0 production have been provided to us by Jeff Owens and will be presented in Chapter 6.

1.5. NUCLEAR DEPENDENCE

The cross sections to be presented in this thesis were measured on nuclear targets, and divided by the atomic weight of the target to obtain the yield per nucleon. In principle, the dependence on atomic weight is unknown. In fact, the Chicago-Princeton^[17] group reported $\sim A^{\frac{2}{3}}$ dependence for pion production at low p_T , and $\sim A^{1.1}$ at p_T of about 3 GeV/c. This would seem to indicate the presence of some form of coherent behavior among nucleons within the nucleus. In Chapter 6 we will present the A dependence on cross sections for beryllium and copper targets. Comparison of our data with results from experiments involving nucleon targets will necessitate a correction if there is a departure from a simple A^1 dependence.

In the remaining sections of this thesis we will discuss the apparatus used in experiment E706, the analysis procedures, the character of π^0 production, and the interpretation of the results in terms of phenomenology.

2. Experimental Setup

This experiment was performed in the Fermilab experimental hall MWEST. The layout of the detectors within the experimental hall is shown in Fig. 2.1. In the following sections I will describe the charged particle tracking system, the liquid argon calorimeters and the forward calorimeter. Not shown in Fig. 2.1 is the Cherenkov counter which is located in the beamline upstream of the hall.

2.1 BEAMLINE/TARGET

Beamline

The beamline for experiment E706 is known as MW9. The source for this secondary beam is the 800 GeV/c primary proton beam. The secondary beam is generated using a 0.75 interaction-length aluminum target, producing either positive or negative beam polarities. When running with positive polarity, the beam consists of $\sim 90\%$ protons, $\sim 7\%$ π^+ and $\sim 2\%$ K^+ , while the negative beam is composed of $\sim 97\%$ π^- , $\sim 3\%$ K^- and $< 1\%$ antiprotons. Our experiment took data with a secondary beam energy of 530 GeV/c and an intensity of 50×10^6 particles in a 20 second spill time.

Major components of the beamline are 3 large "spoiler" magnets for muon deflection, a Cherenkov counter for particle identification, a vertical sweeping magnet for electron calibration of the calorimeters, a large hadron shield to eliminate beam halo, and two veto walls for rejecting muons. The hadron shield consists of large sheets of steel, approximately 6 inches thick, layered at an angle to the beam axis to prevent halo particles from passing through gaps between the steel.

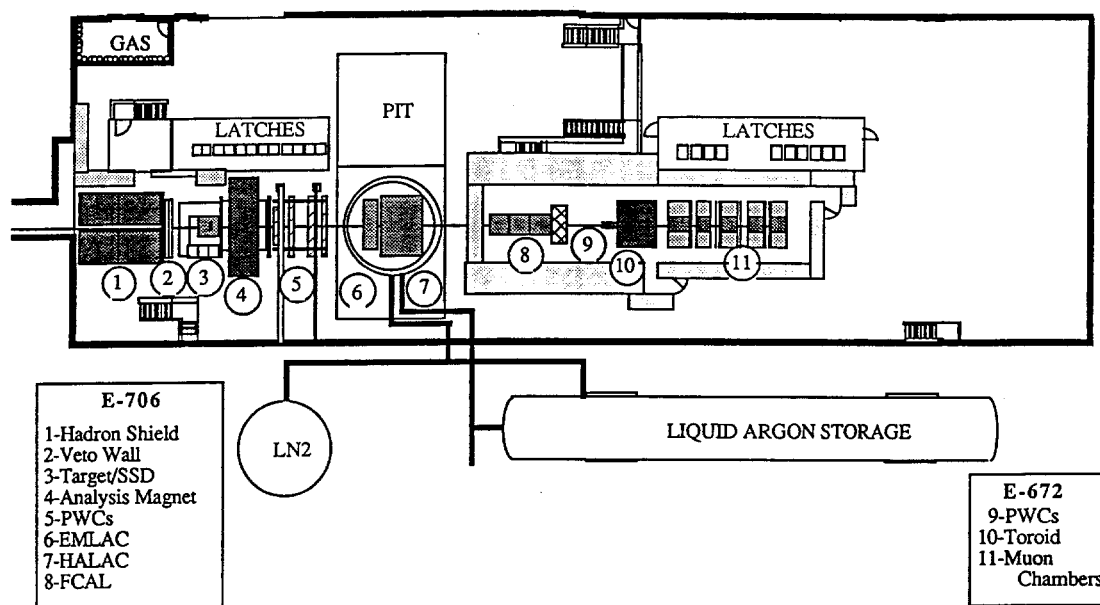


Figure 2.1 Layout of experimental apparatuses at the MWEST hall. Note the liquid nitrogen and liquid argon storage dewars located outside the building. Vacuum insulated transfer lines are used to supply the cryostat of either liquid as needed.

The Cherenkov detector is 42 m long and has a radius of 24.4 cm. Helium gas, at a pressure between 4 and 7 psia, is used as the radiator. Photons are detected by two rings of six phototubes each. The outer ring is termed anticoincidence or veto channel, while the inner ring is the coincidence channel. Scintillation counters placed at the two ends of the detector are used in coincidence to define a good beam particle. The Cherenkov detector is capable of tagging K^- with

an efficiency of $\sim 42\%$, and contained a remnant 3% π^- contamination. In the positive beam, π^+ were tagged with $\sim 78\%$ efficiency and contained a remnant 8% contamination from K^+ .^[18]

The two muon veto walls, put in coincidence with each other, were used to reject any trigger that had a hit in both walls. Each of the walls were 3 m by 3 m, and the two were offset with respect to each other so as to minimize the effects of gaps in one of the walls.

Target

The main targets used were copper and beryllium. The target area consisted of two Cu targets 0.08 cm thick and spaced 0.16 cm apart. Following the Cu were 20 Be targets 0.2 cm thick and spaced 0.16 cm apart. The first Be target was positioned 0.32 cm from the Cu. The target assembly was placed after 3 Silicon Strip Detectors (SSD), in front of the rest of the SSD system. This allowed for the calculation of the slope of the beam trajectory, and provided good vertex definition.

Several other targets were used during the run, but the results will not be given in this thesis. Data without a target in position were also taken to study the nature of background tracks in the SSD system.

2.2 TRACKING SYSTEM

In order to measure charged particles produced in association with high momentum direct photons and π^0 's, the experiment utilizes a magnetic spectrometer consisting of a Silicon Strip Detector (SSD), an analysis magnet, and a set of proportional wire detectors (PWC's). As mentioned previously, several

SSD planes are located before the target for beam identification, while the rest are located behind the target. Downstream of the SSD system is the analysis magnet, which imparts a transverse momentum kick of 450 MeV/c to the charged particles. Immediately behind this magnet are located the PWC's. A schematic of the tracking system is shown in Fig. 2.2. The following sections will briefly describe the SSD and PWC systems.

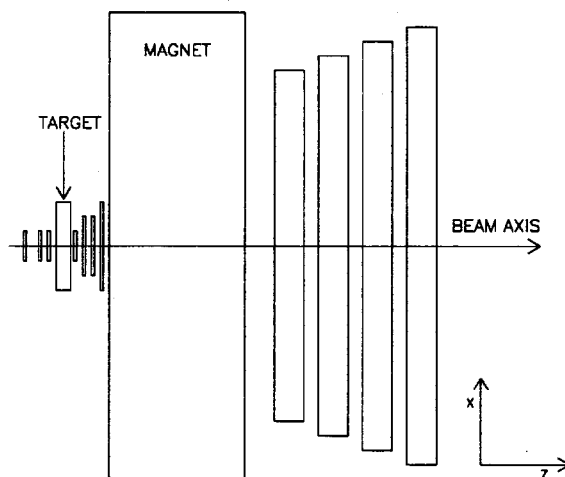


Figure 2.2 Schematic of the E706 tracking system showing the SSDs surrounding the target region prior to the magnet. The PWCs are located downstream of the magnet.

SSD

The SSD system is constructed of seven X - Y modules, with two planes per module and a total of 7,120 instrumented strips. The three modules in front of the target and the first one following the target have $3 \times 3\text{cm}^2$ wafers, while the

remaining modules have $5 \times 5 \text{ cm}^2$ wafers. All the SSD's are $250 - 300 \mu\text{m}$ thick with a pitch of $50 \mu\text{m}$.

Each plane of the system is essentially a PIN diode. Reverse biasing the diode sets up an electric field across the junction. When a minimum ionizing particle (MIP) enters the diode, electron - hole pairs are generated. These pairs are separated by the electric field, thereby causing a small current. Such MIPs will produce about 24,000 electron-hole pairs in any plane of the detector. The collection time for the signal, which depends on the electric field strength and the mobility of the carriers, is approximately 20 ns. The signal is sent to a charge-sensitive preamplifier whose output is amplified again and then discriminated. The final result is converted to a logic signal and read out.

PWC

The PWC system consists of four modules with four planes per module. The combined PWC and SSD system is designed to run at a 1 Mhz interaction rate. Each of the four modules has one X, Y, U and V view. The wires in the U-view are tilted at 37° and the V-view at -53° relative to the vertical. The sense wires are gold-plated tungsten and have a pitch of 0.254 cm. The four modules have active areas $1.22 \text{ m} \times 1.22 \text{ m}$, $2.03 \text{ m} \times 2.03 \text{ m}$, $2.03 \text{ m} \times 2.03 \text{ m}$, and $2.44 \text{ m} \times 2.44 \text{ m}$. The cathodes are made of mylar coated with graphite, so that the high voltage can be independently set over different segments of the wire. This allows the deadening of the center of the chambers during high intensity running. Except for the preamplifier, the readout system is the same as that for the SSD's.

2.3 LIQUID ARGON CALORIMETERS

The main element of the experiment is a large (~ 3 m diameter) liquid-argon calorimeter (LAC), consisting of hadronic and electromagnetic components. Together, the calorimeters reside in a large stainless-steel cryostat, supported by a gantry, which can be moved in a direction transverse to the beam axis. Within the cryostat, the electromagnetic calorimeter is located in front of the hadronic section; a helium-filled beam pipe (~ 40 cm in diameter) runs through the center of both. In front of the electromagnetic section is a foam-filled filler vessel. The components of the cryostat are shown in Fig. 2.3. The purpose of both the filler vessel and beam pipe is to displace the argon with a lower density material in order, to reduce unwanted interactions that could complicate event reconstruction.

The Electromagnetic Calorimeter

The electromagnetic section of the LAC consists of four independent sections. Each of the quadrants is constructed of 66, 0.8573 cm thick, layers; each consists of a 0.2 cm lead sheet, followed by 0.25 cm of liquid argon, followed by a G-10 copper-cladded anode board, followed by another 0.25 cm argon gap. The lead is made of 98.6% lead, 0.07% calcium and 1.3% tin. The Ca and Sn are added to increase the stiffness of the lead, so as to prevent buckling of the large (quadrant sized) plates under their own weight.

The G-10 anode boards are of octant size, and each octant is read out independently of the other. The anode boards have radial and azimuthal geometry as shown in Figs. 2.4 and 2.5. The boards alternate with each layer; the stack starts with a radial board.

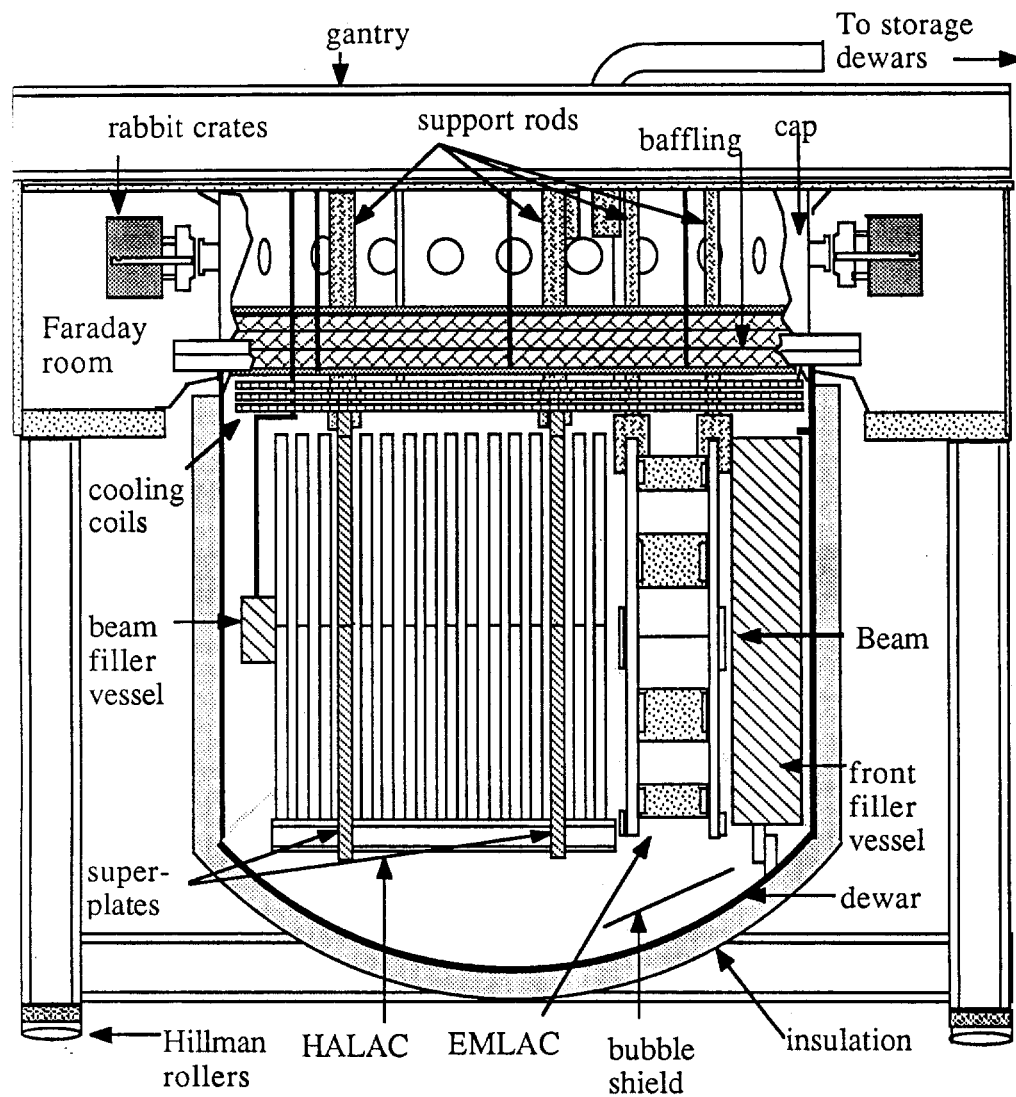


Figure 2.3 View of the Liquid Argon Cryostat being supported by the gantry. Located within the cryostat are located the electromagnetic and hadronic calorimeters, the filler vessel and beam pipe. Also shown are the rabbit crates, located on the top outer perimeter of the gantry.

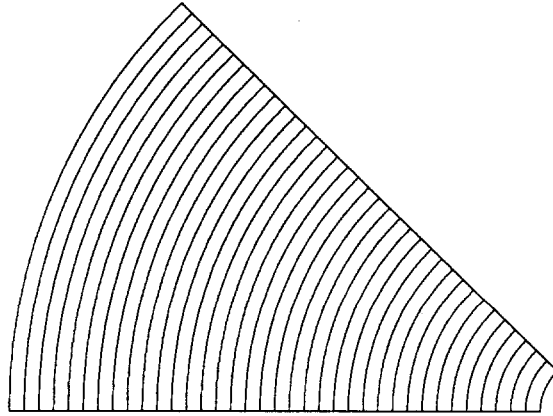


Figure 2.4 Geometry for the radial anode boards.

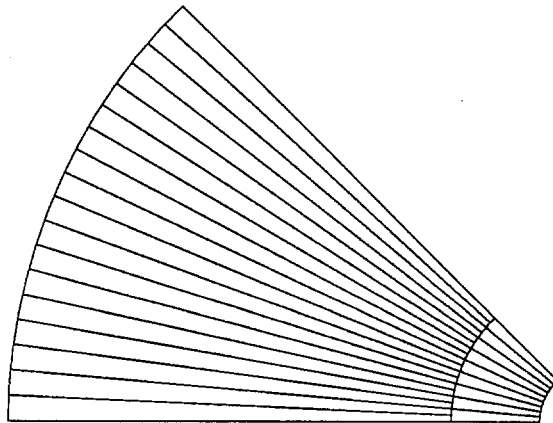


Figure 2.5 Geometry for the azimuthal anode boards.

The radial boards consist of 256 strips, cut in such a manner that they are focused on the target, which is 900 cm upstream of the LAC. The width of the strips on the first radial layer are 0.5466 cm. Each successive radial board has

a strip width given by

$$w = \frac{0.5466}{900.0} [900.0 + 1.56 \times (i - 1)] \quad (2.1)$$

where i is the i^{th} radial board and 1.56 is the distance between two consecutive boards of the same type. The radius to the center of the strips is given by

$$r = \frac{900.0 + 1.56 \times (i - 1)}{900.0} [21.59 + s \times 0.5466] \quad (2.2)$$

where s is the s^{th} strip on the board, and i is as given in Eq. (2.1).

The azimuthal boards are split into inner regions, containing 96 copper strips, each subtending 0.016 radians in azimuth, and outer regions containing 192 strips. The inner/outer split, occurring at a radius of 40.2 cm, helps improve spatial resolution at larger radii by reducing strip widths by a factor of two. The inner and outer regions are read out independently.

Longitudinally, the calorimeter is read out in two sections. The front section consists of 22 layers (about 10 radiation lengths), while the back contains the remaining 44 layers. The read out is achieved by connecting similar strips on each anode board by attaching U-shaped clips to each board, and soldering them together with braided wire. The clips at the end of any chain are attached to one of six different G-10 readout boards (three in front and three in back). Examples of azimuthal and outer radial readout boards are shown in Figs. 2.6 and 2.7.

Each readout board has between 6 and 8 cables connected to it; these are routed through the insulation at the top of the cryostat, through one of twenty feed-throughs that encircle the top outer region of the cryostat (see Fig. 2.3), and into amplifier crates.

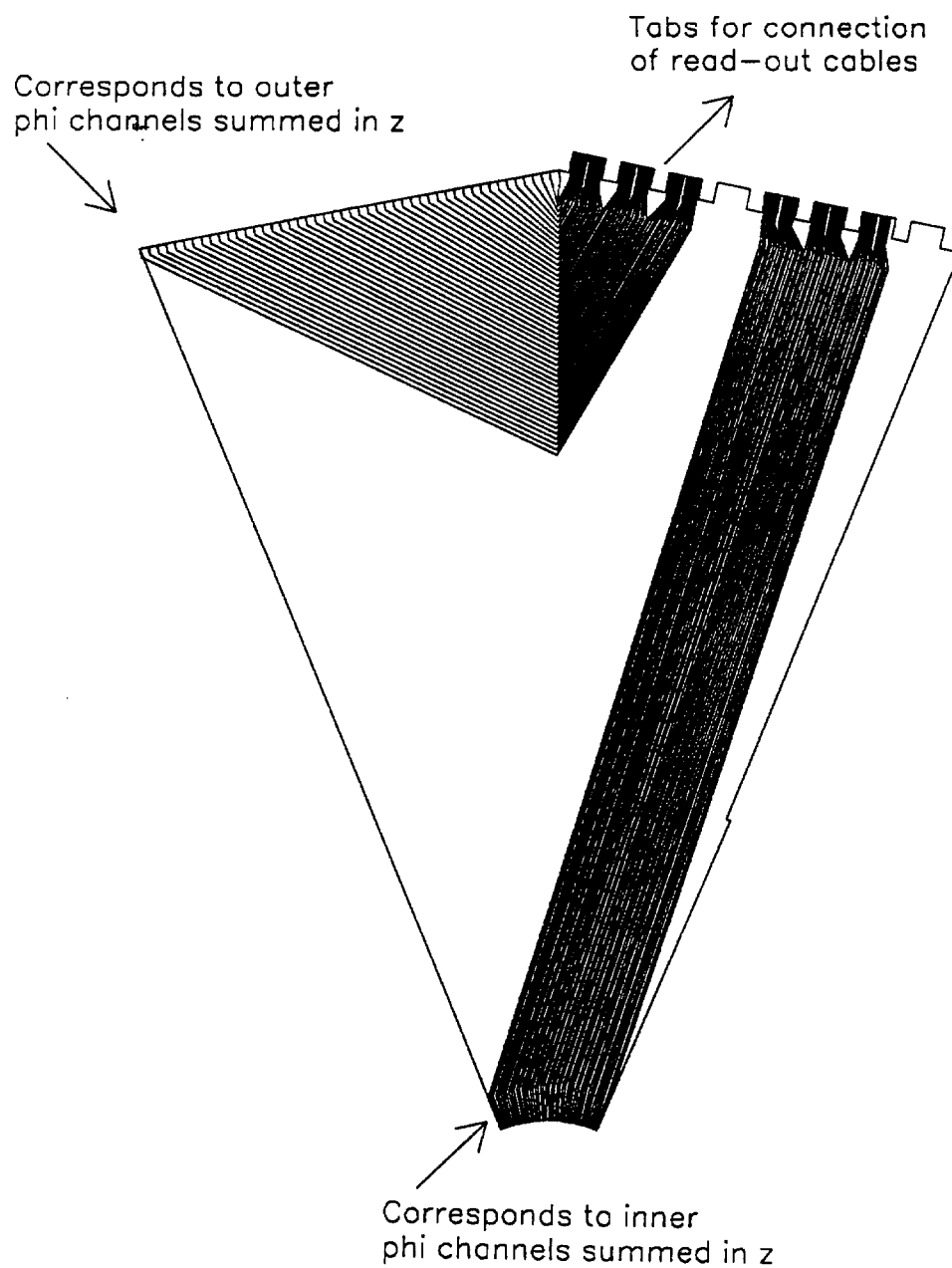


Figure 2.6 Readout board for the azimuthal anode boards. The channels are connected, via braided wire, to all corresponding channels in the front or back sections. The tabs support connectors for the readout cables which are routed to the top of the gantry.

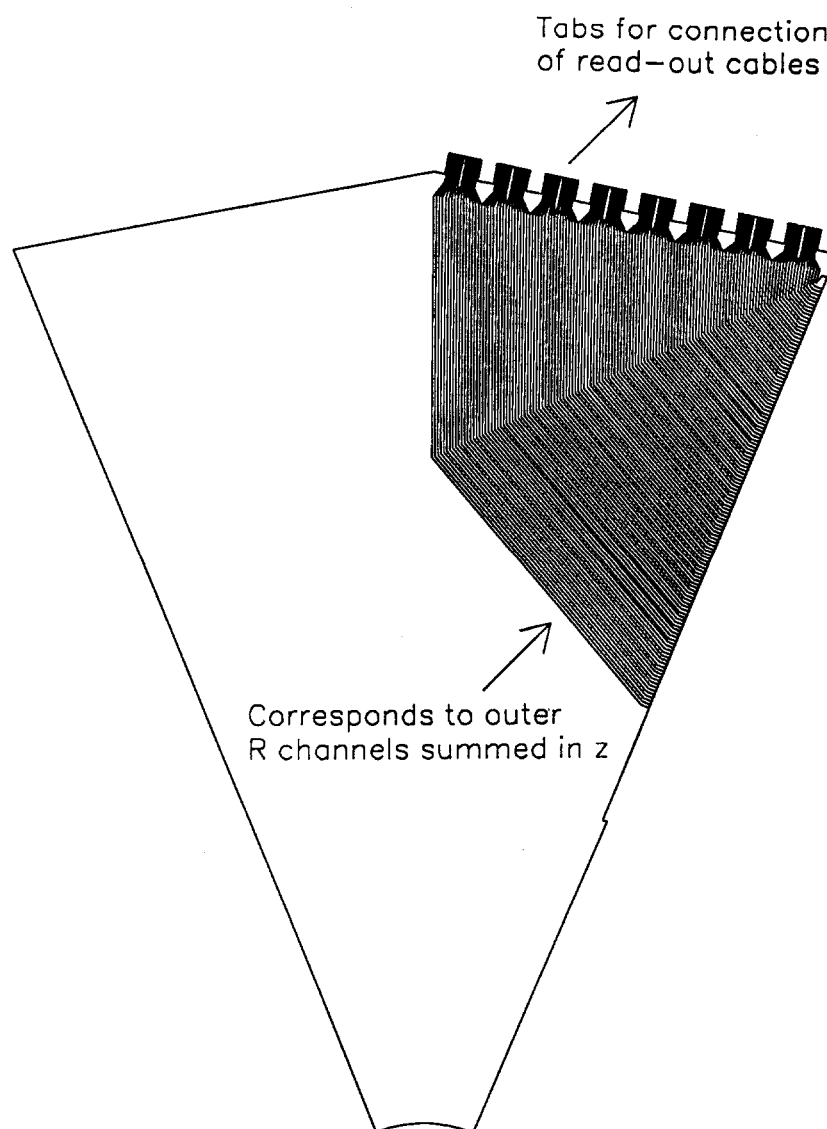


Figure 2.7 Readout board for the radial anode boards. The channels are connected, via braided wire, to all corresponding channels in the front or back sections. The tabs support connectors for the readout cables which are routed to the top of the gantry.

Because the lead plates are connected to high voltage, they must be kept from contact with the anode boards. This is accomplished by epoxying small G-10 buttons at random locations on the anode boards. At octant boundaries, we use G-10 "yo-yo's" that overlap each octant anode board. This prevents the anode boards from developing bulges and shorting to the lead. At the edges, the lead rests in teflon runners that keep it from contact with ground.

Each quadrant is supported by two full-sized G-10 plates located in the front and back of the calorimeter, which are connected by two rectangularly shaped slotted stainless steel plates bolted to the outer edges of the G-10, as shown in Fig. 2.8. The G-10 plates are 3.56 cm thick. The slots in the steel plates were made to support tubes of springs which push against the lead sheets, pressing them towards the inner radius. Adjoining quadrants are connected at their common boundary by one of four wedge-shaped steel plates. Each quadrant is bolted to half of the steel plate. The rectangular steel plates are attached to the main support rings by high compression spring washers, shown in Fig. 2.9. The spring washers were used to maintain a fixed amount of force when the detector contracts at low temperature. Four suspension rods from the gantry are used to support the calorimeter within the cryostat.

The Hadronic Calorimeter

The hadron calorimeter (HLAC) consists of 52 layers. Each layer contains a 2.54 cm steel plate, a 0.32 cm argon gap and a readout module.^[19] An extra module is placed in front of the first steel plate to provide a total of fifty three readout modules. Since the interaction length of hadrons is greater than the radiation length for photons, far more material is needed for shower containment

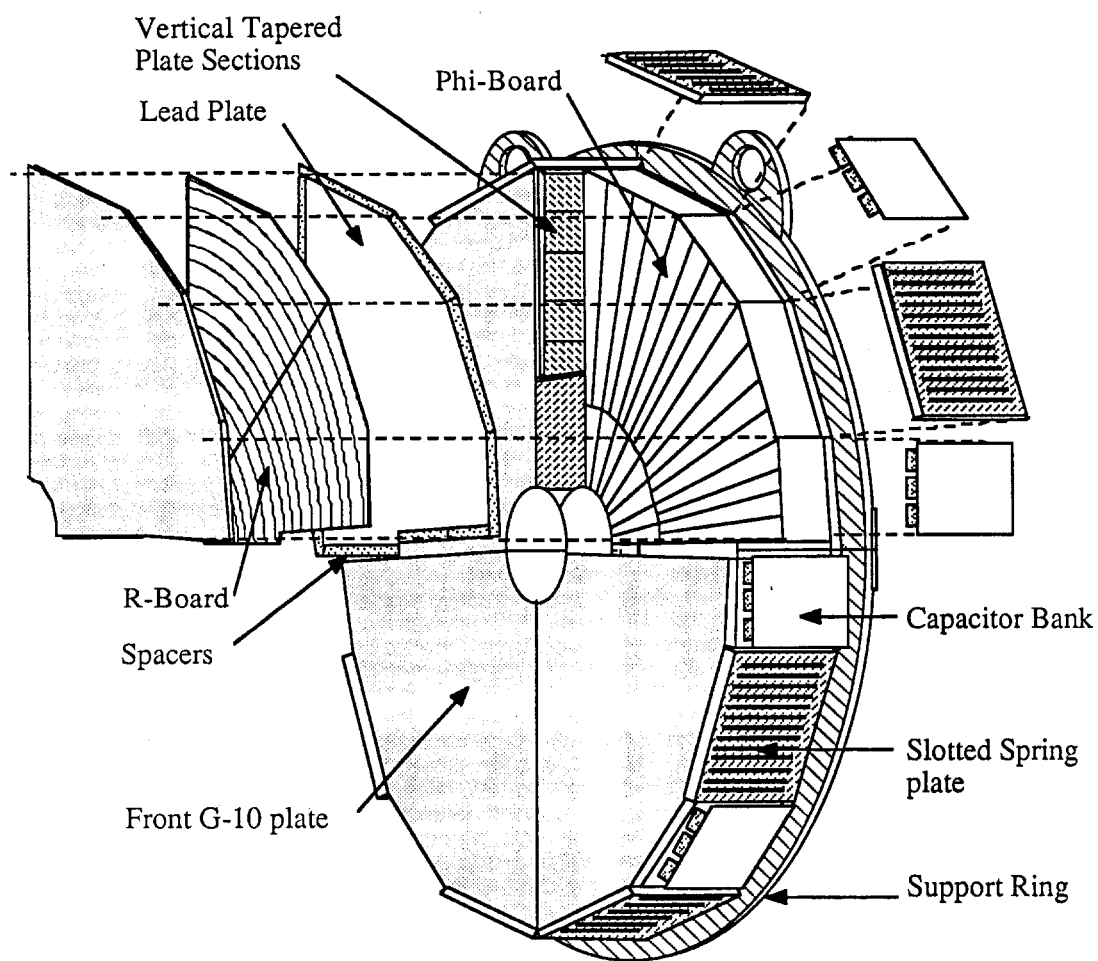


Figure 2.8 Exploded view of the EMLAC. Shown are the alternating layers of radial and azimuthal geometries as well as the slotted plates used to support springs which in turn support the lead plates.

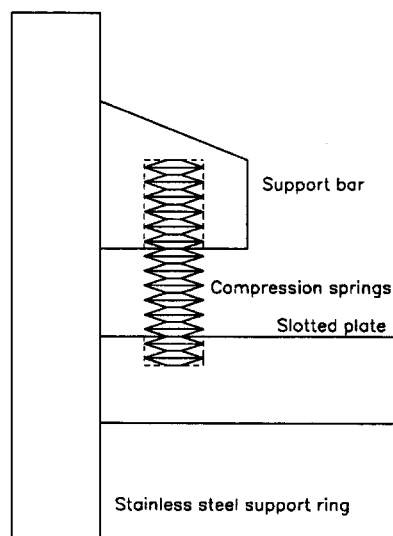


Figure 2.9 Compression spring support system used to apply a uniform supporting force to the slotted plates during contraction of the EMLAC.

in the HLAC. The total number of proton interaction lengths is 9.78, with 2.03 provided by material up to the end of the EMLAC, and the remainder by the HLAC.

Two of the 52 steel plates are called super plates because they support the HLAC. Four support rods from the gantry are attached to the two super plates by means of large clevises. At the bottom of the super plates, and running between them on either side, are two I-beams. These I-beams form the support for the remaining 50 plates. The super plates and I-beams are made of stainless 316L because of its excellent cryogenic properties. The remaining steel is stainless 410 which is not as structurally sound but need only support its own weight.

A complete description of the readout module structure and fabrication can be found in the PhD. Dissertation by C. Lirakis of Northeastern University

(Ref. 19). I shall present here a brief description of the module, concentrating primarily on the readout geometry. Each module is built from 7 layers that are glued together. The outer layers are double copper clad G10, with the interior side held at high voltage and the outer layer at ground. Behind the high voltage board is the G10 readout board, separated from the high voltage plane by G10 ribs. The side of the readout board facing the high voltage plane is etched with triangular readout pads, as shown in Fig. 2.10. The two readout boards are separated by G10 ribs running perpendicular to the other ribs. This provides structural support for the module.

The pad sizes of the hadron readout boards were chosen to match the typical transverse spread of hadron showers. The pads are arranged in a tower structure, such that the triangle size is proportional to the longitudinal position of the module. The size of the pad is given by

$$h = \frac{0.2}{9.0}z \quad (2.3)$$

where z is given by

$$z = 968.0 + 4.92 \cdot j \quad (2.4)$$

and j is the module number.^[20] The modules come in one of four patterns. The four patterns have 1206 pads, 1134 pads, 1008 pads and 874 pads respectively. The HLAC is read out in two sections, with section one containing all pattern one type boards and section two having a mix of the remaining patterns.

The Cryogenic System and the Cooldown Process

A cryogenic system that meets the following general specifications is required to operate the LAC:

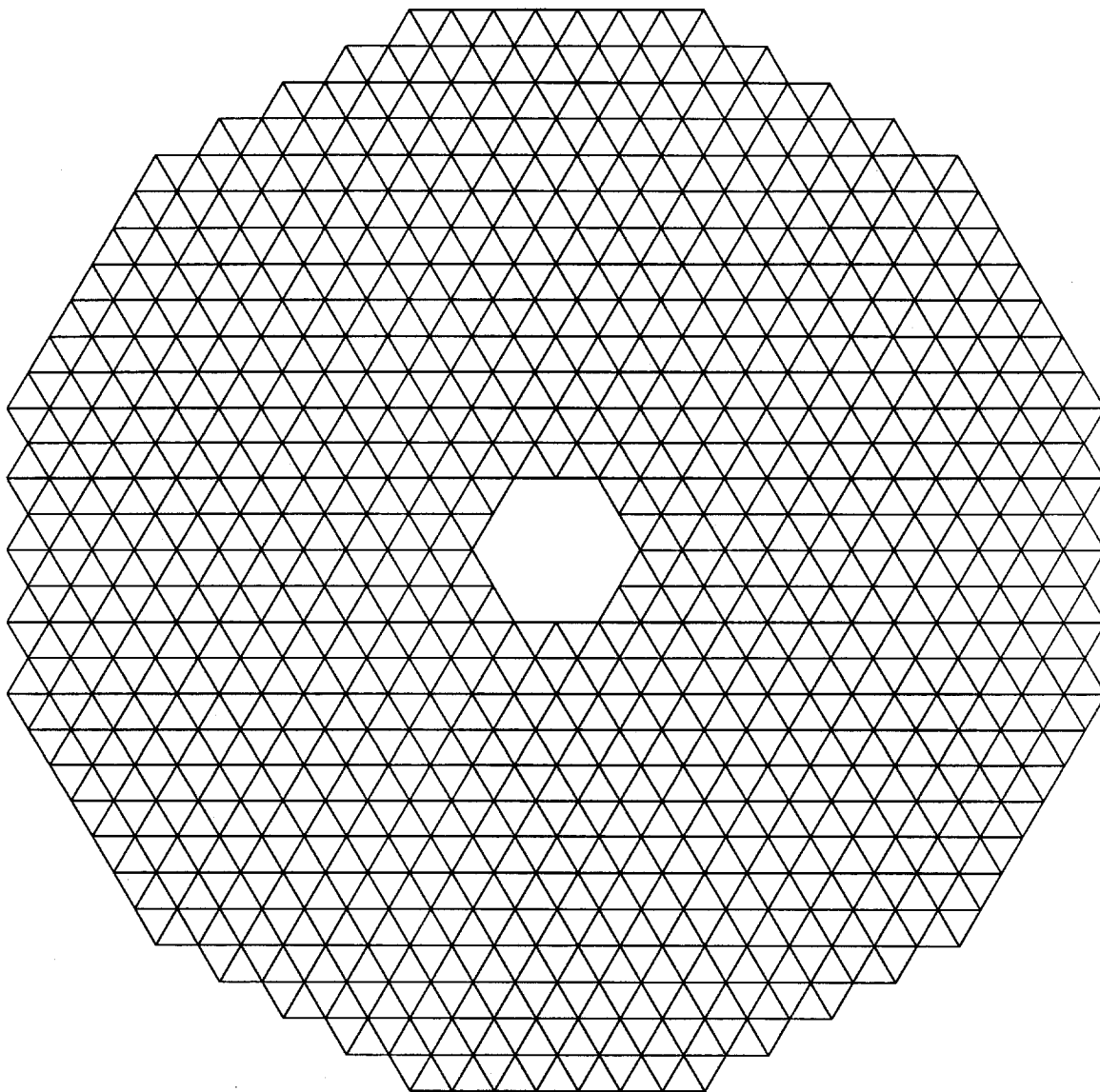


Figure 2.10 Pad geometry used in the hadronic calorimeter. Each triangle represents an isolated copper pad with small strips running from the bottom of the pad to readout boards on either side of the detector.

- It must cool the LAC to liquid argon temperatures
- It must deliver liquid argon to the cryostat

- It must maintain a safe temperature and pressure within the cryostat during running conditions.

These functions were difficult to implement due to the fact that the argon had to remain pure to within ~ 1 ppm O_2 equivalent during five months of data taking.

The main sections of the cryogenic system consist of the liquid-argon storage dewar, the liquid-nitrogen storage dewar, and the main cryostat housing the calorimeters. As shown in Fig. 2.1, the nitrogen and argon dewars are situated outside the main experimental hall ("M-WEST"). Argon and nitrogen liquids are transferred from their respective dewars to the cryostat via cryogenic transfer lines; the argon passes through a stainless-steel mesh filter to eliminate any large foreign elements in the liquid.

Argon purity can be checked directly from the shipping truck or sampled from the cryostat. This is done by transferring argon to a small dewar that contains a known radioactive source, and comparing the observed signal with the expected result from the source. If a shipment of argon fails to meet the 0.6 ppm O_2 allowed upper limit, the liquid is returned to the vendor.

Conceptually, the main cryostat can be divided into two sections; a warm top region and a cold bottom region. The top is at room temperature and therefore contains only argon gas. The bottom is filled with the liquid argon and is separated from the top by ~ 3 ft of special insulation. Positioned just below the insulation are four copper cooling coils encircling the circumference of the cryostat. The cooling coils are separated into groups of three and one, with each group supplied by a different nitrogen pot. The group of three supply ~ 18 kW of cooling power and are used for obtaining the maximum cooldown rate. The

other coil, known as the operating coil, is used to maintain a constant pressure head once the cryostat is filled. The rate of cooldown is essentially manually controlled, while operating pressure is maintained by an automatic feedback control system that regulates the flow of liquid nitrogen, thereby maintaining a constant argon head pressure.

The cooldown of the LAC proceeds by flowing argon gas into the cryostat and cooling the gas with liquid nitrogen circulating in the copper coils. Gaseous cooling was chosen over liquid cooldown because gas flows easily through the layers of detectors providing uniform cooling with minimal temperature gradients. The temperature of the LAC was monitored continuously using thermocouples placed throughout the cryostat and on the calorimeters, to ensure that large gradients did not arise. Temperature gradients can cause warping of the calorimeter elements that can damage the detector. During cooling, as the temperature decreased, thereby causing the gas pressure to drop, additional argon gas was added to maintain slight overpressure in the cryostat. The temperature on the front of the electromagnetic calorimeter, measured as a function of time from the start of cooldown, is shown in Fig. 2.11. The temperature difference between layer 33 and the front of the detector is shown in Fig. 2.12. As seen from these two plots, the cooldown took about 3 weeks, with a maximum temperature difference between the inside and the outside of the detector never surpassing 10°K .

When the maximum temperature inside the LAC was within 10°K of 88°K , liquid argon was introduced directly into the cryostat. At the bottom of the electromagnetic calorimeter, triangular copper fins were attached to copper sheets

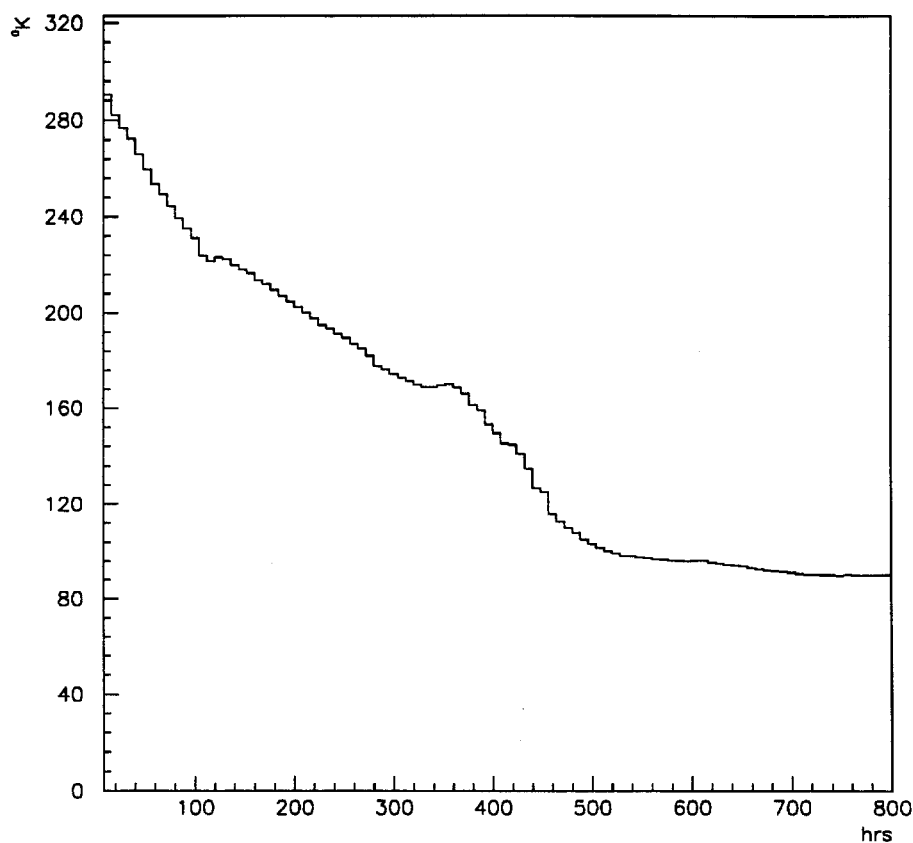


Figure 2.11 Temperature of the front G-10 plate plotted as a function of time from the start of the cooldown process. The flat levels at 125 and 325 hours into cooldown indicate times at which cooldown was stopped in order to allow the temperature of the detector to equalize.

that covered the front and back of the detector. These fins provided a safety margin in that the liquid level could be slowly raised until the fins were partially submerged in the argon. Subsequently, liquid could be added without causing excessive thermal shock to the rest of the detector.

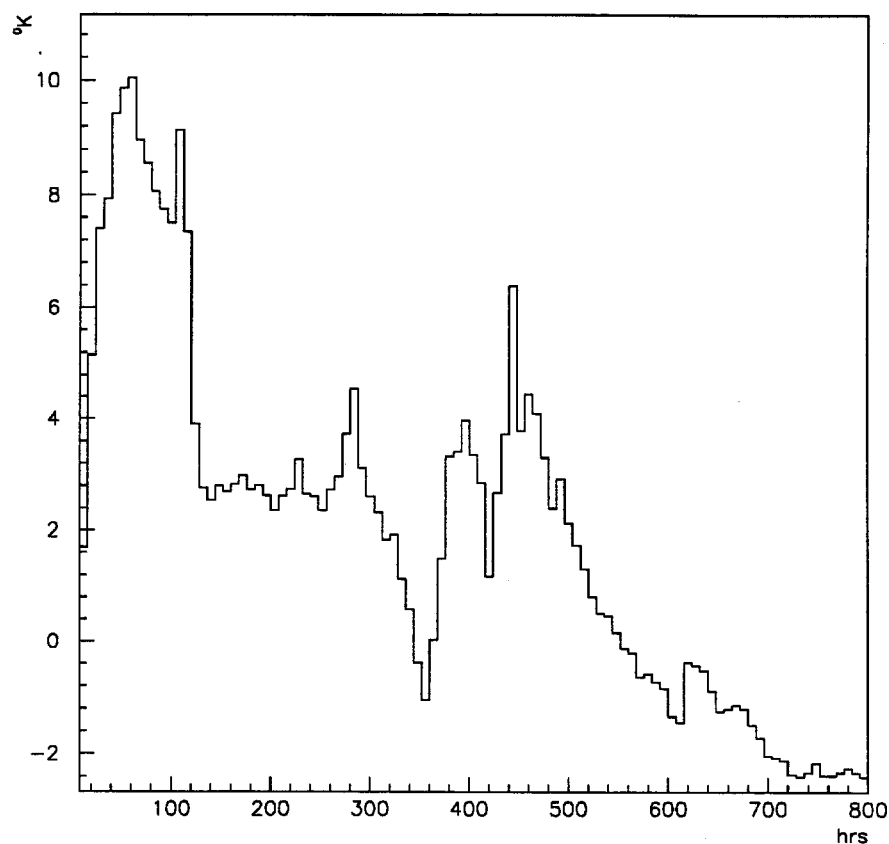


Figure 2.12 Temperature difference between the front G-10 plate and layer 33 plotted as a function of time from the start of the cooldown process.

2.4 FORWARD CALORIMETER

The forward calorimeter (FCAL) consists of three independent modules. The purpose of the FCAL is to cover the beam-hole region of the EMLAC and HLAC. All modules are identical, and each consists of thirty two layers of alternating sheets of steel and scintillator. It is of circular construction and has an outer radius of 57 cm with a 3.175 cm beam hole.

Each steel plate is 1.9 cm thick and has 76, 1.27 cm diameter, holes drilled into it for wave shifter rods. The scintillator is 0.46 cm thick and has 1.1 cm diameter holes for the wave shifter rods. The holes in the steel were made larger to compensate for relative expansion of the plastic due to temperature and humidity variations. Each wave shifter rod is connected to a photomultiplier tube which is read out via a flash analog to digital converter (ADC). The wave shifter rods are made of acrylic, doped with an organic dye, BBQ^[21], which shifts light from the blue to the green part of the spectrum where the photomultiplier tubes operate. The wave shifter rods are also doped with an ultraviolet absorbing agent which absorbs any Cherenkov light caused by the passage of hadrons through the length of the rod.^[22]

3. Operation of the LAC

Energy is deposited in the two calorimeters through electromagnetic interactions. Though the physics by which the incident particle energy is converted to the energy of a multi-particle shower differs for the two calorimeters, the method through which the energy is read out is identical. In what follows, I will describe how a shower develops in the EMLAC, how an event is triggered, and lastly how it is read out.

3.1 SHOWER EVOLUTION AND CHARGE COLLECTION

The calorimeters used in this experiment are known as sampling calorimeters. A sampling calorimeter is characterized by alternating layers in which the functions of energy measurement and energy degradation are separated.^[23] The corresponding layers for our detector are the G-10 anode boards and lead plates respectively. Electromagnetic showers are initiated by either photons or electrons incident on the EMLAC. Above 1 GeV, the radiative energy loss mechanisms of pair creation and Bremsstrahlung become energy independent and dominate over the processes of ionization loss and Compton scattering.^[24] Since Bremsstrahlung and pair creation dominate initially, a multitude of lower energy electrons and photons are produced. The shower cascade continues to develop until the average energy of the produced particles becomes low enough so that ionization losses dominate. Electrons in the shower ionize argon atoms, producing low energy electrons which subsequently drift across the argon gap under the influence of the electric field produced by the high voltage on the lead plates to be collected on the copper strips of the G-10 anode boards. For our detector configuration, about 20% of the energy is deposited in the liquid argon.

The amount of charge collected is proportional to the incident energy, the argon gap thickness, and the mean free path length for absorption of electrons by impurities in the argon. The theoretical expression^[25] is

$$Q = Q_0 \frac{2\lambda}{D} \left[1 - \frac{\lambda}{D} \left(1 - e^{-\frac{D}{\lambda}} \right) \right] \quad (3.1)$$

where Q is the detected charge, Q_0 is the available charge to be collected, λ is the mean free length and D is the argon gap thickness. Q_0 is given by the relation

$$Q_0 = e \frac{dE}{dx} \frac{D}{W} \quad (3.2)$$

where W is the typical energy required to ionize an atom in liquid argon and $\frac{dE}{dx}$ is the energy loss per unit length to ionization. The parameter λ is directly proportional to the electric field strength and inversely proportional to the impurity concentration p ; mathematically the relation is

$$\lambda = \alpha \frac{|E|}{p}. \quad (3.3)$$

By plotting the collected charge versus the electric field strength, we can measure the contamination present in any sample of liquid argon in equivalent ppm of oxygen, by fitting Eq. (3.1) to the data. This procedure was used to determine whether to accept argon shipments from the vendor and to monitor the argon purity during the filling of the LAC. Argon purity measurements were also taken over the extended time the LAC remained filled in order to determine the necessity of refilling the LAC for the next run as well obtaining data for future experiments. Between filling and emptying of the LAC, which

corresponded to approximately 26 months, the oxygen-equivalent contamination increased from 0.6 ppm to 1.8 ppm. This change reflected a 15 % drop in signal.

3.2 DATA ACQUISITION SYSTEM

The data acquisition system used for writing events to tape consisted of one Microvax 2000, running VAXONLINE software,^[26] four Digital PDP-11/45's and two tape drives. The PDP's controlled the collection of event information from the different detectors. One PDP was used for each of the following tasks: the tracking system, the liquid argon calorimeters, the forward calorimeter and E672*. The microvax concatenated the information from the PDP's to form one complete event, which was then written to tape.

The VAXONLINE software was developed by the Fermilab computer department. The main components of this package included GLOBAL MENU, EVENT BUILDER, RUN CONTROL, CONSUMER, DISPLAY, and OUTPUT. GLOBAL MENU is a menu driven routine that allows access to the rest of the VAXONLINE system. EVENT BUILDER is the software which controls the gathering of subevents from the four PDP's, concatenates the data into one event, and then writes the event to the event pool. RUN CONTROL has the control over the initiation and termination of data runs as well as the capability of suspending the run for a finite amount of time. CONSUMER is essentially a shell routine, in which user-routines can be imbedded. The purpose of consumer is to periodically extract events from the event pool for online monitoring of detector performance. This is done by filling diagnostic histograms, which

* E672 is another experiment located downstream of E706 in the MWEST hall. Data was collected cooperatively between the two experiments.

can be displayed using DISPLAY. OUTPUT is the routine that writes events from the event pool to data tape. Several drives can be used, with OUTPUT switching to another drive when a tape is full, thereby eliminating the wait for tape rewind and loading.

3.3 TRIGGER

The trigger used on this experiment was designed to run at 10^6 interactions per second. It was designed to select events on the basis of transverse momentum observed in the EMLAC. To obtain an estimate of p_T , the energy in each radial strip is weighted according to its radial distance from the beamline. The triggering process takes place in three steps:

- Beam particle definition
- Interaction definition and selection
- Final event selection.

A complete description of the trigger and its performance is given in the PhD dissertation by C. Yosef of Northeastern University;^[27] here I will give only a brief description of the system.

The beam definition makes use of two scintillation counters located upstream of the target. A beam particle is accepted if both counters have a signal in coincidence with one another.

Four scintillation counters, located downstream of the target and covering the acceptance of the spectrometer, are used in the definition of an interaction. The OR of the four counters is taken in coincidence with the beam definition

to define an interaction. After an interaction is defined, it then must pass the following criteria:

- No other interaction can occur within ± 60 ns of the current one.
- The interaction is not initiated by a particle in the beam halo; namely there is no signal in the "halo" scintillation counter located near the two upstream counters. This counter has a hole cut out of its center and its signal is taken in anticoincidence with the interaction definition.

After all above requirements are met, an interaction strobe is generated to be used in the definition of the pretrigger.

A global p_T signal was generated for each octant of the EMLAC based on the weighted energy sum mentioned above. If the global p_T was greater than ~ 1.7 GeV/c, an octant signal was generated. The OR of all octants was then formed in coincidence with the interaction strobe, and in anticoincidence with the AND of the two veto walls located upstream of the target. The octant signal was also used in anticoincidence with the SCRKILL; to eliminate coherent noise generated by the power supply used for the LAC electronics. This final step determined whether a PRETRIGGER was produced. If the PRETRIGGER was produced, a signal was sent to the BATs to generate the before/after signal (this is described below), otherwise the trigger was reset for accepting another interaction.

Because several low- p_T photons can combine to generate a global p_T signal, an additional local- p_T requirement was introduced. The local p_T signal was defined as the sum of sixteen contiguous channels, or approximately one-photon shower width. Both of the two p_T signals were discriminated using two threshold

levels, called the high and low threshold. Using these two p_T and two threshold requirements, the following four LAC triggers were formed: LOCAL GLOBAL HI, LOCAL GLOBAL LO, SINGLE LOCAL, and TWO GAMMA. The LOCAL GLOBAL HI was formed by the AND of the lower-threshold local- p_T signal and the higher-threshold global- p_T signal. The LOCAL GLOBAL LO was formed by the AND of the lower-threshold local- p_T signal and the lower-threshold global- p_T signal. The SINGLE LOCAL was formed when the higher -threshold local- p_T signal was generated. The TWO GAMMA trigger required that octant A and octant B, diametrically opposite octant A, or either neighbor of octant B, have low-threshold local- p_T signals.

If one of the above LAC triggers was produced, a signal was sent to the PDP to initiate the reading out of the event. If no LAC triggers were generated, a reset signal was sent to the various electronics modules. The trigger then waited $\sim 5\mu s$ before enabling itself for the next event.

3.4 READOUT ELECTRONICS

Once the event is triggered, it must be successfully read out by the LAC electronics. The key connection in this path is the Redundant Analog Bus Based Information Transfer (RABBIT) system. The four components of the E706 RABBIT system are the liquid argon calorimeter amplifiers (LACAMPs), the EWE crate controllers, the before after timer (BAT) module, and the MX data acquisition sequencers.^[28] The amplifiers are mounted in the RABBIT crates, located around the top of the LAC cryostat. Each crate has twenty amplifier boards, two EWEs, and one BAT. Though each MX can control a maximum of eight EWEs (four crates), we configured our system using three crates per

MX. A complete description of the readout electronics can be found in the PhD dissertation by D. Skow from the University of Rochester (Ref. 28); here I will present the main components and what their role is in the reading out of an event.

LACAMP

Each amplifier board contains sixteen amplifiers for the sixteen channels associated with the cable connected to that board. In addition to the obvious requirements of stability and low noise, the LACAMPs need low input impedance and remote calibration capability (Ref. 28).

A fast output from the LACAMPs is used in forming the trigger while another signal from the LACAMP enters an 800 ns delay line. If the pretrigger is satisfied, the BAT sends a signal to the sample and hold and TVC. The sample-and-hold opens a relay which stores voltages on capacitors. The TVC produces a voltage signal that is proportional to the time difference between the LACAMP pulse and the signal from the BAT. If the pretrigger was not satisfied, the event is rejected. This all happens within the 800 ns of the delay line. The charge is collected and retained in the sample-and-hold until it is addressed by the EWE.

EWE

Each EWE is controlled by an MX processor. The purpose of the EWE is to address each amplifier and collect the signal from the sample-and-hold and the appropriate TVC. The signal is digitized by an analog-to-digital converter (ADC) on each EWE. This has the advantage that all pulse heights from channels on half a crate are converted using the same ADC, thereby reducing

channel-to-channel systematic variations from different ADCs. The signal is then compared to a predefined threshold, and if it is above this value, the EWE informs the MX that it has a signal to be read out.

PDP/MX

When a PDP receives a signal from the trigger indicating the event is accepted, it informs the MXs to start gathering event information in one of their four buffers. The MX signals the EWE that it can start addressing the amplifiers. The values of all addresses with signals above threshold are stored in the MX buffer. The same buffer in all the MXs is used for any given event. If the MXs have any empty buffers, the PDP will enable the trigger for the next event, otherwise it will wait until it finishes reading out one buffer, enable the trigger for the next event, and then proceed to read the remaining buffers.

4. Event Reconstruction

4.1 OVERVIEW

This chapter describes the offline reconstruction package used in this experiment. The overall control program, written in FORTRAN, is called MAGIC. The MAGIC code does the following:

- reads in primary or reconstructed data (or a combination of the two)
- unpacks primary data
- calls the individual reconstructor subroutines (one per detector element)
- outputs the analyzed, unpacked, and/or primary data.

User control cards determine the specific actions that MAGIC will execute and which data will be written out to the Data Summary Tapes (DSTs).

MAGIC uses the CERN code-management system known as PATCHY.^[29] With PATCHY, a program can be broken up into many separate pieces called patches, which in turn contain smaller pieces of code called decks. PATCHY code, is not FORTRAN code which can readily be compiled. In order to compile MAGIC one must first generate a FORTRAN file using PATCHY commands. At this point, any or all of the patches can be selected for the FORTRAN file, with the stipulation that any single patch is included whenever it is required in other patches.

PATCHY flags can also be used to turn on and off certain sections of code as desired. This provides the possibility for writing code that can be run on different computers merely by choosing the correct set of flags at the time the

FORTRAN file is generated. This is an important feature since we used the following machines in the processing and analyzing of the data:

- VAX: used for program development and debugging
- ACP^[30] (Advanced Computer Project): main data processing
- Amdahl: data analysis at the DST level.

Since standard FORTRAN does not provide dynamic memory management, we adopted the CERN memory management system known as ZEBRA^{[31][32]} for E706. ZEBRA provides the possibility of having data banks of variable size, depending upon the requirements of any particular event. Each bank can be increased or decreased in size as needed, thus conserving the overall memory used for any event. Data banks created using ZEBRA can be easily manipulated between "divisions"; the divisions containing only the desired banks can be kept and subsequently written out. ZEBRA output data is available in machine-independent format, which is a clear necessity for our complex computer environment.

4.2 TRACKING RECONSTRUCTION

The reconstruction package for the tracking system is known as PLREC. A complete description of the algorithm is given in the PhD dissertation of S. Easo of Pennsylvania State University.^[33] Because of the vertex requirements we imposed in our data analysis, we will describe some of the main features of PLREC. The algorithm reconstructs the upstream tracks (from SSD's) and the downstream tracks (from PWC's) independently. An attempt is then made to link an upstream and downstream track, taking into account the field strength

of the analysis magnet, to form the full trajectory. Track information, such as momentum, charge, etc ... is then stored in the proper data banks, to eventually be written out to DSTs.

The first step in reconstructing downstream tracks is to form view tracks in each of the four views (X, Y, U, V). A view track is found by first choosing two seed planes and two search planes in each view. A hit from each seed plane is selected to determine slopes and intercepts of straight lines. All possible combinations of points from the two seed planes are used for this purpose. The two remaining search planes for each set of seed planes are searched for hits that fall within ± 1.5 wire spacings of the line, as projected to that plane. If each search plane has a hit that satisfies this criterion, the track is termed a four-hit track. If only one of the search planes has a hit that falls near the line, the track is a three-hit track. If no matches are found in the search plane for the seed points then no view track is made. This procedure is done in two passes. The first pass is done with the two outer planes being the seed planes while the second pass is done interchanging the seed and search planes. The second pass is executed to find three-hit tracks for tracks with a hit missing in one of the outer planes; the first pass is able to handle the other three-hit tracks and all four hit tracks.

Once all possible projected tracks are found for each view, the code proceeds to match view tracks to form space tracks. The procedure is similar to that used above. Two seed views are chosen. A track from each seed view is assumed to come from a space track. The candidate space track is projected onto the two search views. The hits in each search view are compared to the projected hits

of the space track. All hits which fall within a ± 1.5 wire spacing are grouped with the hits making up the seed view tracks. This set of hits makes a space track if the following conditions are met:

- There is a minimum of two hits per search view
- There is a minimum of four hits from all search views
- There is a minimum of six hits from the seed views
- There is a minimum of thirteen hits in all.

The code for reconstruction of the projected upstream tracks follows the same procedure used for the downstream view tracks. An additional complication arises here because of for high multiplicities upstream of the magnet. To minimize CPU time for extremely high multiplicity events, nearby hits are merged to form equivalent single hits, which are then used to complete track reconstruction.

Matching of the upstream and downstream tracks is accomplished by projecting, for each downstream space track, all upstream space tracks to the center of the magnet. The spatial difference of each pair is compared to find the best match. If this best match passes a predetermined cut, it is selected as a linked track. The charge and momentum of the linked track is given by

$$q = \frac{\theta_1 - \theta_2}{|\theta_1 - \theta_2|} \times \frac{B}{|B|} \quad (4.1)$$

$$\sqrt{p_x^2 + p_z^2} = \frac{qBL_0}{\sin(\theta_1) - \sin(\theta_2)} \quad (4.2)$$

$$p_x = p_z \tan(\theta_1) \quad (4.3)$$

$$p_y = p_z \tan(\theta_y) \quad (4.4)$$

where q is the sign of the charge of the particle, B is the field strength, L_0 is the length of the magnet, p_x , p_y , and p_z are the three components of the momentum, θ_y is the angle of the particle trajectory relative to the z axis in the yz plane, and θ_1 and θ_2 are the angles, relative to the z axis, at the exit and entry points of the magnet region, in the xz (bend) plane.

The final step in the tracking algorithm involves the reconstruction of the event vertex. To assure a reliable procedure for vertex finding, only tracks with at least four hits upstream of the magnet, that are properly linked to downstream tracks, are used. If no such tracks are available, the code searches for any four-hit tracks upstream of the magnet (releasing the linking requirement). If there are at least four such tracks, then they are all used in defining the vertex. Finally, if fewer than four such tracks are found, the code uses all three-hit linked tracks to locate the vertex.

The vertex is obtained from a χ^2 minimization procedure, wherein the slopes and intercepts of the individual tracks are used to locate the spatial point that minimizes the average impact parameter of the trajectories relative to that point. The minimization procedure is iterated until the average impact parameter of all tracks used to define a vertex is less than $20\mu\text{m}$, or until the largest impact parameter is less than $50\mu\text{m}$, or until there are only two tracks left.

4.3 ELECTROMAGNETIC-SHOWER RECONSTRUCTION

The reconstruction code for the electromagnetic section of the LAC is called EMREC, and its functions can be broken down into four main parts. The first part, executed for each of the four views (left R, right R, inner Φ , and outer Φ) of a calorimeter quadrant, deals with finding groups of channels (strips) that contain significant energy deposition. In the second part, the code reconstructs GAMMAS from energy peaks detected in each view. The GAMMAS represent an intermediate step in the final photon reconstruction, and differ from peaks in that they correspond to fits to photon shower shapes for determining energies and positions. The third part deals with the correlation of GAMMAS from different views to form the final photons. Finally, the photon time of arrival is obtained from the TVCs.

As mentioned previously, the EMLAC consists of a front and back section, which are read out independently. For reconstruction purposes, corresponding strips in the front and back are added together to form a software summed section. This is done to minimize the dependence of the shower shape on the longitudinal origin of the shower. All final reconstruction is performed on these summed energies. As we will see, however, front and back sections contain additional valuable information on radial positions, as well as on the ratio of energy deposited in the front and back sections of the EMLAC (E_{front}/E_{back}). We will now examine each part of EMREC in more detail.

Group and Peak Finding

Each quadrant can be thought of as consisting of four independent views. Views one and two are the radial readout sections corresponding to $\phi < 45^\circ$

and $\phi > 45^\circ$ respectively. These two views will also be referred to as the left-R and right-R views. Views three and four correspond to the inner and outer Φ regions described in Section 2.3. For any particular view, a group is defined as a series of consecutive strips with energy above a predefined threshold. For a sequence of strips to be called a group, they must pass the following criteria:

- For views 1, 2, and 3, there must be at least 3 strips above threshold. For view 4, this requirement is reduced to 2 strips, due to the widening of strips at large radius.
- The total group energy must be greater than 750 MeV.
- The average energy per strip must be greater than 150 MeV.
- The strip with the maximum energy must contain more than 300 MeV.

Once all these conditions are met, the group is stored in a designated data bank and the code starts the search for peaks.

A peak candidate is established when the slope of the energy distribution as a function of strip position in the group changes from a positive to a negative value. Associated with each candidate are two valleys located at either side of the peak. A valley is defined as the strip with the lowest deposited energy between two peaks, or the end strip in the group if the peak is the first, last or only peak in the group. Because adding front and back energies tends to lose low energy peaks in the front section, a search is performed to locate peaks in the front section between any two valleys already found in the summed energy distribution. If a candidate for a peak strip is found in the front section, we

calculate its significance using the formula

$$\sigma^2 = (0.14)^2 E + (0.1)^2 \quad (4.5)$$

where E is the energy of the peak-strip in the front section, and σ is the estimate of the standard deviation of that energy. Two quality factors are calculated in terms of the energy difference between the peak-strip and its left and right valleys, divided by σ . If the quality factors pass a 2.5 standard deviation cut, the candidate is accepted as a real peak and not as an energy fluctuation. If no peaks are found in the front section, the quality factors are calculated using the peak-strip energy in the summed section and the valleys, also found in the summed section. In either case, the peak is stored with an associated energy equal to the sum of strip energies between its valleys (for the summed section).

For each peak found in the front of the LAC, we sum the energy in the strips between the peak's front valleys (these are not necessarily the same valleys as found in the summed section). If the view in which the peak is found is a radial view, we calculate its front radius, and search for a corresponding peak in the back section of the LAC to obtain its back radial position. The difference between the back radius projected to the front and the front radius, is known as directionality. The value of directionality yields information about whether or not a particle's trajectory intersects the target region. Since a difference between ϕ positions in the front and back does not yield directionality information, we do not search for separate front and back peaks in the Φ view.

GAMMA Reconstruction

The reconstruction of a GAMMA from a peak depends on the type of group

involved. A single-peak group is straightforward in that the position and energy calculations are unambiguous. A multiple-peak group must first be split into equivalent one-peak groups, before GAMMA positions and energies can be calculated. The following paragraphs will describe the shower shape, position algorithm, energy algorithm, and splitting algorithm for GAMMAS .

Shower shape information is needed for extracting the position and energy of any single GAMMA from an overlap of several showers. The individual shower shapes are parametrized by

$$E_f(r) = \frac{1}{r} \left(f_1 e^{-f_2 r} + f_3 e^{-f_4 r} + f_5 e^{-f_6 r} \right) \quad (4.6)$$

for the front and

$$E_b(r) = b_1 e^{-b_2 r} + b_3 e^{-b_4 r} + b_5 e^{-b_6 r} \quad (4.7)$$

for the back of the LAC. In these equations, r is the radial distance from the shower center; the fitted parameters f_1 through f_6 , and b_1 through b_6 are listed in Table 4.1. The factor of $\frac{1}{r}$ is used in the front section to fit the steep r -dependence of the shower; in the back, the shower is more developed and therefore broader. The parameters f_1 , f_3 , f_5 , b_1 , b_3 , and b_5 are normalized at the initialization of EMREC such that the integral of the shape is equal to 1 GeV. The energy in the summed section is taken as $E_{sum}(r) = E_f(r) + E_b(r)$.

The energy-independent shower shape was determined by fitting energy deposition from GEANT^[34] Monte Carlo events to the above form. The shape was also compared to data from electron showers produced in the EMLAC, and the two were found to be consistent. During the initialization of EMREC, the

shower shape is used to fill two arrays. The first array contains the energy deposited in 0.05 cm strips in the front section. The second array contains the same information for the back section.

Front		Back	
f_1	0.49298	b_1	0.04257
f_2	1.0363	b_2	0.43745
f_3	0.02041	b_3	0.87951
f_4	0.33934	b_4	1.3606
f_5	0.34628	b_5	3.5412
f_6	9.0071	b_6	5.8467

Table 4.1 Shower shape parameters.

The position of the GAMMA is calculated in two approximations. The first approximation uses the middle of the peak-strip. For the radial views the i^{th} strip is given by

$$r_i = 20.2233 \text{ cm} + i \times w(k) \quad (4.8)$$

and for the Φ views, the angle for the i^{th} strip is

$$\phi_i = (i - 1) \times w(k) + (quad - 1) \times \frac{\pi}{2} \quad (4.9)$$

where $w(k)$ are the widths of the strips in R [$w(1) = w(2) = 0.5466 \text{ cm}$] or in Φ [$w(3) = 2 \cdot w(4) = 0.0164 \text{ radians}$], and $quad$ refers to the quadrant number of the EMLAC. The second calculation uses weighting based on pulse-height values of the position of the GAMMA within the peak-strip. The shift from center

is determined by the energies in the three strips centered on the peak strip. Different combinations of these three energies were examined to find a variable nearly linear to the offset from the center of the strip. The first estimate for this offset in the radial view is given by

$$X = 1.702 \left[\frac{PH_3 - PH_1}{PH_3 + PH_1} \right] \quad (4.10)$$

where PH_1 and PH_3 are the energies on either side of the peak strip. For the Φ views, a factor that depends on the estimated radial position is used in place of the 1.702 value in the above equation.

After determining this first approximation to the center, three fits are performed to the shower shape with centers at the three values of $X - 0.2$, X , $X + 0.2$. The χ^2 values of the fits for these three points are used to find the minimum χ^2 , which determines the best estimate of the center of the shower.

The energy of a GAMMA is found from minimizing the χ^2 of the fit of the pulse distribution to the shower shape. In order to prevent noise in the tails of the showers from adversely influencing the fit, the number of strips (N_{strips}) used in the fitting procedure was restricted. Clearly, the number of strips used must depend on the total energy in the strips. The value of N_{strips} is determined by the energy in the three central strips. For the Φ views, the number of strips, used to find the energy to calculate N_{strips} , is adjusted so that the total width in centimeters corresponds to 3 strips in the radial view. The energy in these strips is then summed. This sum is then used to calculate the number of strips to be used according to the formula

$$N_{strips} = 15 + 0.2 E. \quad (4.11)$$

The parameters in this relation were determined through Monte Carlo studies, in which N_{strips} was shown to be an appropriate number of strips that could be used without having energy fluctuations in the edges of the shower qualitatively affecting the χ^2 of the fit.

Once the number of strips is determined, the χ^2

$$\chi^2 = \sum_i \frac{1}{\sigma_i^2} (e_i - Ez_i)^2 \quad (4.12)$$

is minimized with respect to the true GAMMA energy E . Here e_i is the energy in strip i , z_i is the fraction of energy in strip i predicted from the shower shape, and σ_i is the standard deviation of the energy for the i^{th} strip (i.e. $\sigma_i^2 = 0.0196e_i + 0.01$). The χ^2 can be expressed as

$$\chi^2 = A - 2BE + CE^2 \quad (4.13)$$

where

$$A = \sum_i \frac{e_i^2}{\sigma_i^2} \quad (4.14)$$

$$B = \sum_i \frac{e_i z_i}{\sigma_i^2} \quad (4.15)$$

$$C = \sum_i \frac{z_i^2}{\sigma_i^2}. \quad (4.16)$$

Also of interest, for reasons given below, are the sums

$$D = \sum_i z_i \quad (4.17)$$

$$E = \sum_i e_i \quad (4.18)$$

The fitted energy is given by the minimum of the quadratic χ^2 , $E_{fit} = \frac{B}{C}$. The

amount of energy in the tails of the shower is computed to be $E_{tail} = E_{fit}(1 - D)$. The energy given by the sum of the strips is $E_{sum} = E + E_{tail}$. If the $\chi^2_{/dof}$ is less than 5.0, the fit is deemed acceptable, and the fit-related quantities are stored, otherwise only the summed-energy results are stored in the GAMMA banks.

For multiple-peak groups, the situation is somewhat more complicated. The procedure is first to split the group into separate showers and then perform the position and energy calculations on the corrected pulse distribution.

To split the group, a rough position and energy estimate is made for each peak. These estimates are used in finding an energy for the GAMMAS by minimizing the χ^2

$$\chi^2 = \sum_i \left(e_i - \sum_k E_k z_k^i \right)^2 \quad (4.19)$$

where e_i is the energy in the i^{th} strip, E_k is the true energy of the k^{th} GAMMA, and z_k^i is the fraction of energy from the k^{th} shower in the i^{th} strip. The minimization is done by setting $\partial\chi^2/\partial E_l$ to zero. This implies that for each shower

$$\sum_i \left(e_i - \sum_k E_k z_k^i \right) z_l^i = 0,$$

$$\sum_i \sum_k E_k z_k^i z_l^i = \sum_i e_i z_l^i.$$

We can write this as the matrix equation

$$E \times S = V$$

where

$$S_{kl} = \sum_i z_k^i z_l^i$$

$$V_l = \sum_i e_i z_l^i$$

and E is the array of energies. To obtain the solution E , we must invert the matrix S and multiply by V such that

$$E_k = \sum_l S_{kl}^{-1} V_l . \quad (4.20)$$

In the event that the matrix is not invertible, the peak of lowest energy is dropped from the group and another attempt at splitting is made.

Once the energies of the individual GAMMAS are known, they are used to calculate the corrected pulse height distributions. The new values obtained are given by

$$PH_i = e_i - \sum_j E_j z_j^i \quad (4.21)$$

where PH_i is the corrected energy in the i^{th} strip and the other values are as previously defined. After the new strip energies are found, we check whether or not the peak strips are located at the same positions. If not, we define new peaks, and, in either case, recalculate the positions of the peaks since the pulse height values have changed. The energies are then calculated using the same algorithm as the one used for the single-peak group case. At this point one more fit is done to the shower shape using the fitted energies to obtain the GAMMA position. The final χ^2 is

$$\chi^2 = \sum_i \left(\frac{e_i - \sum_k E_k z_k^i}{\sigma_i^2} \right)^2 \quad (4.22)$$

where the σ_i^2 are calculated based on the total contribution from all GAMMAS to that strip.

Correlation

Once all the GAMMAS are reconstructed, they are correlated to form the final photons. The correlation procedure, though very complicated in practice, is straightforward in conception. Remember that the G-10 readout boards alternate between radial (R views) and azimuthal (Φ views) boards. A photon will therefore deposit roughly the same amount of energy in each view. Since the shower development is identical for each view, the E_{front}/E_{tot} ratios will be the same. The idea is to match a GAMMA from one view with a GAMMA in another view that has approximately the same energy and E_{front}/E_{tot} ratio. There are some requirements that improve the matching, such as requiring that the inner Φ GAMMAS only correlate with R GAMMAS that have a radius less than 40 cm, and outer Φ GAMMAS correlate with R GAMMAS with a radius greater than 40 cm. Additional problems arise when a GAMMA falls near the inner/outer Φ boundary, the octant boundary, or a combination of these boundaries. In Chapter 5 we will see the effects of these problem areas on the reconstructed π^0 mass.

The first step in the correlation procedure is to identify which GAMMAS are near the boundaries. This is done by comparing the first and last strips of all groups to see if any are across the boundary. If so, the amount of energy on each side is summed, and if both sides are above 1.5 GeV, the GAMMA closest to the boundary is identified. If the distance of this GAMMA to the boundary is less than some minimum distance, the view is flagged as having a boundary GAMMA. The minimum distance is 5.0 cm for R views, and 0.16 rad/0.08 rad for the inner/outer Φ views.

The correlations for boundary GAMMAS are done first. The worst correlation would be for one GAMMA on the boundary with two GAMMAS from the other views. For example, one R boundary GAMMA could be correlated to an inner Φ and an outer Φ GAMMA. Likewise, a Φ boundary GAMMA can be correlated to a left R and right R GAMMA. The other possibility would be a two and two correlation, in which the boundary view has two GAMMAS near the boundary that are correlated with two GAMMAS from two other views. In the steering routine for correlation, the energy and position restrictions are incremented by

$$\left(\frac{E}{\sigma}\right)_{max} = i \times 0.5 \quad (4.23)$$

$$SEP_{max} = i \times 0.3 \quad (4.24)$$

where i is the iteration number, $\left(\frac{E}{\sigma}\right)_{max}$ is the maximum number of allowed standard deviations for the energy difference between the correlating GAMMAS and SEP_{max} is the largest spatial separation allowed for the two GAMMAS in cm. Up to ten iterations are tried for Eq. (4.24) while 15 iterations are allowed for Eq. (4.23). The general procedure for each routine can be seen by the following example. Let the boundary view be one of the R views, then the correlation routine loops over the two Φ views comparing the energy difference, taking into account the E_{front}/E_{tot} , between the R view GAMMA and the sum of the Φ view GAMMAS. Mathematically the correlation procedure is

$$\sum_{R_{bound}} \left(\sum_{\Phi_{inner}} \left(\sum_{\Phi_{outer}} E_{diff} = \frac{W_f}{\sigma_f} |EF_R - EF_{\Phi_i} - EF_{\Phi_o}| + \frac{W_b}{\sigma_b} |EB_R - EB_{\Phi_i} - EB_{\Phi_o}| \right) \right) \quad (4.25)$$

where

$$W_f = \frac{EF_R + EF_{\Phi_i} + EF_{\Phi_o}}{E_R + E_{\Phi_i} + E_{\Phi_o}}$$

$$W_b = \frac{EB_R + EB_{\Phi_i} + EB_{\Phi_o}}{E_R + E_{\Phi_i} + E_{\Phi_o}}$$

and σ_f is the standard deviation calculated using the sum of the GAMMA front energies and the sum of the strips each GAMMA spans in the front. σ_b is the corresponding standard deviation in the back. It should be mentioned here that \sum used in Eq. (4.25) represents a looping over the appropriate GAMMAS and not a sum. E_{diff} then measures the E_{front}/E_{tot} weighted energy difference of the correlated GAMMAS. Once the R GAMMA is matched with two Φ GAMMAS such that the standard deviation of the energy difference is less than the maximum allowed, a correlation is made. The GAMMAS are flagged and the photons are stored in their data banks. Other correlation subroutines check whether GAMMAS have been correlated, so they will not be used again.

After all correlations at boundaries are completed, the code proceeds with GAMMAS located away from boundaries. The three types of correlations attempted are one R to one Φ , one R to two Φ and one Φ to two R. The one to one correlation is simple matching of one R GAMMA to one inner or outer Φ GAMMA (depending on the radius of the R GAMMA). E_{diff} is calculated in the same way, and the energy cut is dependent on the iteration as in Eq. (4.23).

For the one R to two Φ correlation, each R GAMMA is matched with a pair of Φ GAMMAS (both inner or both outer, as determined by the R GAMMA) until E_{diff} passes the energy cut. Once a correlation is found, we attempt to split the one GAMMA using the energies of the two correlated GAMMAS. The

one Φ to two R correlation is essentially the same, but with the views reversed. Whenever a correlation is made, the photon information is stored in the photon data banks.

After all possible GAMMAS are correlated, we again reconstruct the Φ gammas using the information obtained during the correlation. This is done for the Φ view only, because a better estimate of the radial position of the gamma is available. Since the fit depends on the width of the Φ view strips, which in turn depends on the radius of the gamma, we can get a better fit using the correlated information. After the Φ gammas are refitted, we recorelate them because of the new energy values calculated. The code that does this varies little in principle from the code described above and will not be discussed further.

Photon Timing

Associated with each photon is a time of arrival, calculated using the strip TVC information mentioned in Chapter 3. In order to use the TVCs, they must first be properly calibrated. The pedestals for the TVCs are not the values that correspond to no detected signal, but instead are the TVC values corresponding to an "in-time" event. These pedestals are determined by comparing the distribution of TVC values for different before settings of the BAT (see Ch. 3) to the distribution of TVC values observed in the data. The before setting for the BAT that best duplicates the observed TVC distribution is then used to determine the value of the TVC to be used as the pedestal. Unfortunately, during data taking, the TVCs reached not more than 90% efficiency due to noise, even for strip energies above 4 GeV.^[35]

At the unpacking stage for each event, all TVCs with associated energy

of less than 4 GeV were not used. The remaining TVCs, except those that were previously flagged as being bad, were corrected for pedestal shifts. The timing algorithms used in EMREC, associate a time of arrival with each group, GAMMA, and photon.

In order to find the time associated with a particular EMREC group, we first find sets of TVCs that fall within 3 standard deviations (45 ns) of each other. Next, we do an energy-weighted average of the TVC sets, and get a unique time per set. The most reliable time is given by the set that has the greatest number of pedestal-corrected TVC values. If two sets have the same number of TVCs, then the set with the largest associated energy is chosen as providing the best time. The best and second best times found this way are stored in the group data banks. For each time, a quality factor is calculated and stored with it. The quality word is given by $1000 \times (\text{number of TVCs}) + (\text{TVC group energy})$.

Since there is a one-to-one mapping between GAMMAS and peaks, the times associated with GAMMAS are just the best and second best times of the group the peak originated in. Since photons can be constructed from as many as four GAMMAS, the photon time is found by taking the best time from each of its GAMMAS. These best arrival times are treated as original TVC signals, and the group criteria for calculating times is applied.

4.4 HADRON RECONSTRUCTION

The hadron reconstruction code is described in detail in the PhD dissertation by A. Sinanidis of Northeastern University.^[36] For completeness, we shall only describe the philosophy of the code. The reconstruction algorithm searches the

hadron calorimeter pads for clusters of pads that have energy above a threshold of 2 GeV. The minimum number of pads allowed to form a group is two. Each cluster must contain one pad that has a minimum energy of 5 GeV.

For a given cluster, one or more hadrons can be reconstructed. If the number of pads in a cluster does not exceed twelve, and if no more than three pads contain 40% of the maximum pad energy, the cluster is considered to be one hadron. If these conditions are not met, the cluster is assumed to contain more than one hadron, and additional information concerning the deposition of energy in pads by hadrons is used to separate the individual showers.

The reconstructed hadrons are corrected for losses at the edges of showers using a shape function generated from Monte Carlo. The final corrections to the hadron energy are from EMREC: that is, since hadrons can start to shower in the electromagnetic calorimeter, the hadron energies are corrected using the output from EMREC, provided they correlate in position with an electromagnetic shower.

5. Data Analysis

5.1 DATA SELECTION

Overview

The data used in this analysis were collected during the last part of the 1987 - 1988 fixed target run. Table 5.1 summarizes what was written to tape. The different data sets correspond to different beam polarities, changes in target, or to runs for which some detector was not functioning normally. Calibration runs and data taken without electromagnetic triggers are not included in the entries.

Set	Beam	Target	First run	Last run	# Runs	Triggers
A	Neg	Cu + Be	2852	3036	95	786K
B	Pos	Cu + Be	2588	2670	-	440K
C	Pos	Cu + Be	2387	2586	141	1,225K
D	Neg	Be	2062	2382	162	1,247K
E	Pos	Be	1728	2007	162	1,508K
F	Pos	C	1672	1719	-	161K

Table 5.1 Breakdown of data sets used in this analysis.

Most of the triggers for each set of runs have p_T below our analysis cut-off of 4.0 GeV/c. The event sample also contains events triggered by beam associated muons, events in which no vertex was reconstructed, or events where EMREC failed to properly correlate the GAMMAS. All such events were removed and corrected for in the cross section. Table 5.2 shows the number of events remaining, for each data set, after a minimum p_T cut was applied. The other columns

list the number of events lost upon applying the above mentioned restrictions, namely, effect of the veto wall, absence of reconstructed vertex, and the presence of large uncorrelated energy. The last column indicates the final number of events used in the analysis.

Set	# Ev above p_T	Veto Wall	Uncorr. Energy	Vertex Existence	Final # Events
A	321,861	128,715	8,444	42,281	142,421
C	205,865	157,609	1,421	9,644	37,191
D	166,967	107,634	1,875	11,457	46,001

Table 5.2 Table of the events remaining after applying various cuts. Data sets B, E, and F are not shown because they were not available for this analysis.

Veto Walls, Directionality, and Timing

The two veto walls used in this experiment were put into the trigger in a logical AND mode, that is, in order for the event to be rejected, both veto walls had to have signals. Figure 5.1 displays the correlation between the X and Y position of photons in the EMLAC that have two photon masses outside of the π^0 and η mass peaks. The figure is for events that have a signal in the region of the veto wall that shadows the photon-triggered EMLAC quadrant. A large number of entries is observed in the region of the EMLAC where beam muons are expected to be deflected. Figure 5.2 shows the same distribution as in Fig. 5.1, but for events without a hit in the veto wall shadowing the trigger quadrant of the EMLAC. The strong anisotropy observed in Fig. 5.1 is not seen in Fig. 5.2.

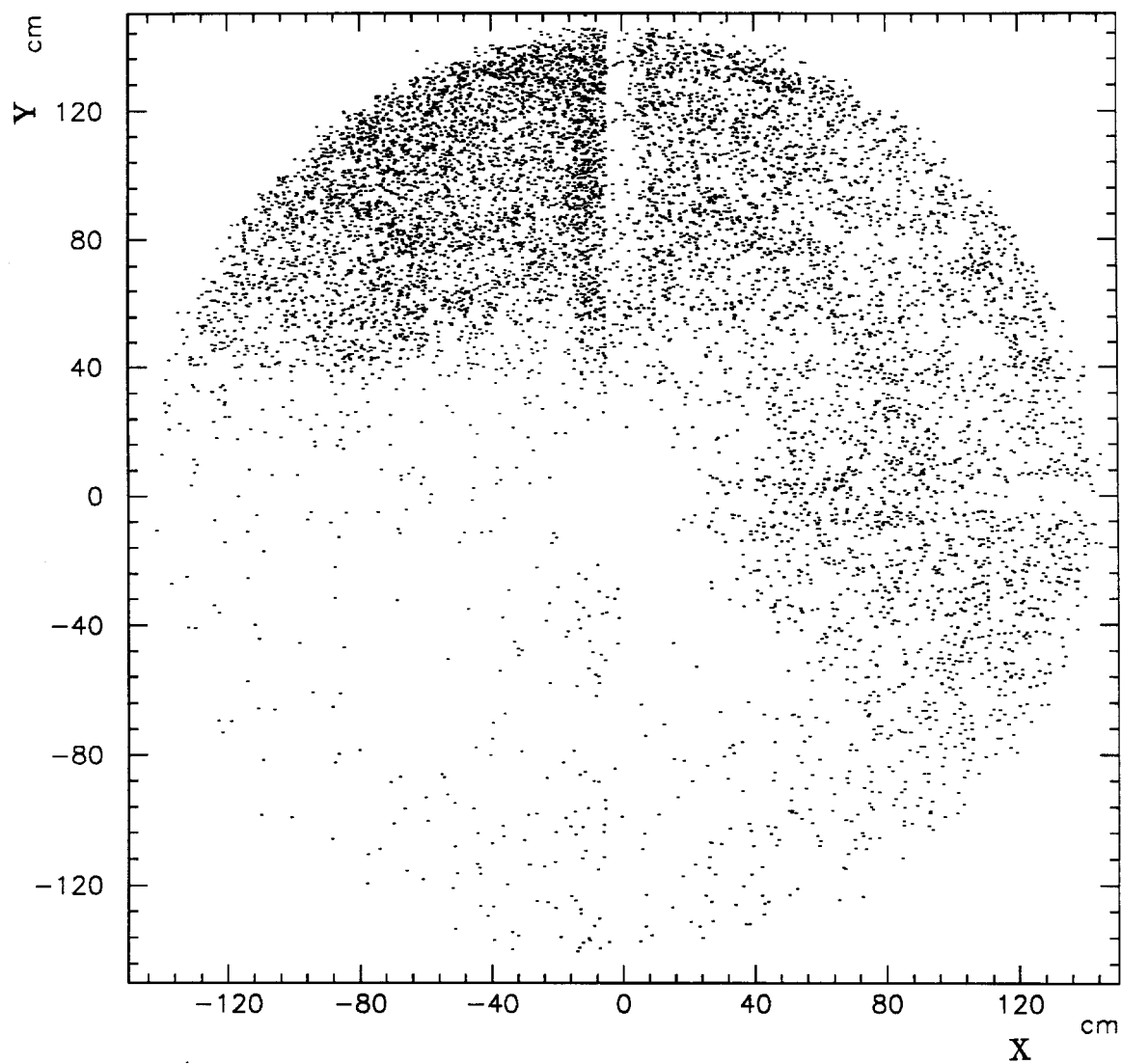


Figure 5.1 Spatial distribution of photons for events when the veto wall had a signal in the quadrant corresponding to the trigger quadrant of the EMLAC.

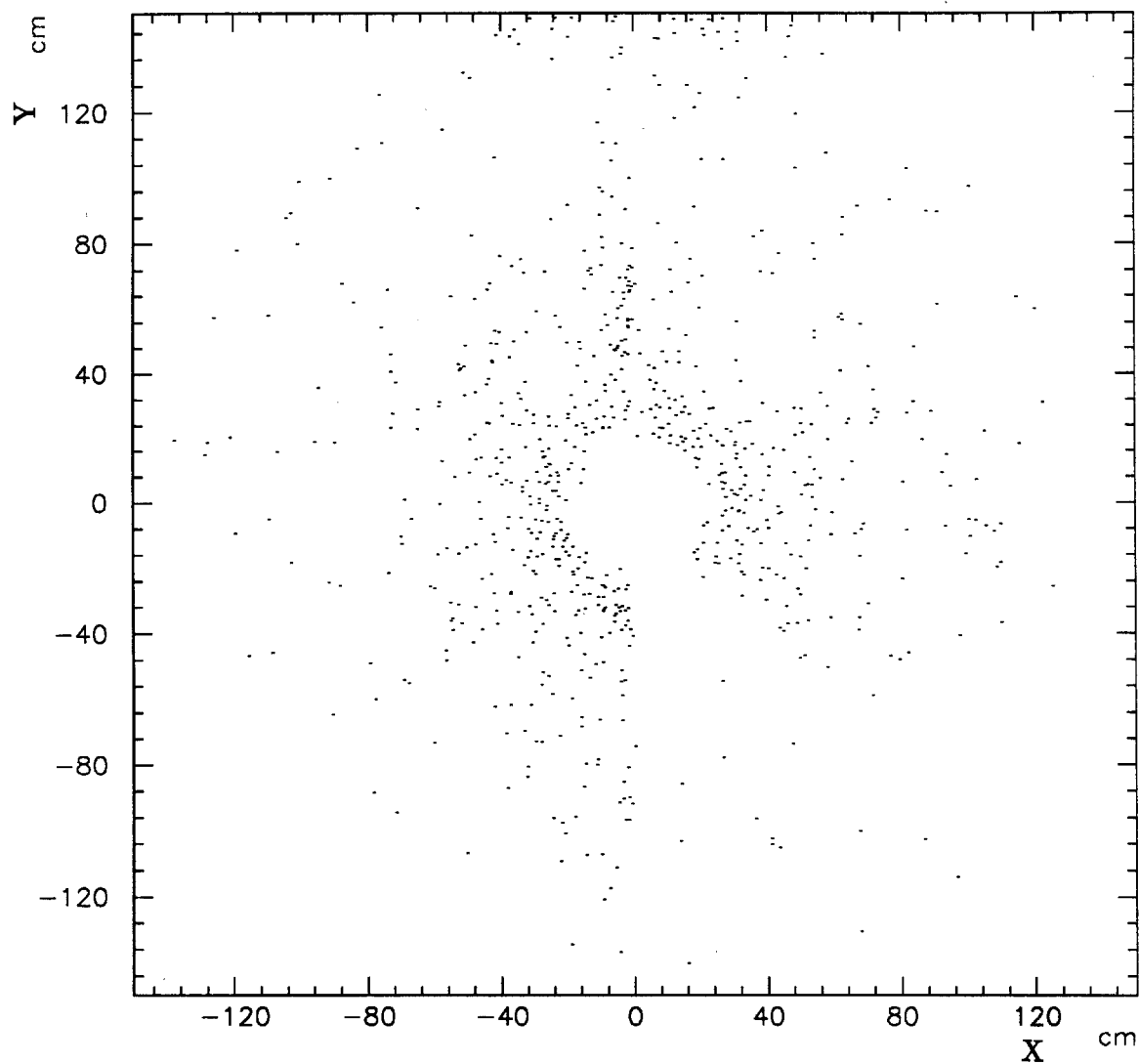


Figure 5.2 Spatial distribution of photons for events when the veto wall had no hit in the quadrant corresponding to the trigger quadrant of the EMLAC.

Associated with each reconstructed photon is a quantity referred to as directionality (δ_r), which is a measure of the photon's trajectory in the EMLAC. It is determined from the energy deposition in front and back of the EMLAC. Directionality is defined as;

$$\delta_r = R_f - \frac{Z_{front}}{Z_{back}} R_b \quad (5.1)$$

where R_f , R_b are the reconstructed front and back radial positions of the energy centroids. The parameters

$$Z_{front} = 900 \text{ cm}$$

and

$$Z_{back} = 918.5 \text{ cm}$$

are the longitudinal positions, relative to the target center, of the beginning of the front and the back sections of the EMLAC. Particles that have trajectories parallel to the beam line will have larger directionality, at all radii, than particles that originate from the target because $R_f \approx R_b$ for parallel trajectories. Figure 5.3 shows the situation when a muon enters the EMLAC parallel to the beam line, and when a photon originates from the target.

The correlation between directionality and hits in the veto wall can be seen in Figs. 5.4 and 5.5. When one of the veto walls has a signal, the particles in the EMLAC tend to have large directionality, and when the veto wall has no signal the directionality is primarily centered on zero. The directionality in Figs. 5.4 and 5.5 is displayed as a function of transverse momentum, showing that for

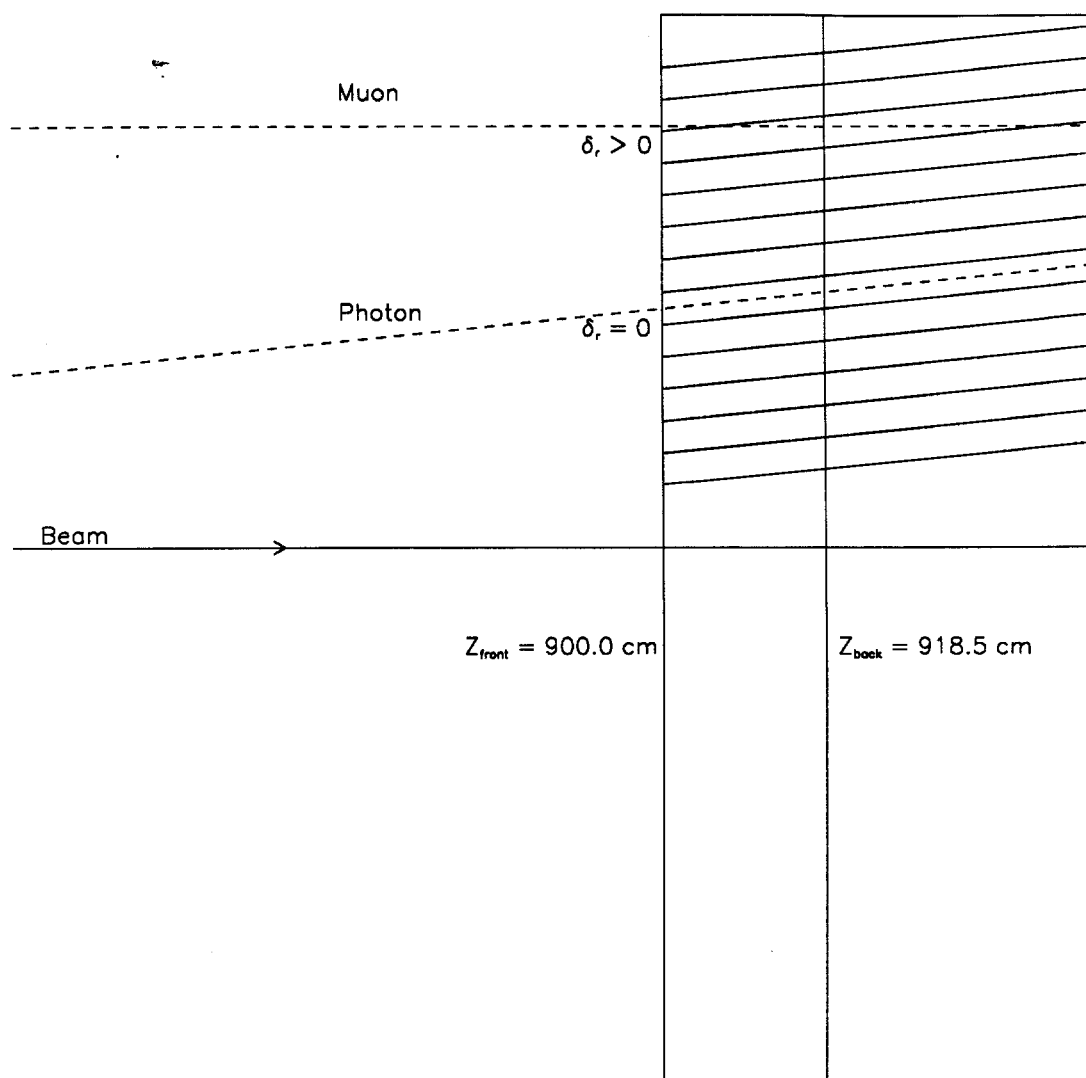


Figure 5.3 Directionality expected for a muon from the halo of the beam and for a photon originating in the target.

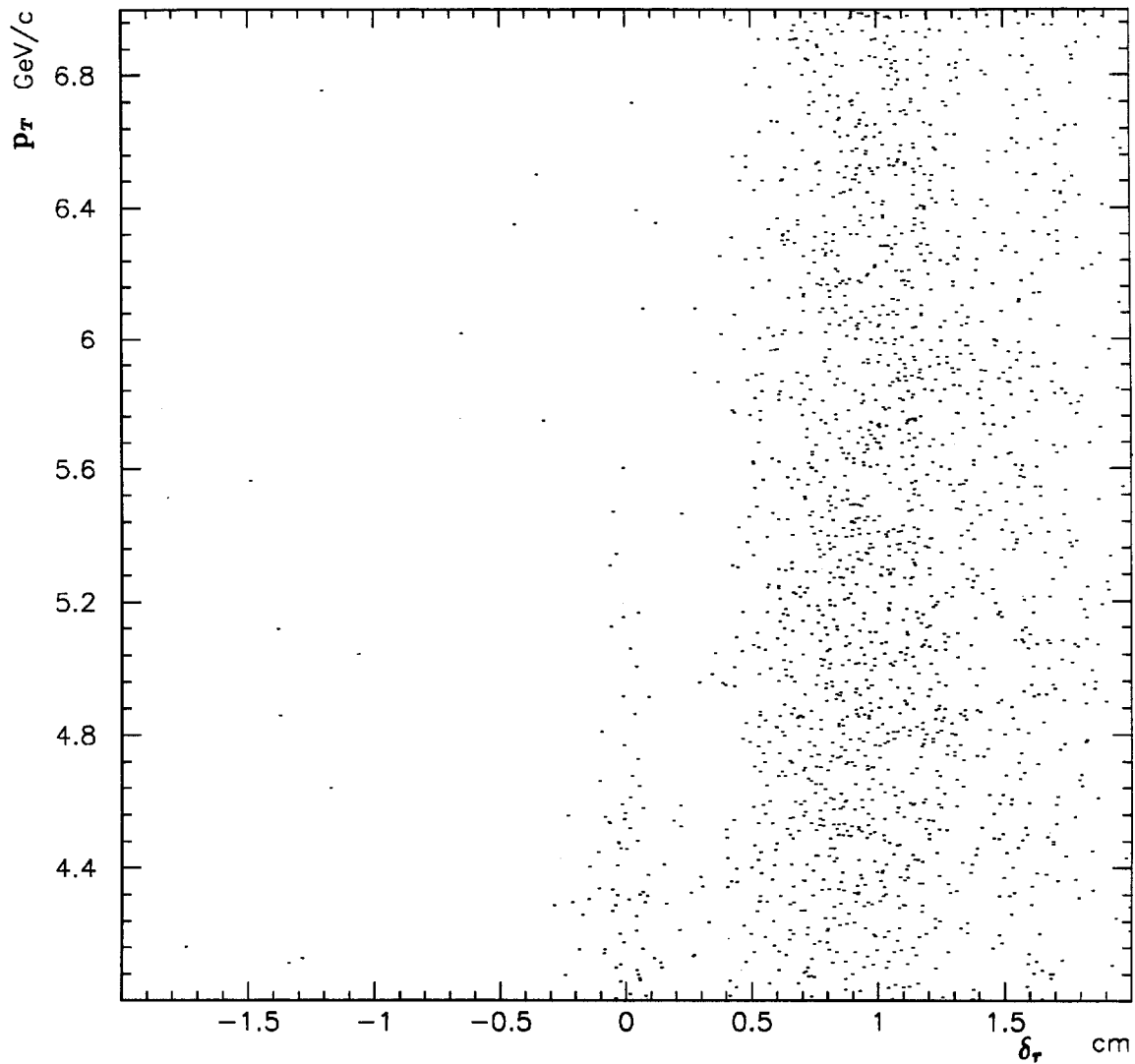


Figure 5.4 p_T dependence of directionality for events when the veto wall had a signal in the quadrant corresponding to the triggering quadrant of the EM-LAC. At large p_T , the majority of photons have large directionalities, indicating that the background for large p_T photons are objects not originating from the target.

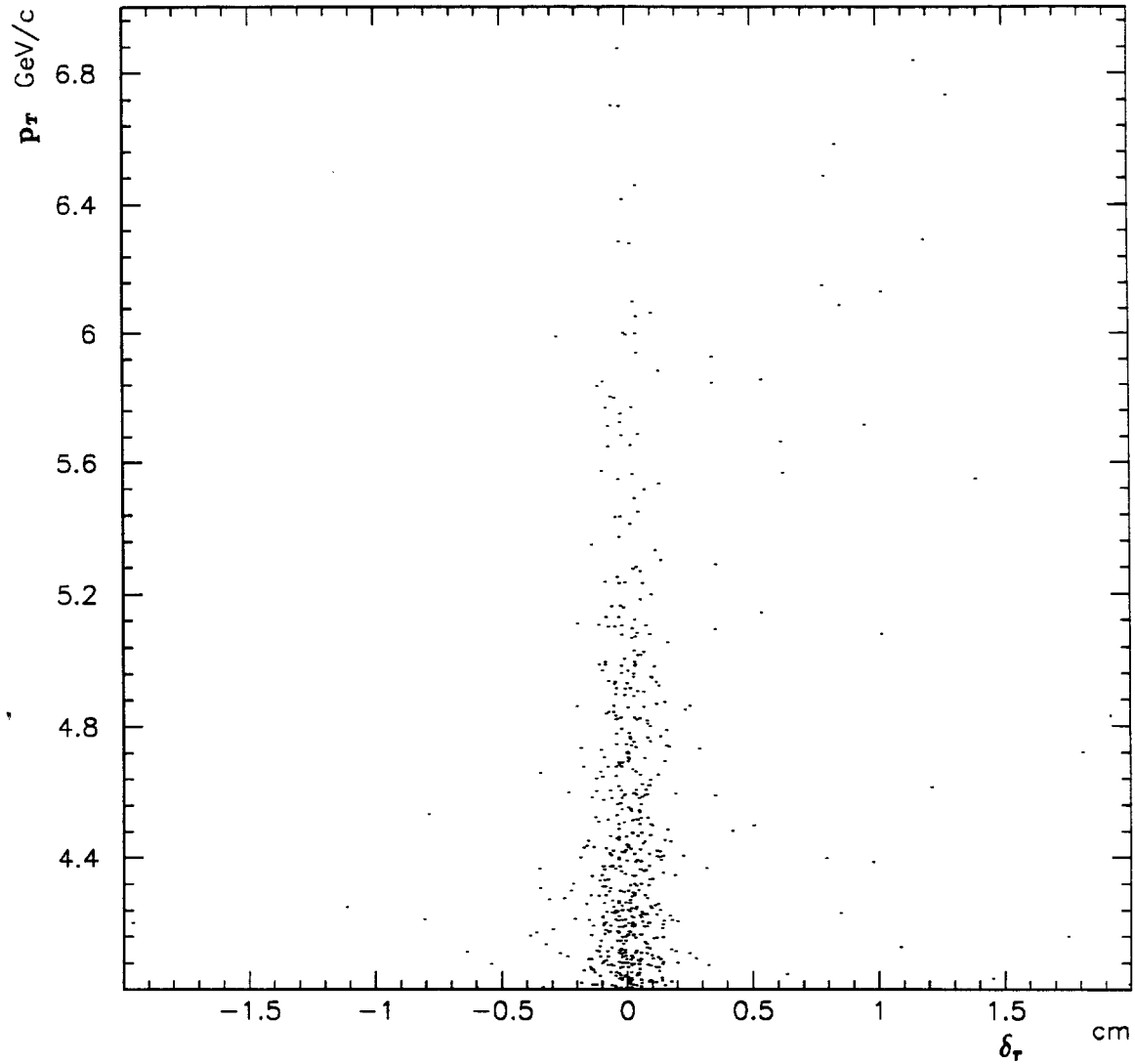


Figure 5.5 p_T dependence of directionality for events when the veto wall had no signal in the quadrant corresponding to the triggering quadrant of the EM-LAC. The background at large p_T seen in Fig. 5.4 is removed by the requirement that the veto wall have no signal as mentioned above.

large p_T the data are dominated by particles that have trajectories parallel to the beam.

Another quantity measured for each reconstructed photon is the energy arrival time calculated using the algorithm described in Chapter 4. Muons in the EMLAC do not have to correlate with interactions in the target. Figures 5.6 and 5.7 show plots of time versus transverse momentum for photons that are not derived from two photon mass pairs in the π^0 or η peaks. Figure 5.6 is for photons with a signal in the veto wall, and Fig. 5.7 is for events without such hits. These plots indicate that when the veto wall has a hit we reconstruct a large number of energy depositions that are out of time with the interactions, namely muons.

Figures 5.8 and 5.9 show the correlation between directionality and reconstructed time when the veto wall has a hit, and when it does not. The figures show that, when the veto wall has a hit, events have large directionality and are out of time, while when there is no hit, the events cluster near small directionality and are in time with the rest of the trigger.

Uncorrelated Energy

Events with large values of uncorrelated energy were studied, and observed to correspond to good events in which the GAMMAS did not properly correlate to form a photon. Figure 5.10 shows a plot of the uncorrelated energy in quadrants which have a large- p_T π^0 . Sometimes, a fluctuation in the tail of a shower can produce a peak that can form a GAMMA. Not surprisingly, these GAMMAS often will not correlate with a GAMMA from another view. The energy of this

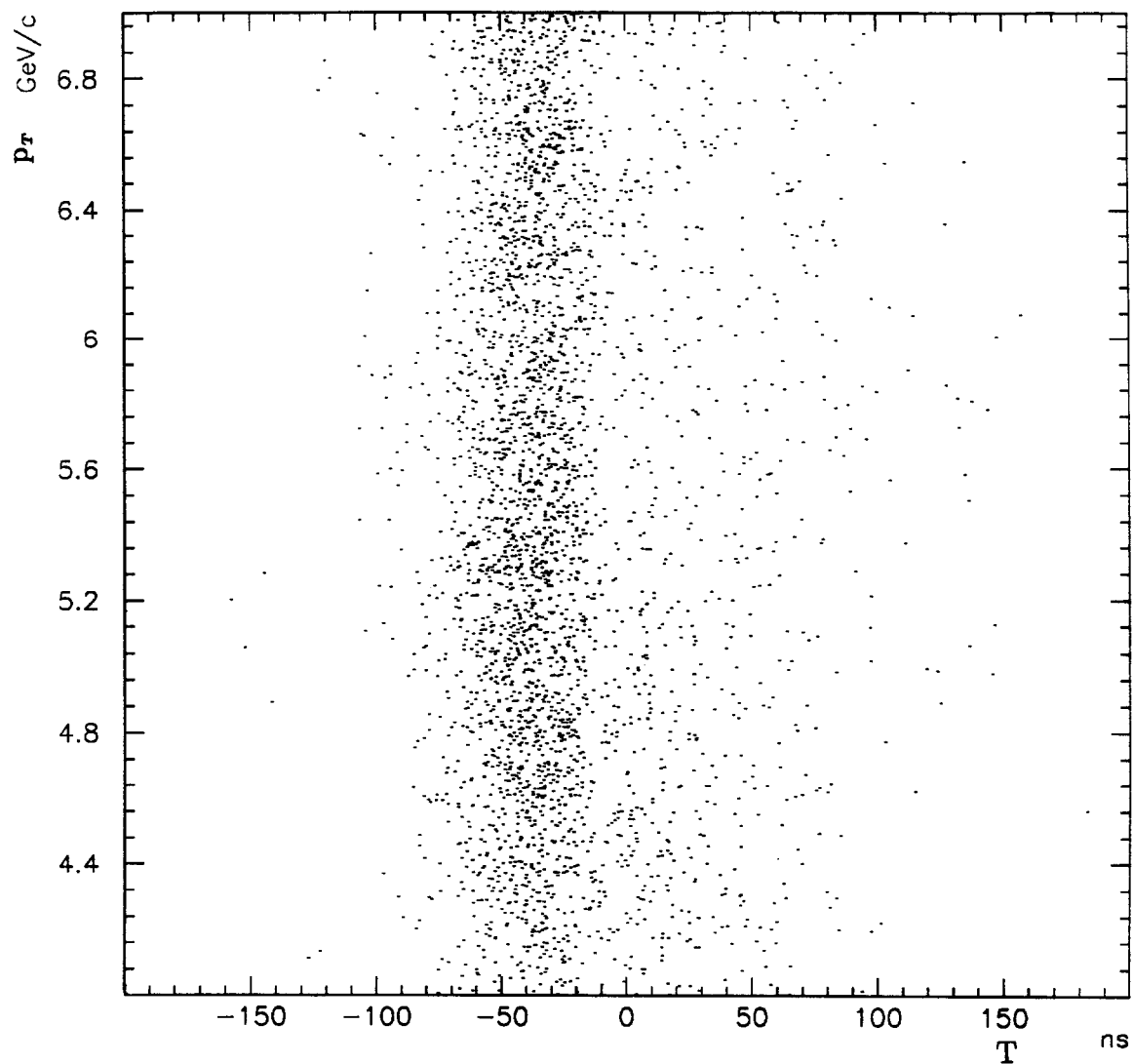


Figure 5.6 p_T dependence for the time of arrival of photons for events when the veto wall had a signal in the quadrant corresponding to the triggering quadrant of the EMLAC. A large number of out of time events can be seen at ~ -45 ns for all p_T .

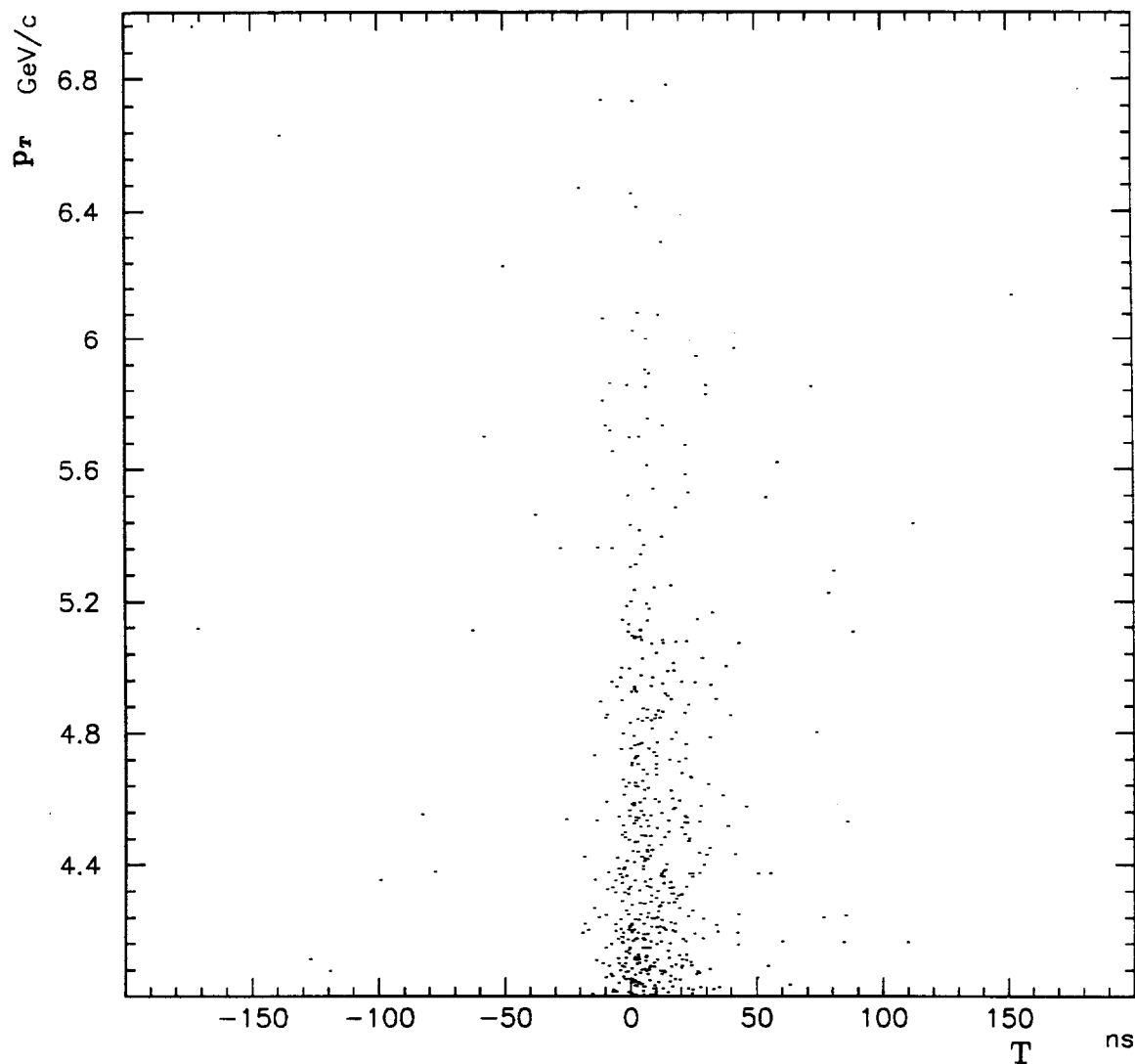


Figure 5.7 p_T dependence for the time of arrival of photons for events when the veto wall had no signal in the quadrant corresponding to the triggering quadrant of the EMLAC. The out of time events seen in Fig. 5.6 have been removed by this veto wall cut, indicating a correlation between out of time events and muons.

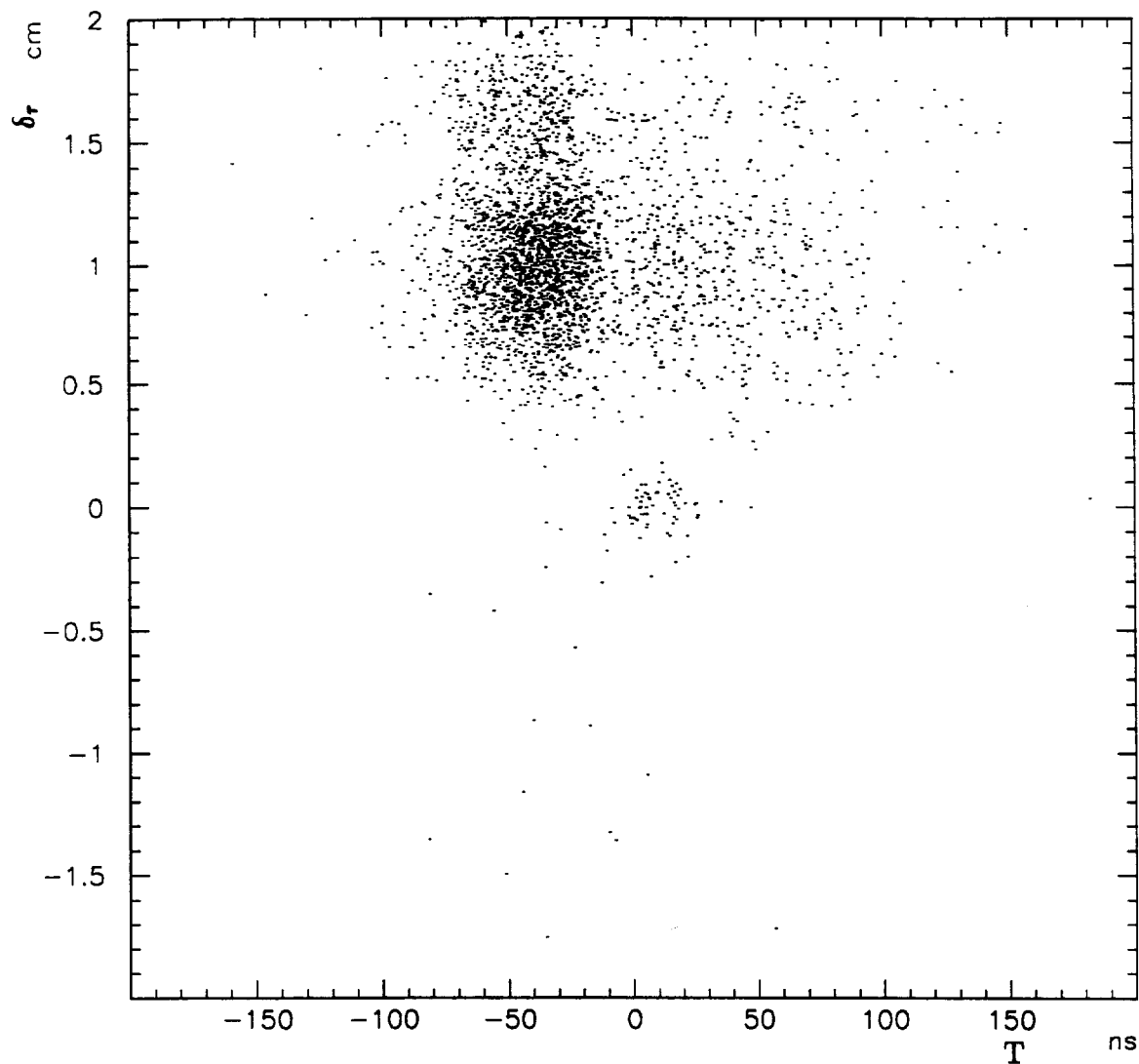


Figure 5.8 Directionality vs photon time of arrival for events when the veto wall had a signal in the quadrant corresponding to the triggering quadrant of the EMLAC. Out of time objects tend to have large directionalities, consistent with the assumption that they are muons from the beam halo.

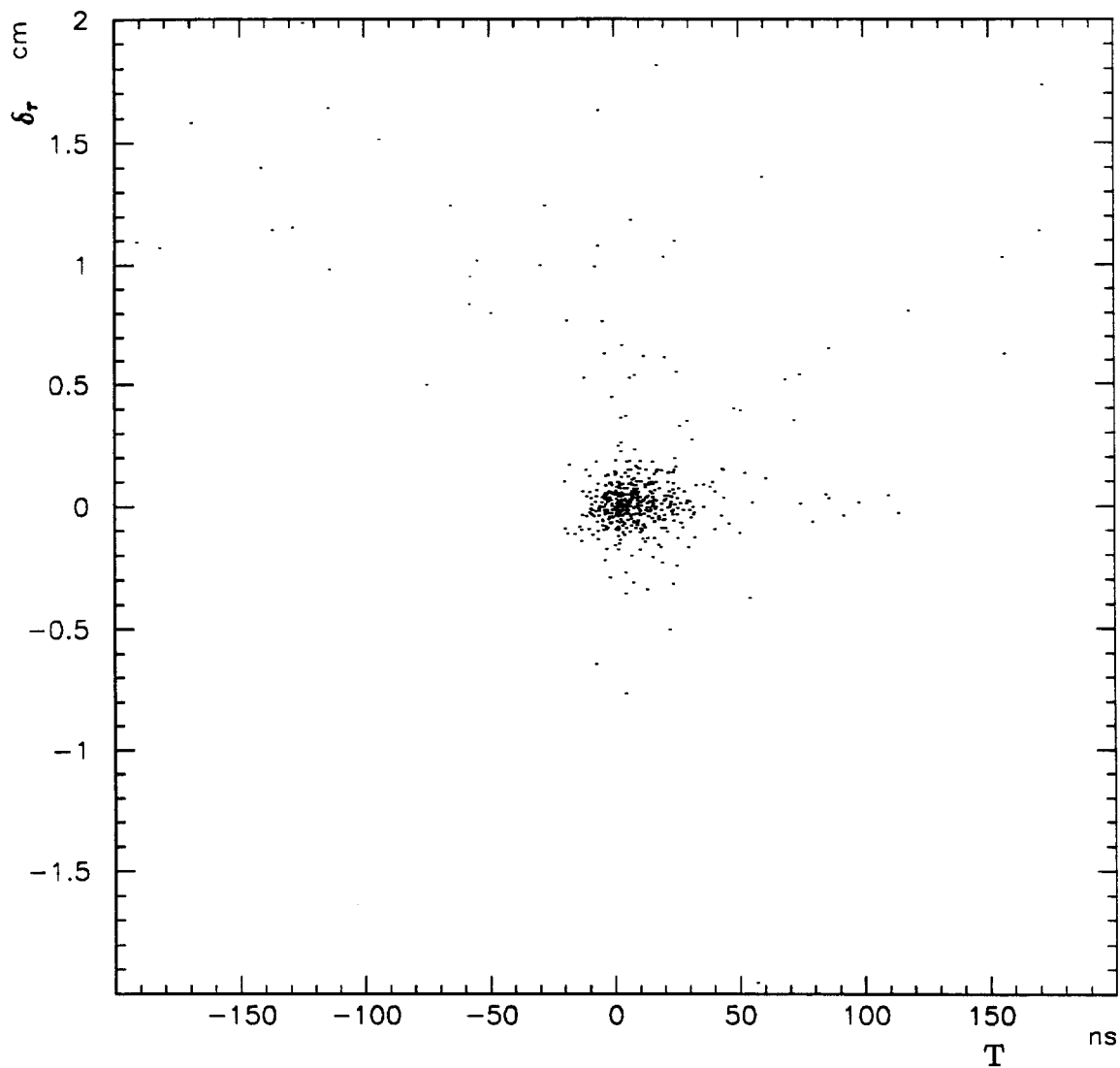


Figure 5.9 Directionality vs photon time of arrival for events when the veto wall had no signal in the quadrant corresponding to the triggering quadrant of the EMLAC. In time objects are seen to originate from the target (small directionality).

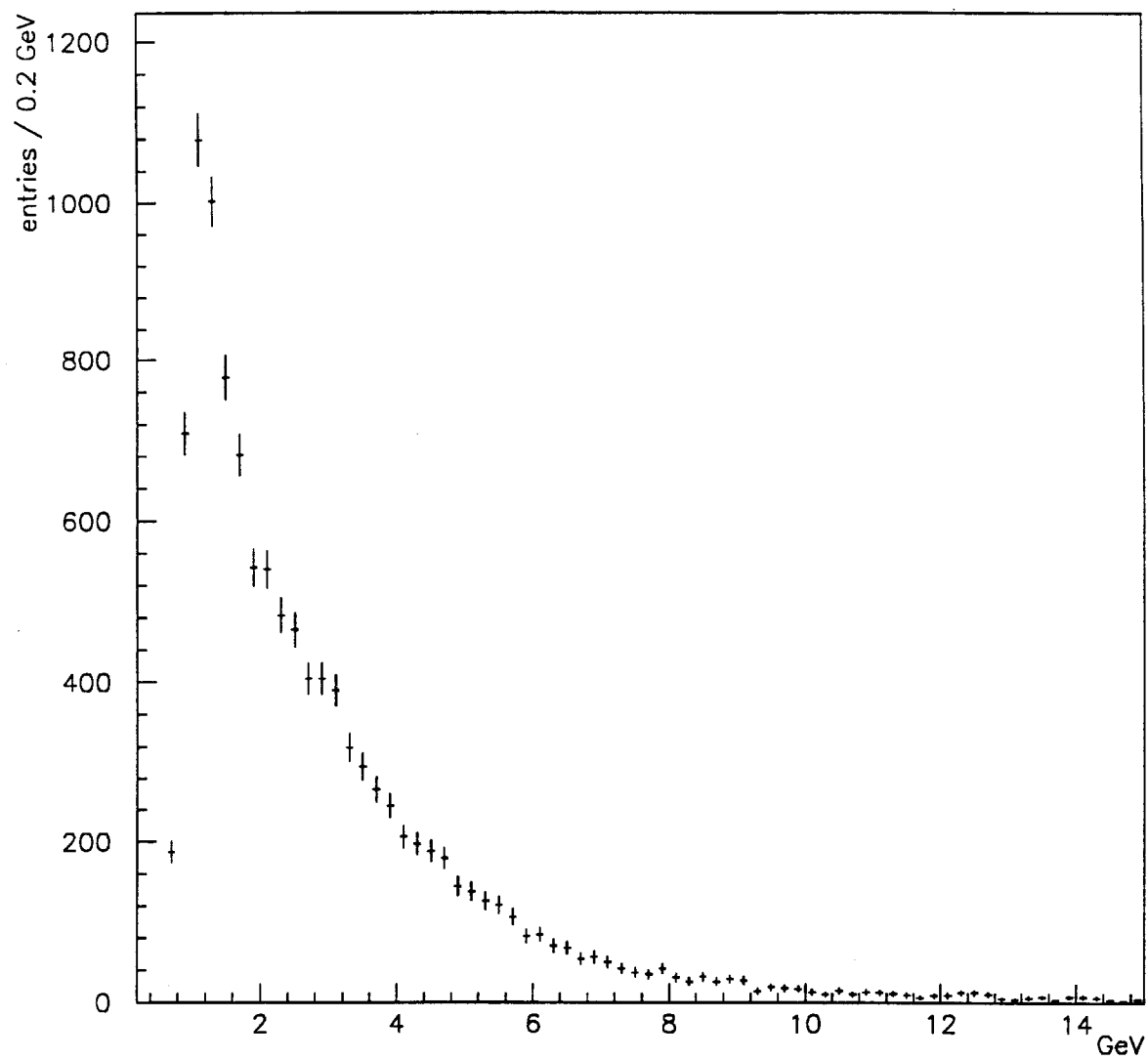


Figure 5.10 Maximum uncorrelated energy per event. Events with zero uncorrelated energy are not plotted.

GAMMA is therefore added to the total uncorrelated energy in that quadrant. Events with large uncorrelated energy are therefore suspect and consequently removed from the data sample. The maximum allowed uncorrelated energy for the π^0 quadrant was 10 GeV.

Vertex Selection

The final requirement in the event selection is that all events have a vertex within the target region. This is needed to provide unambiguous cross sections for beryllium and copper targets. From these cross sections we can extract the atomic mass dependence of π^0 production in π^- and proton interactions. The reconstructed vertex distribution is shown in Fig. 5.11 for events where a π^0 was reconstructed. There are 22 peaks in the distribution; the first 2 correspond to the copper targets, while the remaining 20 correspond to the beryllium targets.

The relative reconstruction efficiency is shown in Fig. 5.12 for events that have a high transverse momentum π^0 . The solid crosses represent the uncorrected number of vertices found in each of the beryllium targets. The following three corrections were applied to produce the distribution shown by the dotted crosses:

- Correction for beam absorption in any upstream targets.
- Correction for photon conversions in targets downstream of any given target.
- An overall efficiency correction based on event by event visual inspection.

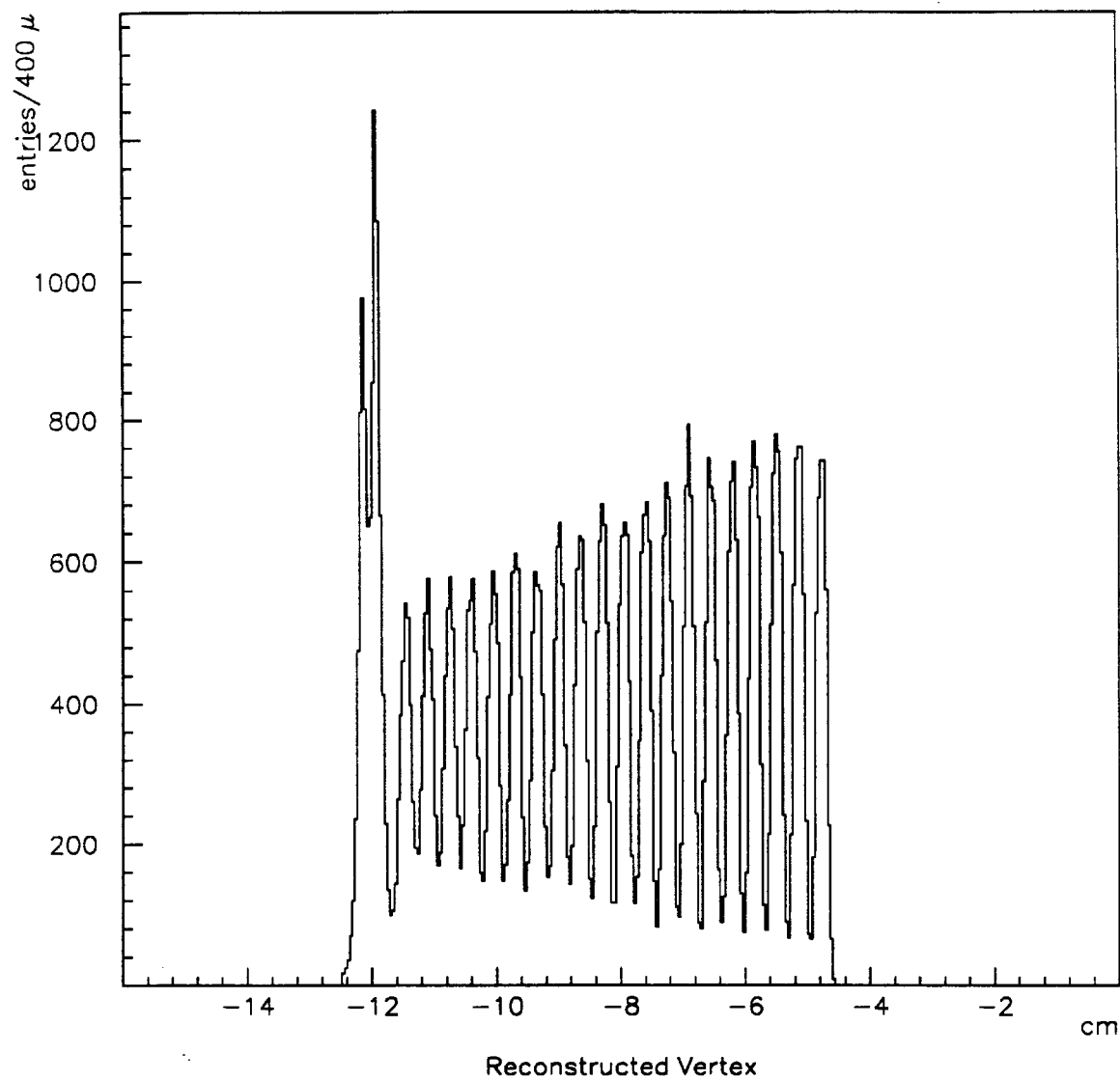


Figure 5.11 Distribution of vertices from high p_T π^0 events. The 20 beryllium targets and 2 copper targets are clearly visible.

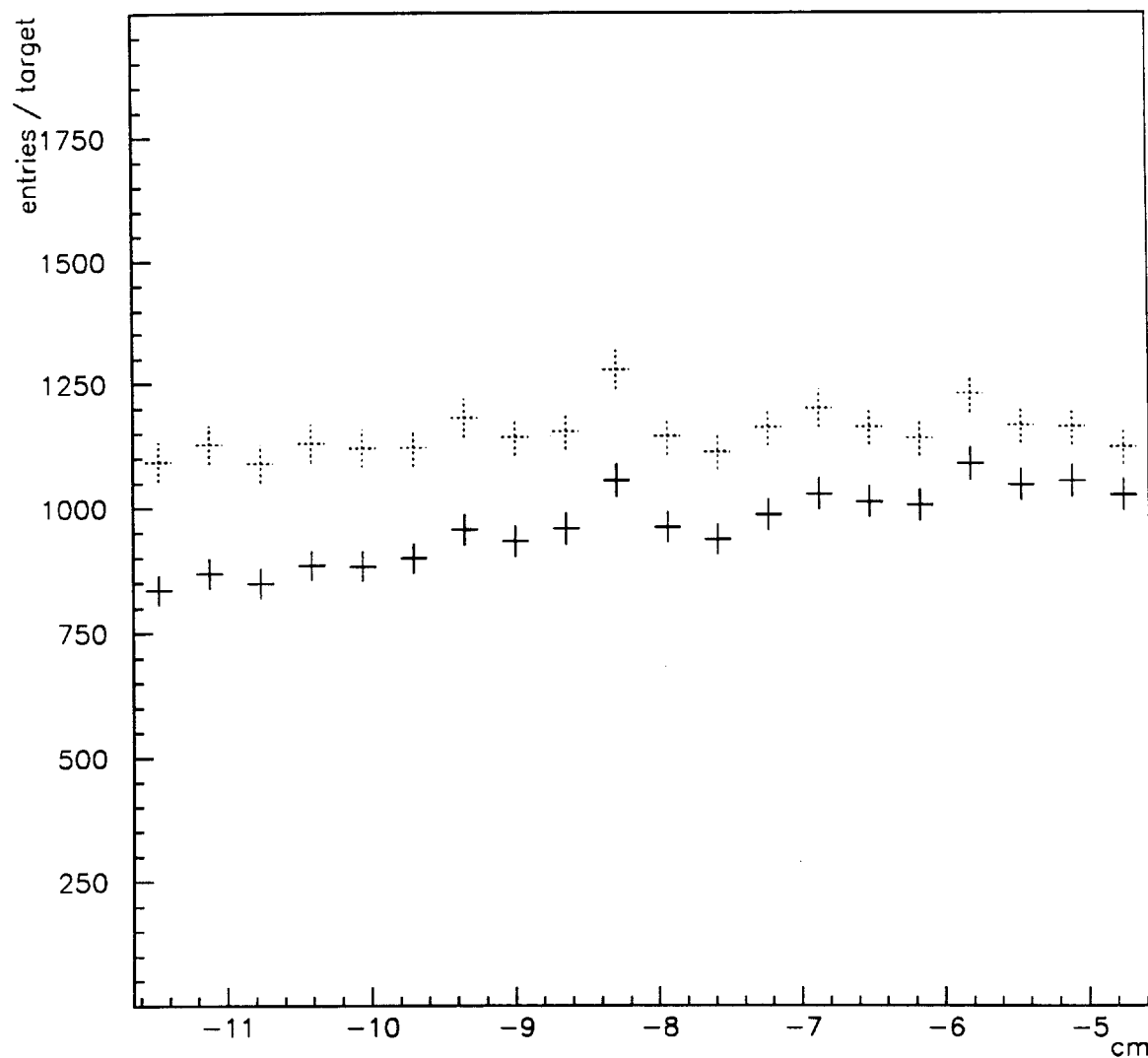


Figure 5.12 Uncorrected number of events, having a high p_T π^0 , per beryllium target. The dotted crosses represent the corrected number of events per target. Corrections being applied were for lost π^0 's due to photon conversions within the target and beam particle absorption within the target.

5.2. TWO- γ MASS DISTRIBUTIONS

π^0 Signal Definition

Figure 5.13 shows the mass distribution for two-photon pairs in the region of the π^0 mass. A π^0 is defined as a $\gamma\gamma$ mass in the range between 110 and 160 MeV. The solid line is the mass distribution for all pairs with $p_T \geq 3.0$ GeV/c, while the dotted line has an energy asymmetry* cut of 0.75. This cut-off was chosen because the asymmetry plots from a Monte Carlo simulation agree with the data up to 0.75. That is, in this range of asymmetry, the π^0 reconstruction efficiency is consistent with the Monte Carlo. Figure 5.14 shows the asymmetry distribution for π^0 s with $p_T \geq 3.5$ GeV/c, and superimposed is a polynomial fit to similar Monte Carlo events. The π^0 signal was defined with a subtraction of the background as estimated from the sidebands 75 - 100 and 170 - 195 MeV; the side bands correspond to the estimated number of background events expected in the peak.

Energy Corrections

Because each octant was read out and triggered using separate electronic modules, a check was made on the relative energy scale between octants. The peak in the π^0 mass was calculated for each octant and a correction factor determined to bring that mass into agreement with the accepted value of 135 MeV. The rescaling of the energy of each photon thereby improved the overall resolution in subsequent analysis. The correction factors used in the analysis were

* The energy asymmetry A is defined as $\frac{|E_1 - E_2|}{E_1 + E_2}$ where E_1 and E_2 are the energies of the two photons. It corresponds to $|\cos\theta|$ of the γ with respect to the π^0 line of sight, as calculated in the rest frame of the π^0 . For a spin zero object, such as the π^0 , the distribution should be isotropic. Biases in π^0 acceptance and reconstruction can produce departures from isotropy.

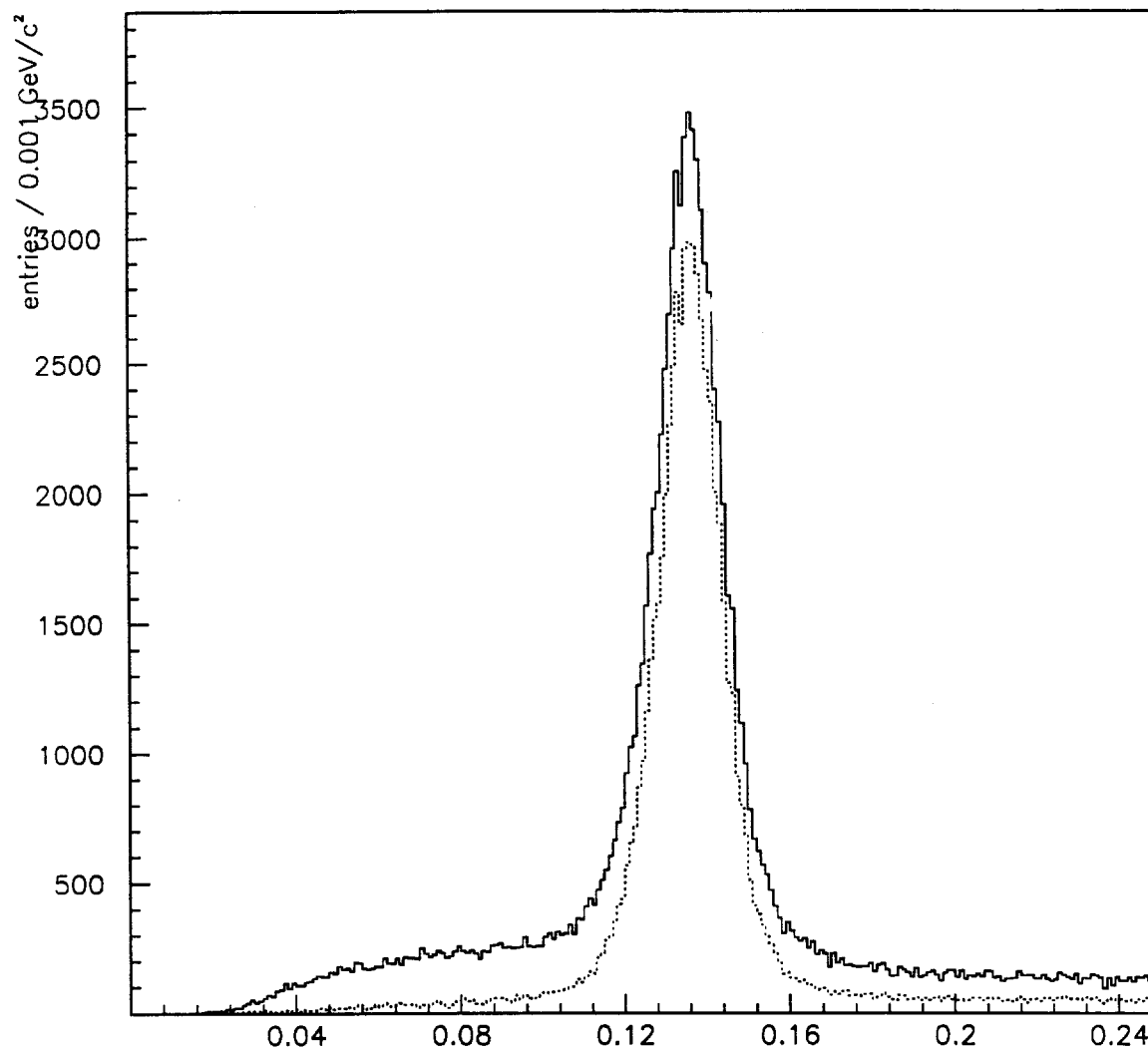


Figure 5.13 Two photon mass distribution near the π^0 mass for $p_T \geq 3.0 \text{ GeV}/c$. The dotted line represents the two photon mass distribution with an energy asymmetry cut of 0.75.

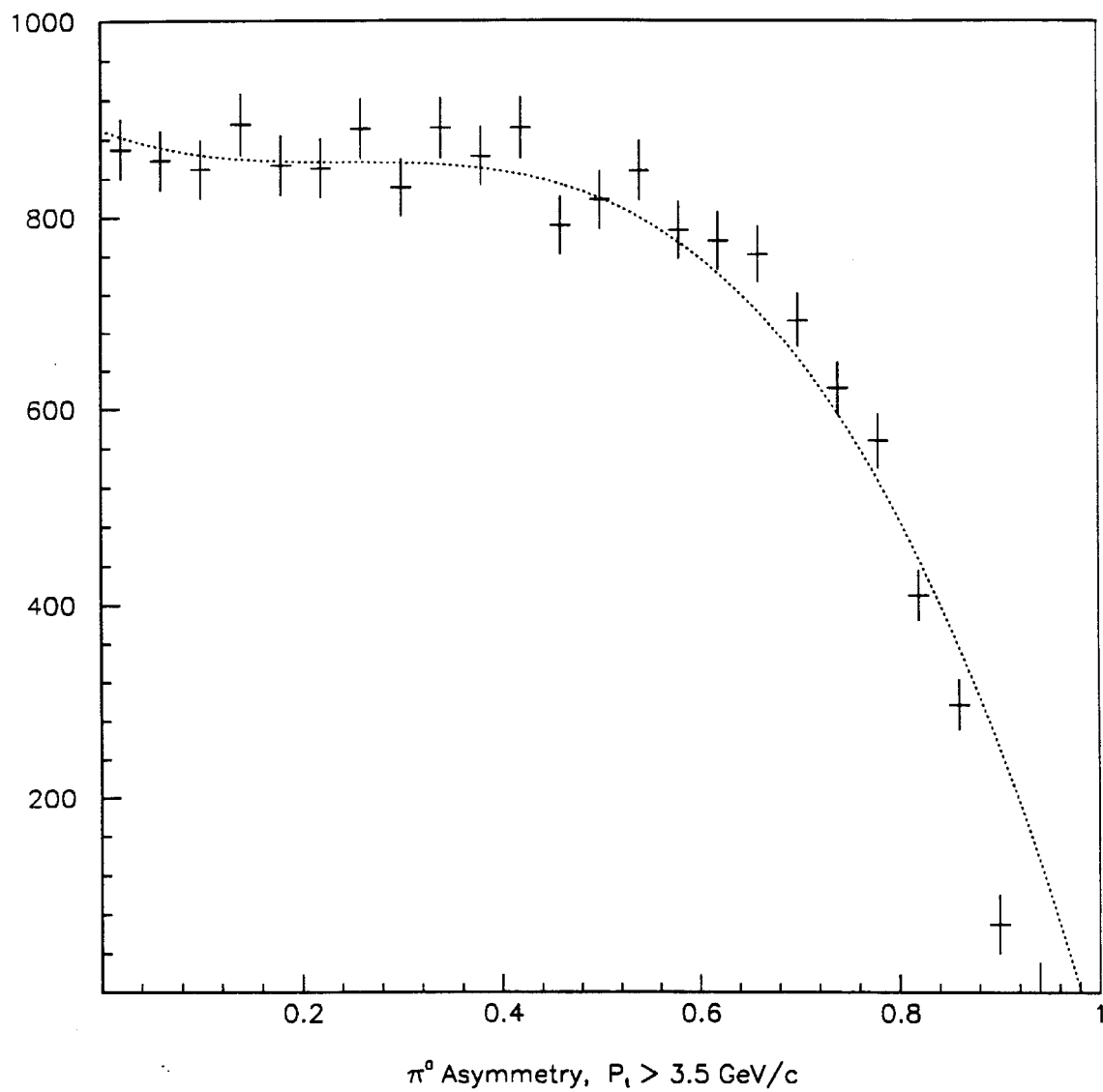


Figure 5.14 π^0 asymmetry distribution. The dotted line represents the asymmetry distribution for Monte Carlo generated π^0 s .

0.9655, 0.9648, 1.0014, 0.9846, 0.9372, 0.9444, 0.9683, and 0.9392 for octants one through eight, respectively. Figure 5.15 shows the corrected values of the π^0 mass as a function of octant number, for $p_T \geq 4.0$ GeV/c.

Figure 5.16 shows the number of π^0 's found per octant with p_T greater than 4.0 GeV/c; the yield was corrected for trigger differences, and divided by the live triggerable beam for that octant. Since all octants were not in the trigger for all runs, the live-beam count can vary from octant to octant. Octant eight is low compared to the rest of the octants due to losses in a region of the LAC that was not triggering properly. Octant five is low because the trigger for this octant was not as efficient as that for the other octants below a p_T of 5.0 GeV/c. Octants one and seven have larger error bars because they were not in the trigger for the same number of runs as the other octants.

An additional energy correction had to be applied for photons that showered near the inner/outer Φ boundary; this had to do with losses of energy in Φ views. Photons near this boundary usually deposit energy in both inner and outer radial sections; however, if the energy in one of the Φ views is not large enough to reconstruct a GAMMA, the GAMMAS in the radial sections would not correlate to form a photon and the energy in the Φ views will therefore be lost. A correction for this effect was obtained by generating Monte Carlo photons near the boundary, and then correcting for any lost energy as a function of distance from the boundary.

Dependence of the π^0 mass on radial position

The dependence of the π^0 mass on radial distance from the center of the LAC is shown in Fig. 5.17. The drop in the value of the reconstructed mass at a

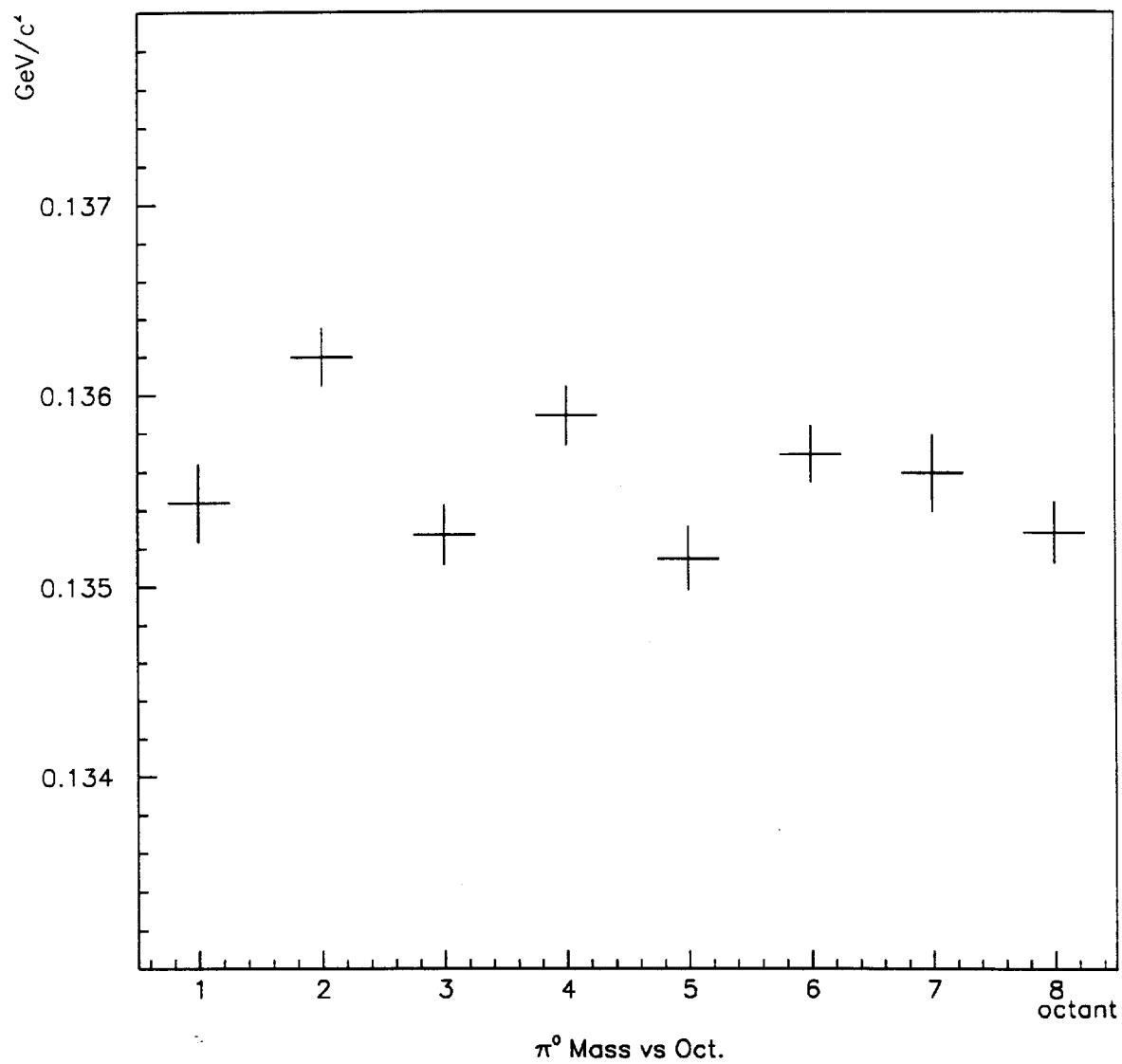


Figure 5.15 Reconstructed π^0 mass per octant.

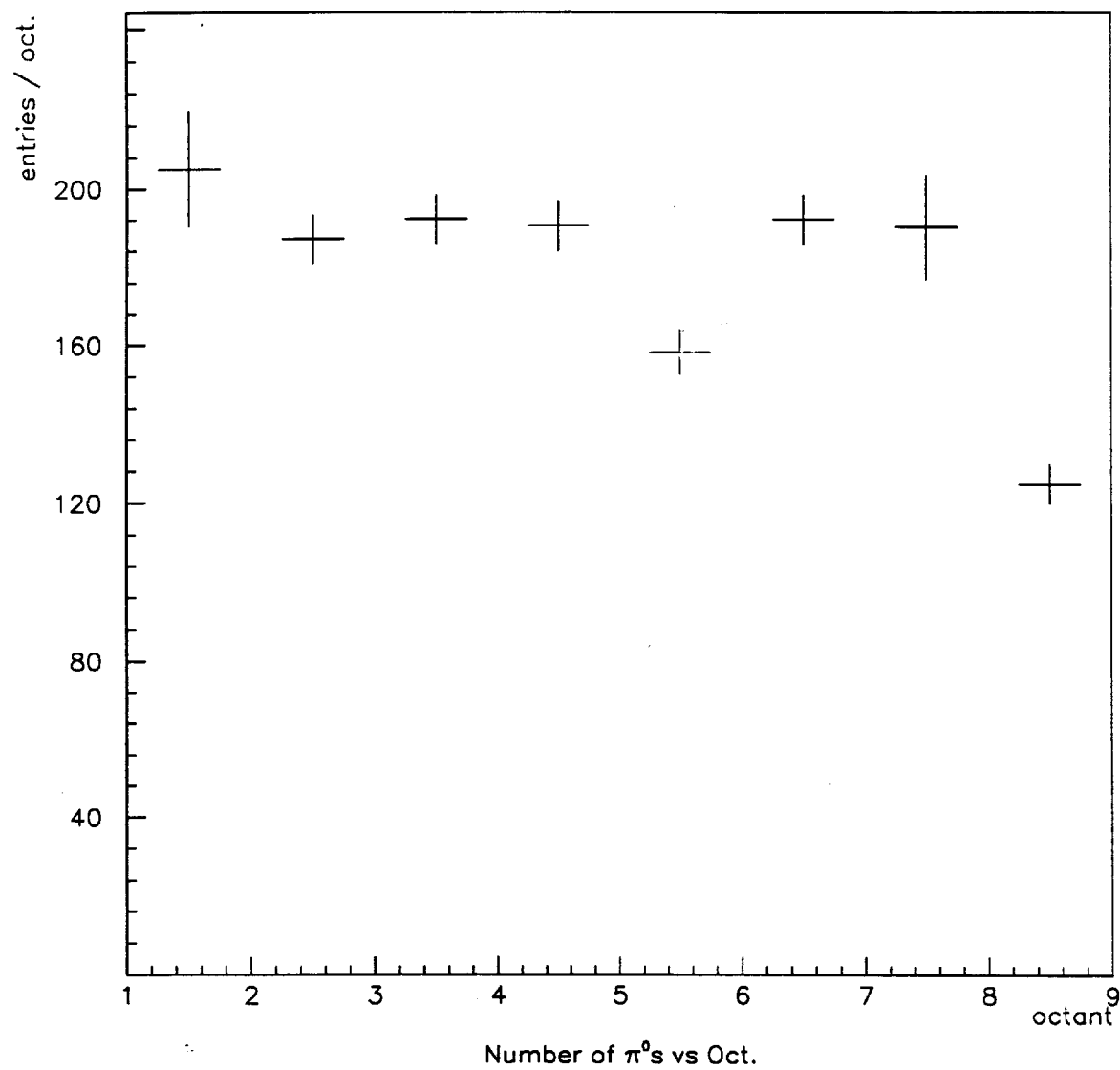


Figure 5.16 Corrected number of reconstructed π^0 s per octant. Corrections applied are for live beam and trigger efficiency.

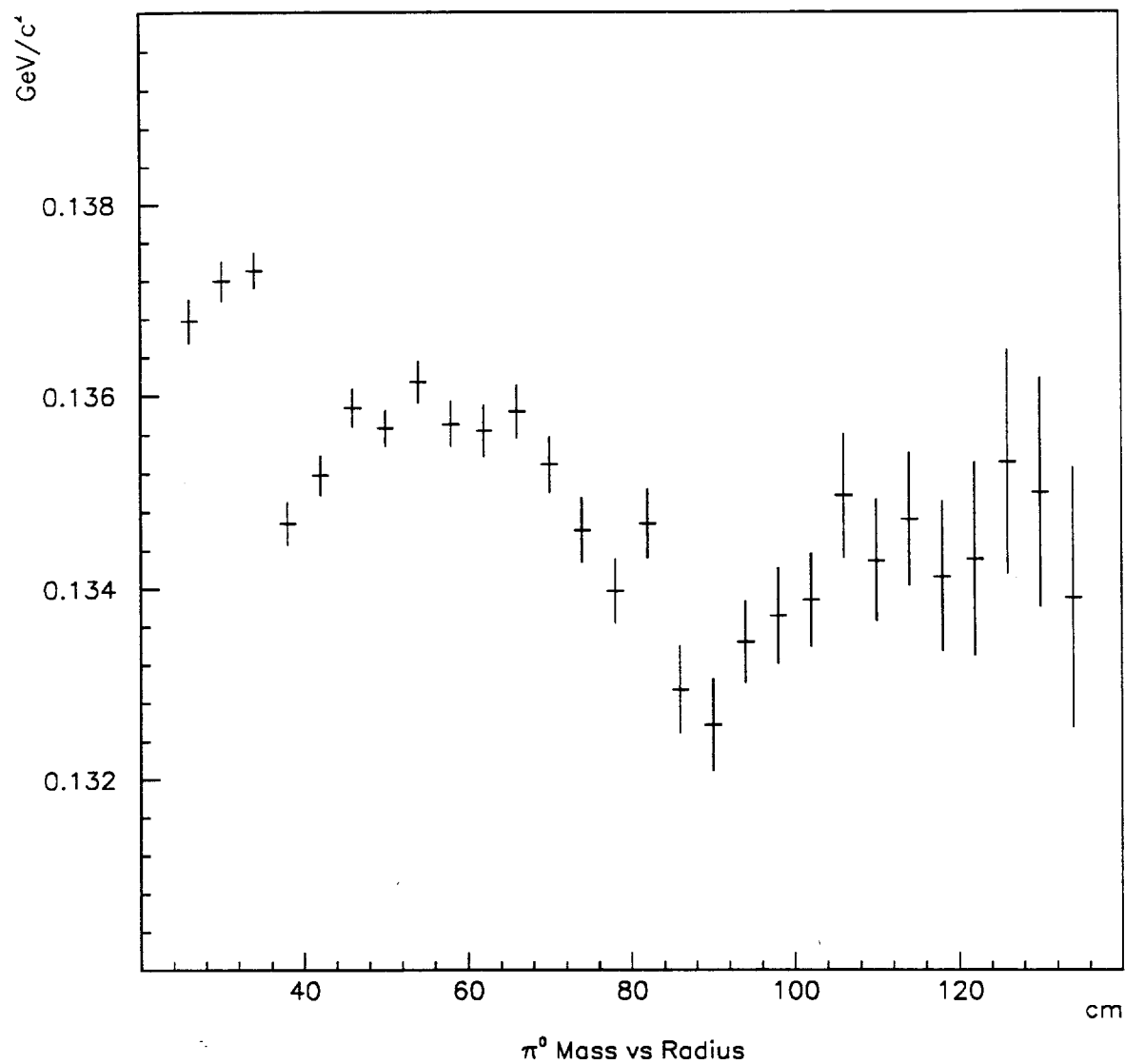


Figure 5.17 Reconstructed π^0 mass as a function of radius. The drop at ~ 40 cm is due to reconstruction inefficiency at the inner/outer Φ boundary. The drop at ~ 90 cm is not yet understood.

radius of ~ 40 cm is due to incorrect reconstruction of photons at the inner/outer radial boundary. The correction at the boundary was clearly not fine enough to account for such small differences, and the π^0 mass was therefore rescaled to 0.135 MeV for radial region between 32 cm and 48 cm. The small drop in the π^0 mass near 90 cm is not fully understood, but was treated in the same fashion, namely by rescaling the energies of the photons.

Azimuthal dependence of the reconstructed π^0 mass

The π^0 mass and the number of π^0 s observed as a function of ϕ , within a quadrant, are shown in Figs. 5.18 and 5.19, respectively. Data from all quadrants, for $p_T \geq 4.0$ GeV/c, have been added together in order to improve statistics. Figure 5.18 shows a clear drop in the mass value near the octant and quadrant boundaries. This is again due to loss of photon energy in the views where the energy is split and, falling below threshold, improperly correlated. The distribution in the number of π^0 s also indicates a loss at the octant boundary due to energy loss and the resultant trigger inefficiencies. Because the single local trigger is sensitive only to energy deposition within a single octant, a π^0 near the octant boundary, decaying into two photons that fall into separate octants, will have a smaller probability of triggering the event than the case when both photons fall within the same octant. To help alleviate this problem, a requirement was made that a π^0 must have both photons within the same octant, and that the photon shower centroids be at least 2.0 cm from the octant boundary (as well as from the quadrant boundary).

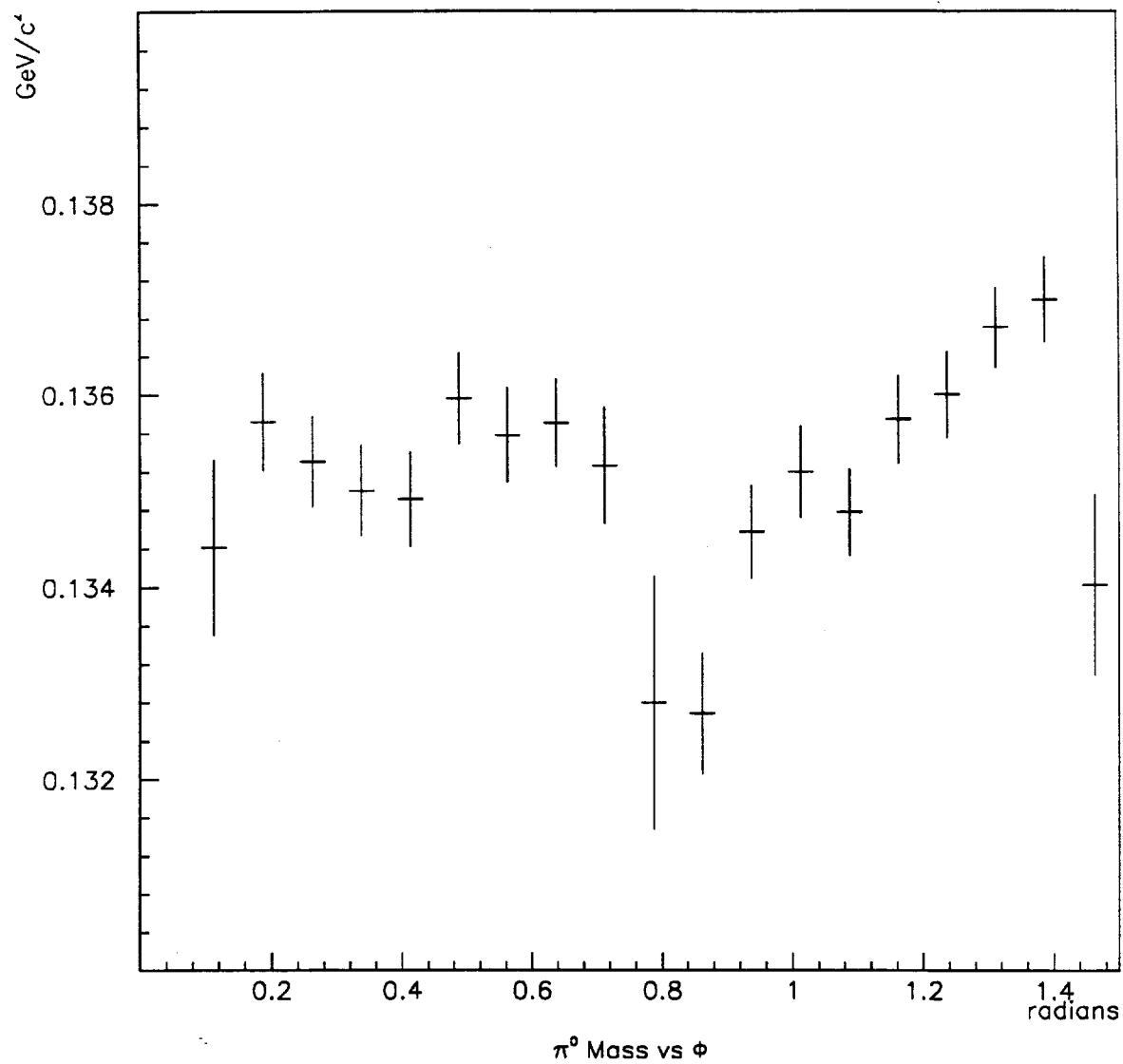


Figure 5.18 Reconstructed π^0 mass as a function of azimuth angle, projected to quadrant one. The drop at $\sim \frac{\pi}{4}$ is due to energy loss into the neighboring octant.

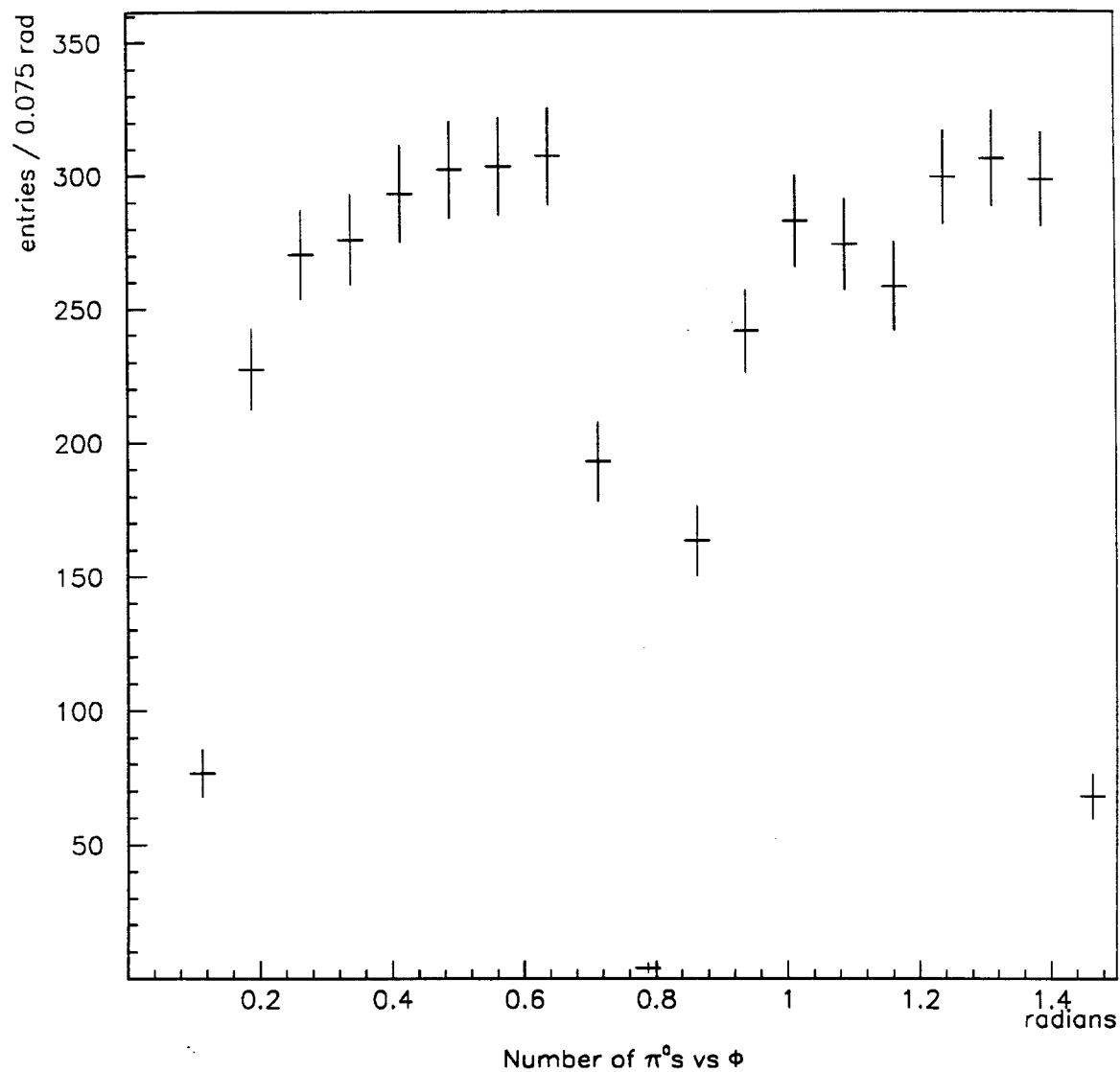


Figure 5.19 Number distribution of reconstructed π^0 s as a function of azimuth angle, projected to quadrant one. The drop at $\sim \frac{\pi}{4}$ is due to trigger losses at octant boundaries.

5.3 ACCEPTANCE AND RECONSTRUCTION EFFICIENCY

Acceptance and reconstruction efficiency was calculated using a Monte Carlo simulation of the LAC. One thousand π^0 's were generated in each p_T and rapidity bin and reconstructed with the same offline reconstruction code as used for data. The p_T ranged from 3.0 to 10.0 GeV/c, with bin widths of 0.5 GeV/c, while the rapidity varied from -1.0 to 1.0 in 0.2 intervals. The acceptance was evaluated as the number of times a π^0 , of given p_T and rapidity, would decay into two photons that would fall in the fiducial region of the EMLAC, divided by the number of events generated in that p_T and rapidity bin. The reconstruction efficiency was calculated with the added requirement that the two photons meet the π^0 definition given in Section 5.4. Tables 5.3 and 5.4 list the acceptance and reconstruction efficiencies used in the analysis.

5.4 TRIGGER CORRECTIONS

At present, the most studied trigger in E706 is the single local; we shall therefore consider only those events for which this trigger fired. There are 14 groups of 16 radial strips per octant for the single local trigger. Because the number of events available for analysis was limited, the trigger efficiency was calculated for three regions of each octant; the first region contained the first two trigger groups, the second region contained the next four groups, and the third region the remaining eight. For the range where the single local trigger was turning on the two gamma trigger was 100% efficient. The efficiency, for each region, was therefore obtained by plotting the ratio $TG \bullet SL / TG$ for the group

p_T

	3.0	3.5	4.0	4.5	5.0	5.5	6.0	6.5	7.0	7.5	8.0	8.5	9.0	9.5	10.0
-1.0	0.805	0.814	0.820	0.830	0.833	0.837	0.838	0.846	0.844	0.846	0.859	0.857	0.859	0.864	0.861
-0.8	0.805	0.814	0.820	0.830	0.833	0.837	0.838	0.846	0.844	0.846	0.859	0.857	0.859	0.864	0.861
-0.6	0.780	0.802	0.809	0.815	0.818	0.825	0.830	0.830	0.828	0.838	0.846	0.843	0.847	0.849	0.8436
-0.4	0.770	0.790	0.805	0.801	0.811	0.810	0.814	0.820	0.822	0.831	0.826	0.827	0.832	0.840	0.834
-0.2	0.751	0.766	0.782	0.788	0.791	0.790	0.784	0.804	0.808	0.801	0.811	0.807	0.8142	0.813	0.821
0.0	0.731	0.752	0.756	0.768	0.771	0.777	0.777	0.783	0.795	0.783	0.792	0.786	0.792	0.796	0.795
0.2	0.717	0.723	0.727	0.738	0.749	0.745	0.754	0.749	0.757	0.765	0.759	0.762	0.763	0.766	0.768
0.4	0.680	0.693	0.690	0.703	0.717	0.719	0.724	0.718	0.724	0.732	0.727	0.731	0.737	0.736	0.734
0.6	0.634	0.654	0.650	0.665	0.673	0.684	0.680	0.686	0.687	0.684	0.688	0.693	0.696	0.701	0.699
0.8	0.599	0.621	0.637	0.642	0.644	0.652	0.650	0.648	0.664	0.658	0.665	0.671	0.671	0.670	0.681

Y

Table 5.3 Absolute π^0 acceptance as a function of p_T and rapidity.

p_T

	3.0	3.5	4.0	4.5	5.0	5.5	6.0	6.5	7.0	7.5	8.0	8.5	9.0	9.5	10.0
-1.0	0.844	0.911	0.939	0.959	0.99	0.99	0.994	0.989	0.992	0.989	0.998	0.982	0.986	0.981	0.977
-0.8	0.894	0.935	0.960	0.974	0.986	0.992	0.991	0.993	0.995	0.993	0.998	0.982	0.986	0.981	0.977
-0.6	0.945	0.959	0.981	0.988	0.983	0.993	0.998	0.997	0.998	0.997	0.998	0.968	0.993	0.986	0.979
-0.4	0.967	0.993	0.984	0.989	0.997	0.993	0.994	0.998	0.998	0.995	0.998	0.978	0.973	0.974	0.974
-0.2	0.984	0.994	0.998	0.996	1.0	0.998	0.994	1.0	1.0	0.998	0.993	0.989	0.979	0.982	0.985
0.0	0.990	0.996	0.996	1.0	0.996	1.0	0.998	0.996	0.994	0.998	1.0	0.978	0.983	0.976	0.970
0.2	0.990	0.986	0.991	0.993	0.996	0.996	0.986	1.0	0.996	0.991	0.998	0.970	0.962	0.960	0.958
0.4	0.998	0.996	0.985	0.989	0.991	1.0	0.996	0.998	0.978	0.959	0.919	0.855	0.675	0.614	0.553
0.6	0.996	0.996	0.986	0.998	0.998	0.996	0.981	0.959	0.936	0.864	0.802	0.591	0.498	0.440	0.381
0.8	0.981	0.983	0.985	0.978	0.970	0.972	0.932	0.884	0.827	0.722	0.606	0.487	0.468	0.364	0.260

Y

Table 5.4 Absolute π^0 reconstruction efficiency as a function of p_T and rapidity,

of sixteen strips which had the highest p_T . The ratio represents the fraction of time the single local fired when the two gamma triggered had already fired.

The trigger corrections were applied by depositing the energies of all photons into the appropriate EMLAC strips. Next, a p_T was calculated for each group of sixteen radial channels by taking the energy in each strip weighted by the radial position of the strip. The group with the largest p_T was assumed to be the one which fired the trigger. The weight given to the event is the inverse of the calculated efficiency at this p_T for the trigger region where the π^0 is located.

To determine cross sections, a minimum p_T value was set for each region of each octant below which no π^0 s were accepted. The p_T cuts were set such that only π^0 s with trigger efficiency $\geq 50\%$ were accepted. Consequently, data from different octants contributed to different ranges of p_T (especially near threshold).

5.5 BEAM PARTICLE IDENTIFICATION

Beam particles were tagged using the Cherenkov counter described in Chapter 2. Extensive studies of the beam composition can be found in the PhD dissertation by A. Lanaro (Ref. 18).

5.6 LIVE BEAM COUNT

The live beam count is calculated using scaler information generated during the spill. A spill event is a pseudo event containing such information. A complete description of the scalers is given in Chapter 5 of the PhD dissertation of C. Lirakis (Ref. 19). Here I will only describe the information that is used in calculating live triggerable beam.

Live triggerable beam is a measure of how many incident beam particles can provide an acceptable interaction. To measure such a quantity, the following items must be taken into account:

- Clean interaction: This is the requirement that the interaction have no other interaction within ± 60 ns. This will contribute dead time since the trigger must reset if a second interaction occurs within the specified time.
- Loss of clean interaction signal in its transmission to the LAC Faraday room (a distance of ~ 50 ft).
- Pretrigger dead time: This is the time required for determining whether the pretrigger condition is satisfied.
- Veto dead time: Time lost due to a veto generated in the muon veto walls, electronic noise (SCRKILL), or by early deposition of p_T (residual energy from a previous event).
- Lost spill event correction: This small correction was required by in the RUN CONTROL program that allowed a run to be ended in the middle of a spill, thereby preventing the scalers in the final spill event from being written to tape.

The product of the above corrections yields the live triggerable beam (LTB) for a given run.

5.7 NORMALIZATION OF THE CROSS SECTION

The invariant cross section per nucleon is given by the expression:

$$\frac{1}{A} E \frac{d\sigma}{d^3p} = \frac{1}{\rho l N_a} C \frac{N^{corr}(p_T)}{B(p_T)} (ABS) \quad (5.2)$$

where

$$ABS = e^{\frac{x}{\lambda}} \approx 1 + \frac{x}{\lambda}$$

is the correction due to beam attenuation from interactions in the thin target, and

$$N^{corr} = \frac{N^{obs}}{2 \pi p_T \Delta p_T \Delta y} \frac{(trig)(conv)(vrteff)}{(accept)(rec)}$$

is the corrected differential p_T distribution. The meanings of the variables in the above expressions are:

- A : Nucleon number of the target material.
- ρ : The density of the target in gm/cm^3 .
- l : The thickness of the target in cm.
- N_a : Avogadro's's number.
- C : An overall normalization factor to be described below.
- $B(p_T)$: The beam count valid for each p_T bin.
- x : The average distance traveled in the target (taken to be l).
- λ : Beam attenuation coefficient.
- Δp_T : Bin width in p_T .

- Δy : Rapidity range.
- *trig* : Trigger correction given event by event.
- *conv* : Correction for lost π^0 's due to conversion of one of the decay photons while still in the target region.
- *vrteff* : Residual vertex efficiency correction mentioned in section 5.2.
- *accpt* : Acceptance correction from Table 5.3.
- *rec* : Reconstruction efficiency correction from Table 5.4.

Because data are derived from runs with different trigger thresholds, the LTB will be different for different regions of p_T . This is taken into account in the expression for $B(p_T)$.

Correction	$\pi^- + \text{Be}$	$\pi^- + \text{Cu}$	P + Be	P + Cu
Double occupancy of beam particle	0.98	0.98	0.98	0.98
Asymmetry cut for π^0	1.333	1.333	1.333	1.333
Veto wall and cut on uncorrelated energy	1.176	1.176	1.176	1.176
Conversion of photons originating from π^0 decays downstream of target	1.082	1.082	1.082	1.082
Beam particle attenuation before target	1.01	1.01	1.014	1.014
Particle content beam	1.03	1.03	1.096	1.096
$C = \text{product of above corrections}$	1.729	1.729	1.847	1.847
λ used in <i>ABS</i>	57.953	19.289	43.283	15.486
<i>ABS</i>	1.043	1.004	1.056	1.005
$\frac{C(ABS)}{l\rho N_a} \times 10^{26}$	40.51	201.08	43.82	215.01

Table 5.5 Corrections to normalization of cross sections.

The factors that are used in calculation of the normalization constant C are listed in Table 5.5 for π^- and p beams on Be and Cu targets. The double occupancy correction scales the beam count for the events where two beam particles are incident on the target. The asymmetry correction comes about because of the cut imposed on the definition of the π^0 . The veto wall and uncorrelated energy correction increases the cross section due to the losses of π^0 s in these cut events. The loss in π^0 signal due to conversion of π^0 photons downstream of the target is taken into account by the fourth factor in the Table 5.5. The beam particle attenuation correction adjusts the cross sections for losses prior to the target. Lastly, the beam count is corrected for misidentification of the beam particle.

6. Results and Conclusions

6.1 CROSS SECTIONS

The inclusive invariant differential cross sections per nucleon, averaged over p_T and rapidity bins for $\pi^- + \text{Be} \rightarrow \pi^0 + \text{anything}$ and $p + \text{Be} \rightarrow \pi^0 + \text{anything}$ are given in Tables 6.1 and 6.2. The ranges for each p_T interval are listed along with the average p_T value measured in that interval. Because of limited statistics, cross sections for the copper target will be presented integrated over rapidity. The data for beryllium were fitted to the phenomenological form:

$$E \frac{d\sigma}{d^3p} = C \frac{(1 - x_D)^n}{p_T^m} \quad (6.1)$$

where

$$x_D = \sqrt{x_T^2 + (x_F - x_0)^2} \quad (6.2)$$

$x_T = 2p_T/\sqrt{s}$ and x_F is the Feynman x in the center of mass ($\sim x_T \sinh(y)$). The experimental cross section was integrated over p_T and rapidity for each interval to obtain the average values used in the fit. Table 6.3 gives the results for the fits for negative and positive beams.

	$C \text{ (mb/GeV}^{-2}\text{/nucleon)}$	n	m	x_0	χ^2_{dof}
$\pi^- + \text{Be}$	24.01 ± 6.42	5.45 ± 0.48	9.60 ± 0.27	0.08 ± 0.01	1.48
$p + \text{Be}$	46.0 ± 4.25	7.21 ± 0.44	9.79 ± 0.05	0.02 ± 0.01	1.37

Table 6.3 Parameters for fits of relation (6.1) to experimental cross sections.

p_T^{min}	p_T^{max}	p_T^{ave}	$-0.7 < Y < -0.5$	$-0.5 < Y < -0.3$
4.0	4.2	4.1	2678.8 ± 358.7	3448.5 ± 367.9
4.2	4.4	4.3	1470.3 ± 166.4	2034.9 ± 213.2
4.4	4.6	4.5	1067.2 ± 146.8	1018.2 ± 123.3
4.6	4.8	4.7	550.1 ± 89.0	866.5 ± 115.4
4.8	5.0	4.9	438.7 ± 67.6	534.1 ± 74.9
5.0	5.4	5.2	294.6 ± 38.3	341.0 ± 39.6
5.4	5.8	5.6	57.6 ± 13.1	96.1 ± 17.5
5.8	6.2	6.0	17.5 ± 6.7	41.2 ± 10.0
6.2	6.6	6.4	11.2 ± 5.1	13.9 ± 6.0
6.6	7.0	6.8	-	2.1 ± 2.1
7.0	8.0	7.2	1.7 ± 1.2	0.6 ± 0.6
8.0	10.0	8.4	0.3 ± 0.3	-

Table 6.1 Invariant cross section in pbarn/GeV² for $\pi^- + \text{Be} \rightarrow \pi^0 + \text{anything}$. Cells with no entries correspond to kinematic regions where either no π^0 s were detected or to regions where the background exceeded the detected number of π^0 s.

$-0.3 < Y < -0.1$	$-0.1 < Y < 0.1$	$0.1 < Y < 0.3$	$0.3 < Y < 0.5$	$0.5 < Y < 0.7$
4828.6 ± 448.3	5461.5 ± 475.9	6112.4 ± 500.0	5957.5 ± 521.9	5891.4 ± 524.6
2757.7 ± 205.2	3534.8 ± 225.9	3539.4 ± 221.3	3111.8 ± 212.9	3400.3 ± 228.4
1617.0 ± 148.8	2039.5 ± 163.1	2362.1 ± 169.1	2074.8 ± 171.5	2085.7 ± 177.5
901.9 ± 89.1	1120.9 ± 107.0	1190.5 ± 104.9	1347.0 ± 110.7	1000.3 ± 105.2
527.6 ± 76.3	759.8 ± 75.4	747.6 ± 73.7	713.9 ± 75.6	659.7 ± 79.0
300.9 ± 31.8	415.4 ± 37.1	436.6 ± 38.4	397.9 ± 37.2	268.8 ± 33.9
138.2 ± 21.9	113.8 ± 19.5	155.1 ± 21.2	134.3 ± 21.3	108.6 ± 19.8
53.4 ± 12.1	51.5 ± 11.2	58.9 ± 12.5	44.2 ± 11.1	60.9 ± 13.7
14.0 ± 5.4	35.7 ± 9.7	7.3 ± 4.2	10.1 ± 6.2	13.7 ± 7.4
7.1 ± 4.3	7.2 ± 4.2	10.6 ± 4.8	1.7 ± 1.7	2.3 ± 2.3
1.0 ± 1.3	5.2 ± 2.1	2.6 ± 1.5	1.7 ± 1.2	2.7 ± 1.6
-	0.4 ± 0.4	0.8 ± 0.5	-	-

Table 6.1 Continued.

p_{π}^{min}	p_{π}^{max}	p_{π}^{ave}	$-0.7 < Y < -0.5$	$-0.5 < Y < -0.3$
4.2	4.4	4.3	1134.8 ± 162.6	2180.9 ± 250.5
4.4	4.6	4.5	1011.8 ± 155.0	1145.0 ± 176.2
4.6	4.8	4.7	721.8 ± 123.1	851.1 ± 136.0
4.8	5.0	4.9	415.5 ± 83.5	401.1 ± 75.1
5.0	5.4	5.2	125.7 ± 26.4	197.2 ± 42.0
5.4	5.8	5.6	58.0 ± 17.5	52.0 ± 17.5
5.8	6.2	6.0	24.3 ± 11.1	10.0 ± 9.7
6.2	6.6	6.4	12.2 ± 7.1	15.3 ± 8.8
6.6	7.0	6.8	-	12.5 ± 7.4
7.0	8.0	7.2	-	1.5 ± 1.5

Table 6.2 Invariant cross section in pbarn/GeV² for p + Be \rightarrow π^0 + anything. Cells with no entries correspond to kinematic regions where either no π^0 's were detected or to regions where the background exceeded the detected number of π^0 's.

$-0.3 < Y < -0.1$	$-0.1 < Y < 0.1$	$0.1 < Y < 0.3$	$0.3 < Y < 0.5$	$0.5 < Y < 0.7$
2748.5 ± 234.4	3311.6 ± 236.0	2767.8 ± 207.8	2833.3 ± 222.4	1878.9 ± 186.8
1327.5 ± 143.2	1620.5 ± 158.0	1591.7 ± 154.0	1325.7 ± 144.5	1349.1 ± 146.7
795.1 ± 111.9	911.3 ± 114.6	1148.1 ± 127.6	767.9 ± 104.8	757.3 ± 106.8
671.4 ± 97.5	512.8 ± 84.0	600.3 ± 88.3	382.7 ± 76.2	178.6 ± 53.3
257.9 ± 41.6	342.1 ± 46.7	169.4 ± 32.7	215.4 ± 36.7	115.9 ± 27.5
116.3 ± 26.4	97.4 ± 23.8	78.1 ± 20.3	109.1 ± 25.1	76.9 ± 23.2
48.3 ± 16.3	41.1 ± 15.8	33.4 ± 12.7	20.5 ± 10.3	5.3 ± 9.7
14.7 ± 8.6	5.6 ± 5.6	24.3 ± 11.0	24.4 ± 10.9	5.8 ± 5.8
-	4.7 ± 4.7	8.2 ± 5.8	-	-
-	-	2.9 ± 2.0	-	-

Table 6.2 Continued.

π^- Beam

The differential cross section for π^0 production from a π^- incident beam as a function of p_T , averaged over seven different rapidity intervals, is shown in Fig. 6.1. The rapidity intervals cover the range from -0.7 to 0.7 in increments of 0.2 units of rapidity. The cross section is restricted to p_T values ranging from $4.0 \text{ GeV}/c$ to $8.0 \text{ GeV}/c$. For clarity, vertical error bars are not shown for the largest p_T values. The lines through each set of points are integrations of the fit over the respective rapidity intervals. As can be seen, there are no significant variations in the shape of the cross sections for the different rapidity intervals. Hence, the dependence on p_T and y can be factorized into the product of the two.

The cross sections as a function of rapidity, averaged over three different p_T intervals, are shown in Fig. 6.2. The solid lines represent the fitted function integrated over the p_T range and plotted versus rapidity. The p_T range for the negative data was restricted to values above $4.0 \text{ GeV}/c$ due to π^0 losses below this value. The reason for the losses is not understood as of now but may be related to trigger inefficiency at negative rapidities. The cross sections for the ranges of p_T plotted in Fig. 6.2 show similar behavior as a function of rapidity. Figures 6.3 and 6.4 show the differential cross section as a function of p_T averaged over the full rapidity range ($|y| < 0.7$) for the beryllium and copper data.

Proton Beam

The differential cross section for π^0 production from incident protons as a function of p_T , averaged over seven different rapidity intervals, is shown in Fig. 6.5. As in the case for π^- beam, the rapidity intervals cover the range from

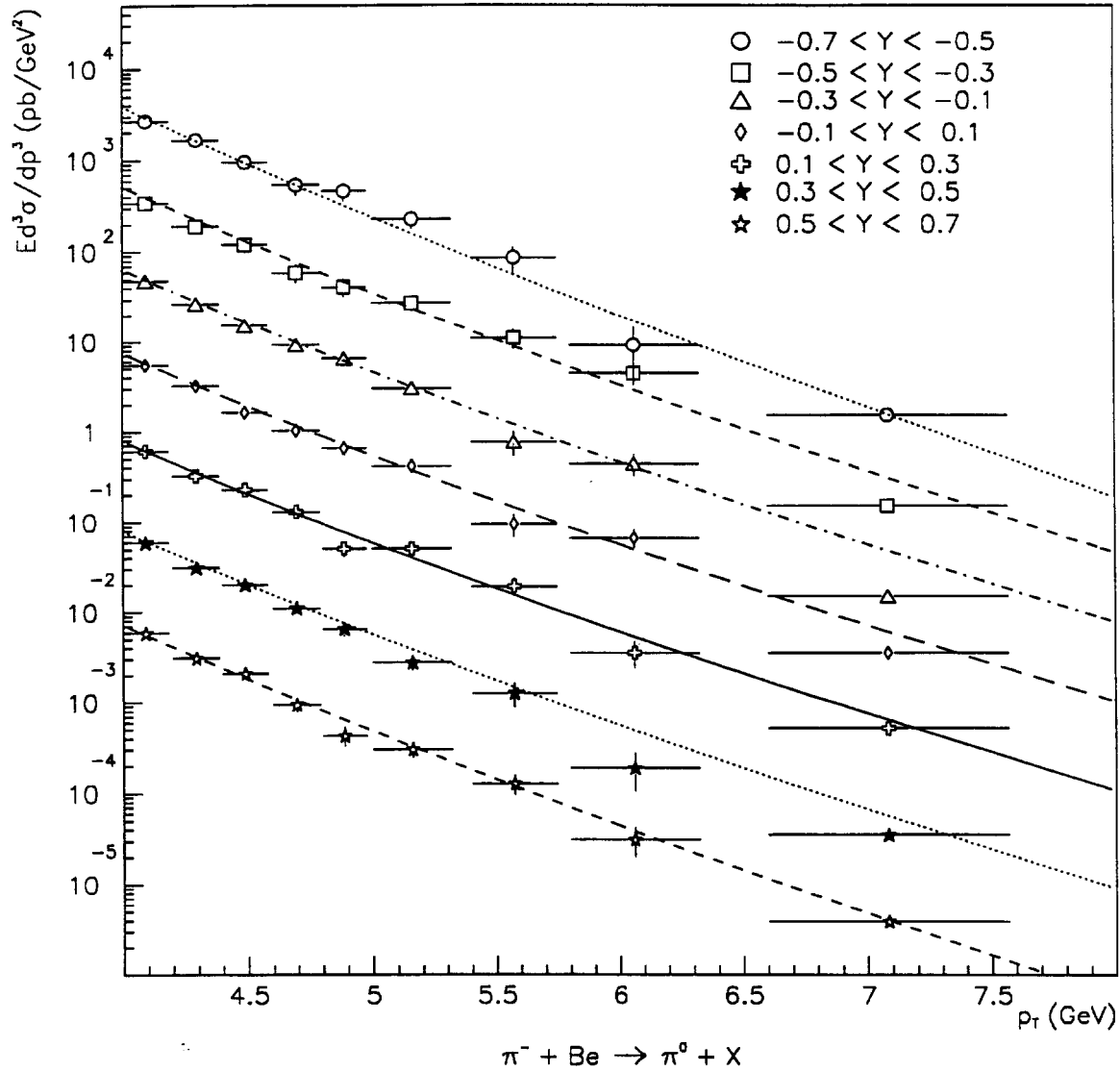


Figure 6.1 Invariant differential cross sections as functions of p_T for different rapidity intervals. The cross sections are for π^- interactions on beryllium, divided by $A_{\text{Be}} = 9$ (per nucleon). The topmost data have the correct normalization, while the rest of the y intervals have progressive shifts by factors of 10. The curves represent integrations of Eq. (6.1) over the appropriate p_T and rapidity ranges..

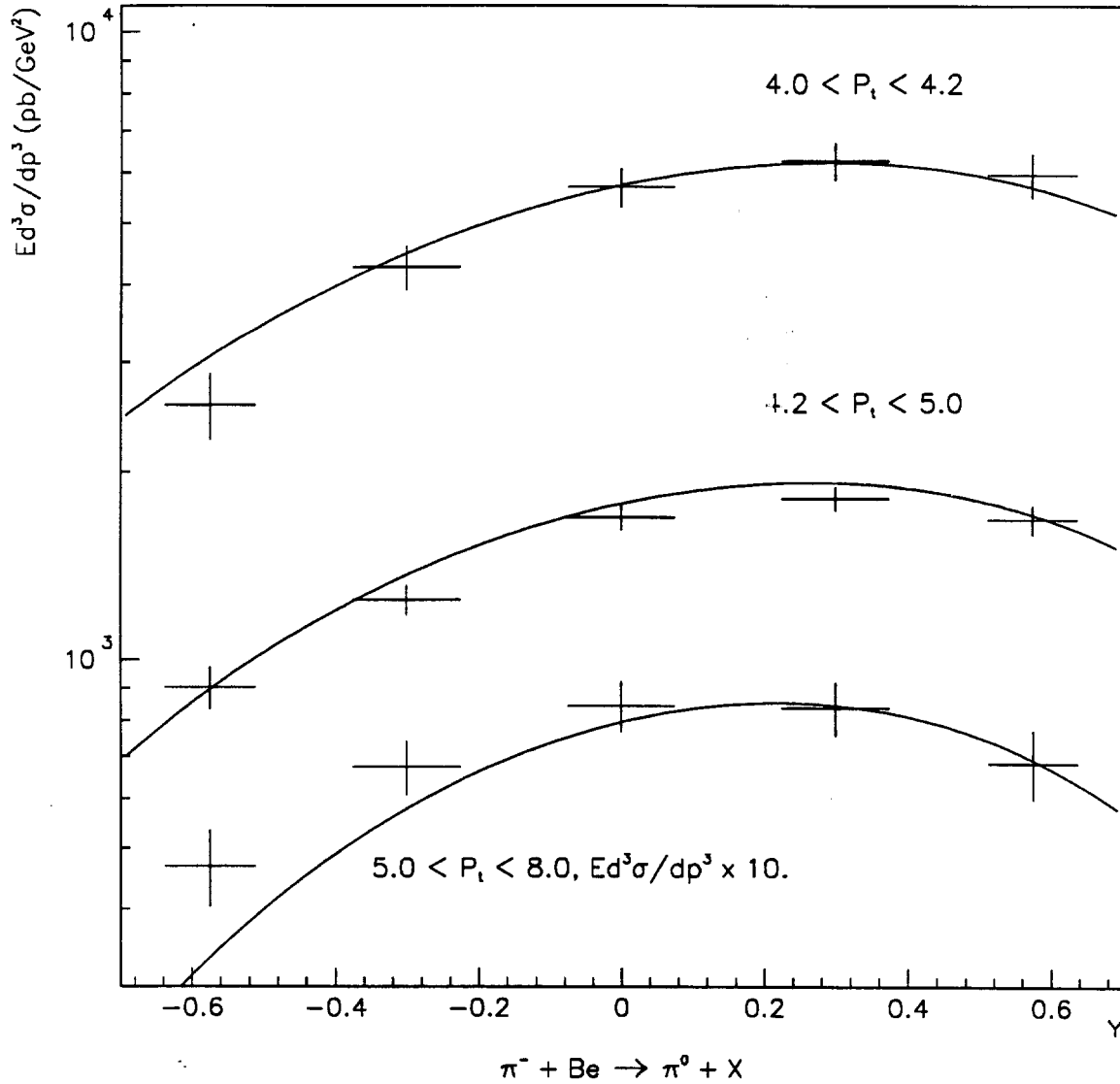


Figure 6.2 Invariant differential cross sections for π^- interactions on beryllium, divided by $A_{\text{Be}} = 9$, as functions of rapidity averaged over several p_T ranges. The cross section for p_T between 5.0 and 8.0 GeV/c has been scaled by a factor of 10. The curves represent integrations of Eq. (6.1) over the appropriate p_T and rapidity ranges.

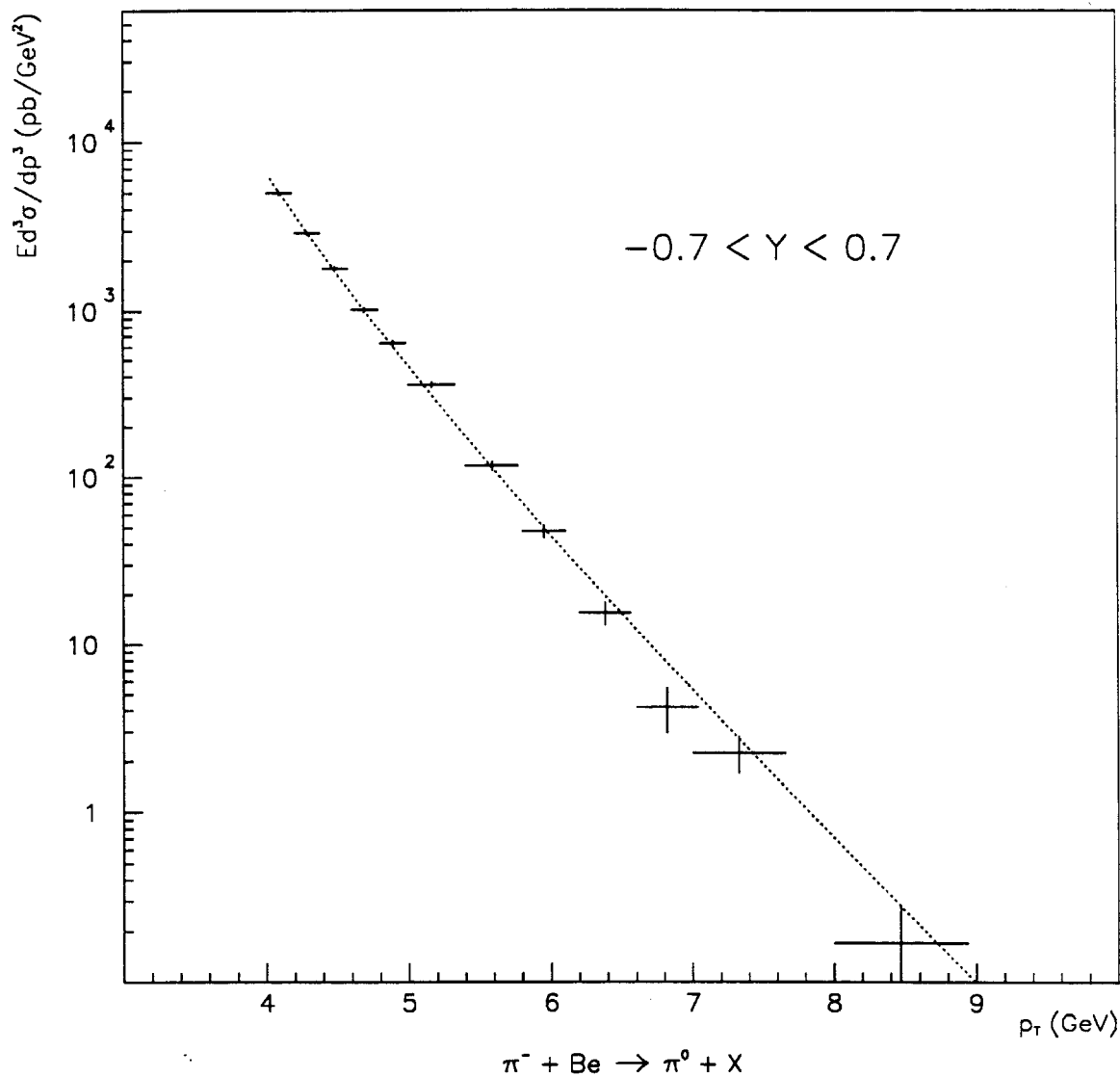


Figure 6.3 Invariant differential cross section as a function of p_T averaged over the full rapidity range. The cross section is for π^- interactions on beryllium, divided by $A_{Be} = 9.0$. The curve represents an integration of Eq. (6.1) over the appropriate p_T and rapidity ranges.

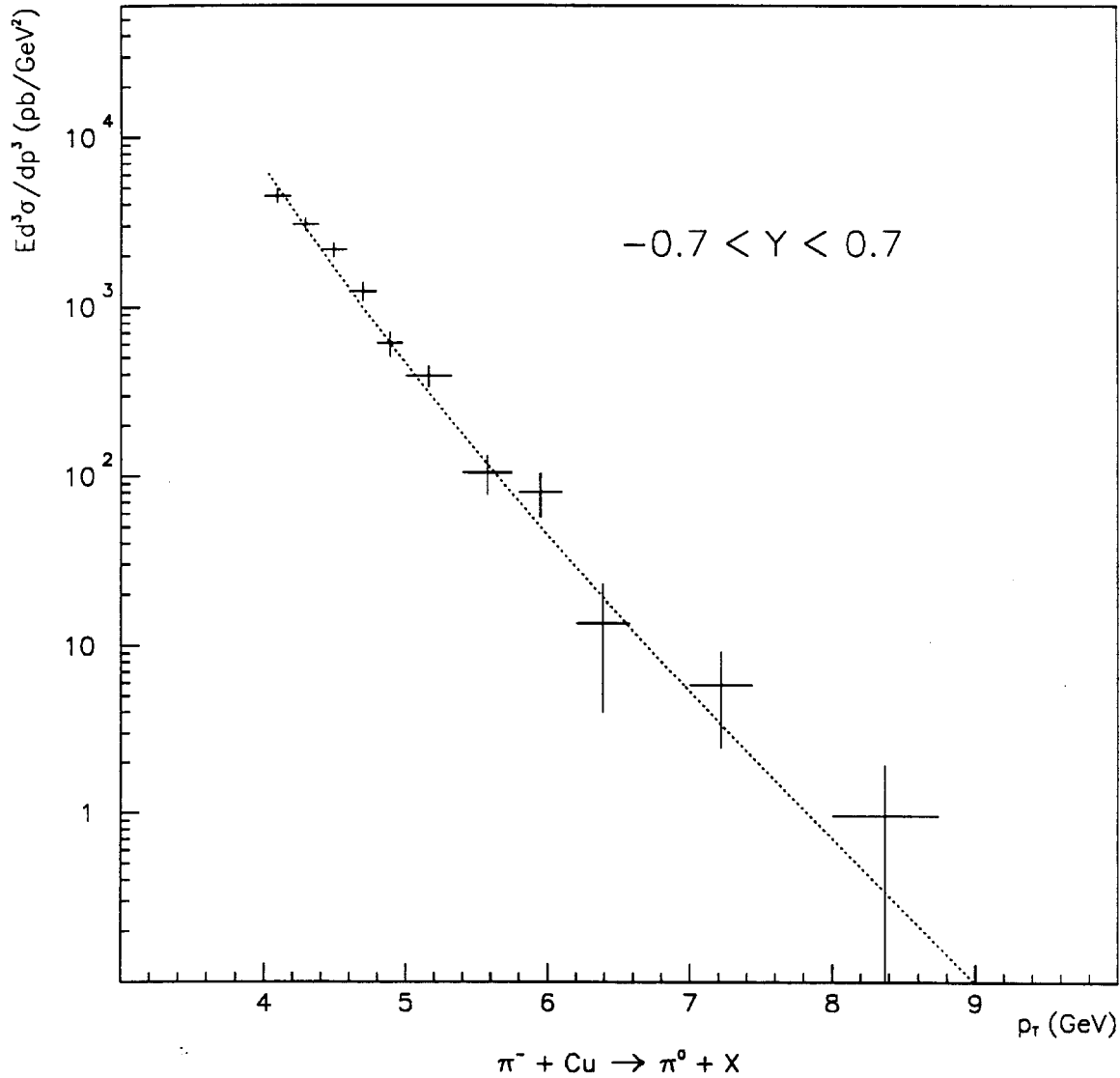


Figure 6.4 Invariant differential cross section as a function of p_T averaged over the full rapidity range. The cross section is for π^- interactions on copper, divided by $A_{\text{Cu}} = 63.5$. The curve represents an integration of Eq. (6.1) over the appropriate p_T and rapidity ranges.

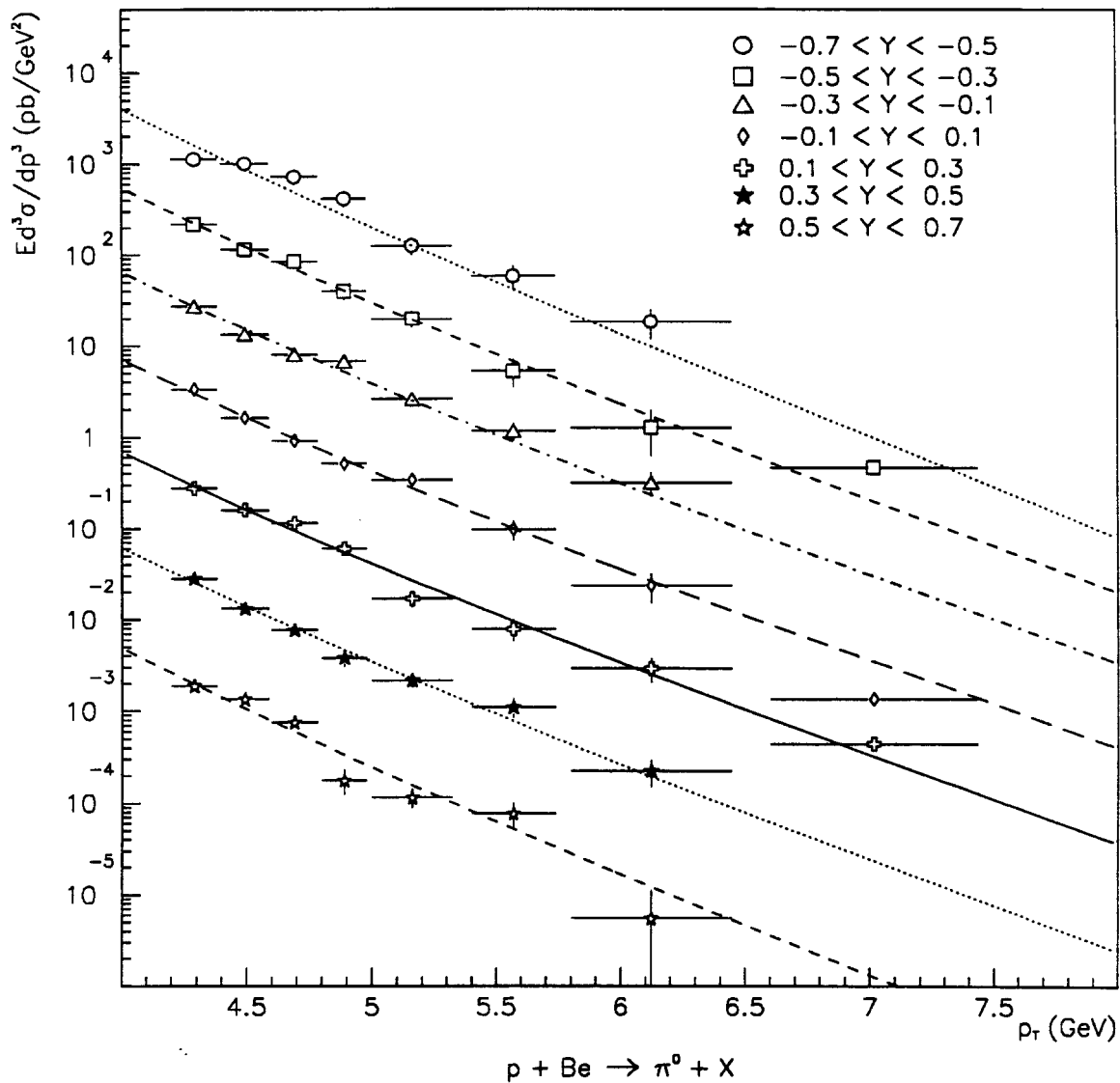


Figure 6.5 Invariant differential cross sections as functions of p_T for different rapidity intervals. The cross sections are for p interactions on beryllium, divided by $A_{\text{Be}} = 9$ (per nucleon). The topmost data have the correct normalization, while the rest of the y intervals have progressive shifts by factors of 10. The curves represent integrations of Eq. (6.1) over the appropriate p_T and rapidity ranges.

-0.7 to 0.7 in increments of 0.2 units of rapidity. Again, for clarity, vertical error bars are not shown for the last p_T points. The lines through each set of points represent the integrated fit over the respective rapidity intervals. Though statistics are somewhat more limited than in the case of negative beam, we again see no significant variations in the shape of the cross sections for different rapidity intervals.

The cross sections as functions of rapidity, averaged over four different p_T intervals, are shown in Fig. 6.6. The solid lines represent the fitted function integrated over the p_T range, plotted versus rapidity. For positive data, we have restricted p_T to greater than $4.2 \text{ GeV}/c$ because of trigger bias. Figure 6.6 indicates similar shapes of cross sections for the different p_T ranges. Figures 6.7 and 6.8 show the differential cross section as a function of p_T averaged over the full rapidity range, for the beryllium and copper targets.

6.2 NUCLEAR DEPENDENCE OF CROSS SECTIONS

The expression for the cross section per nucleon, given by Eq. (5.2), was obtained by dividing the observed cross section per nucleus by A . Previous experiments have shown that the A dependence of the cross section may vary as A^α , where α is not necessarily fixed. In order to determine α , the ratio of the measured cross section on beryllium to that on copper was examined. This ratio was then used to extract α for each p_T interval. Figures 6.9 and 6.10 show the values of α obtained for negative and positive beams.

The dependence of α on different rapidity intervals, was also examined for cross sections integrated over p_T ($4.2 \text{ GeV}/c < p_T < 8.0 \text{ GeV}/c$). The π^- data

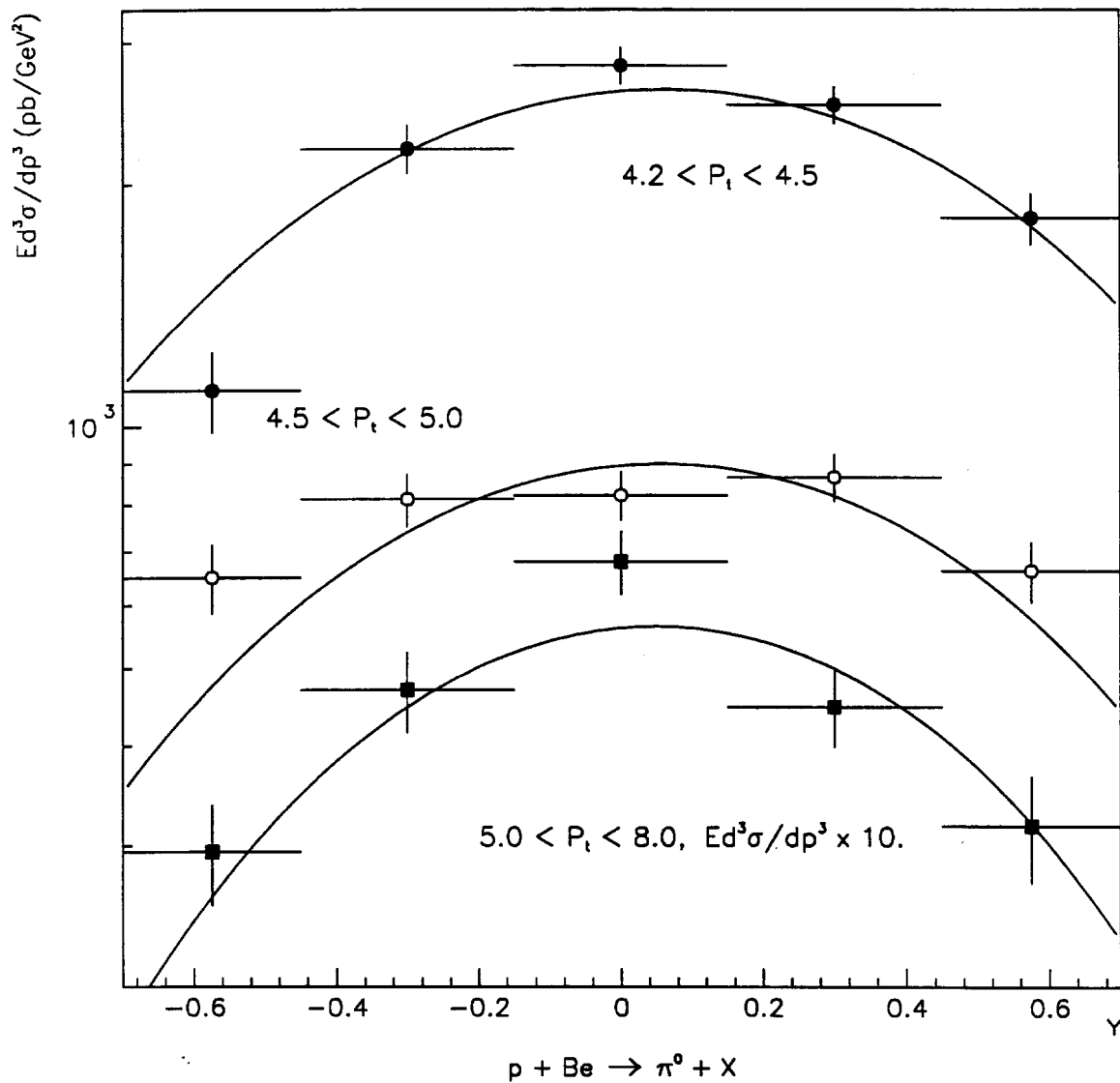


Figure 6.6 Invariant differential cross sections for p interactions on beryllium, divided by $A_{Be} = 9$, as functions of rapidity averaged over several p_T ranges. The cross section for p_T between 5.0 and 8.0 GeV/c was scaled by a factor of 10. The curves represent integrations of Eq. (6.1) over the appropriate p_T and rapidity ranges.

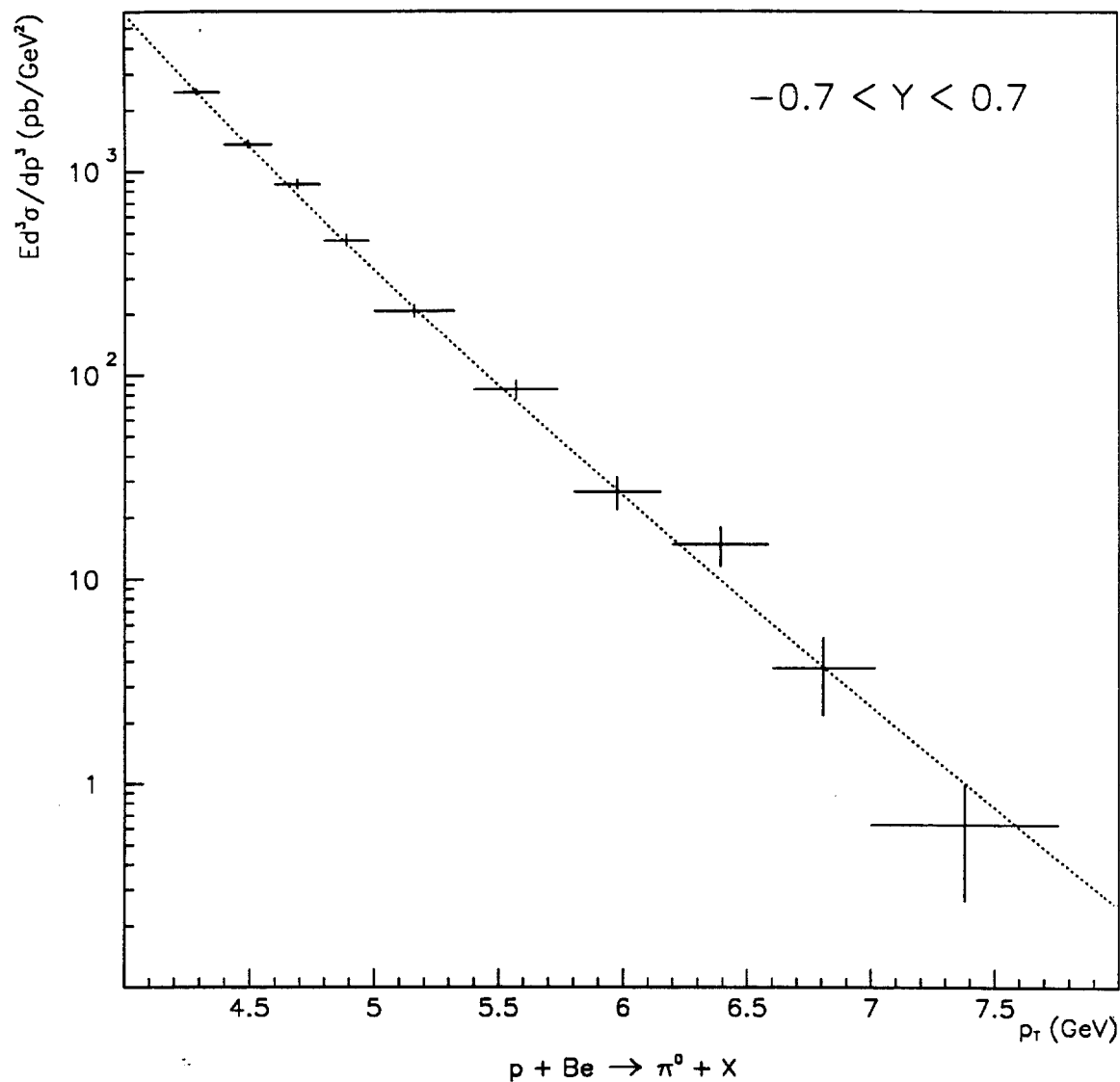


Figure 6.7 Invariant differential cross section as a function of p_T averaged over the full rapidity range. The cross section is for p interactions on beryllium, divide by $A_{\text{Be}} = 9.0$. The curve represents an integration of Eq. (6.1) over the appropriate p_T and rapidity ranges.

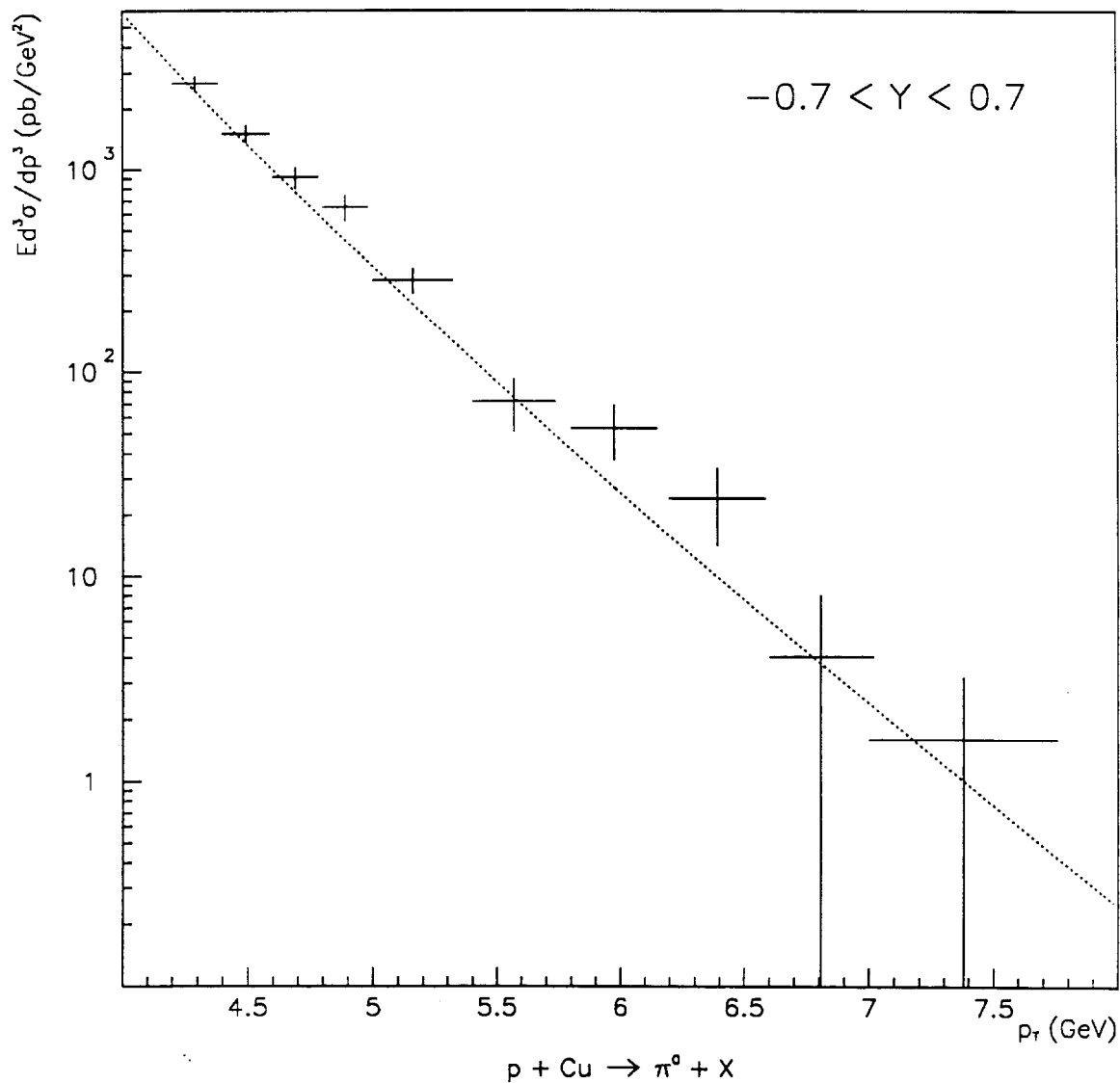


Figure 6.8 Invariant differential cross section as a function of p_T averaged over the full rapidity range. The cross section is for p interactions on copper, divide by $A_{Cu} = 63.5$. The curve represents an integration of Eq. (6.1) over the appropriate p_T and rapidity ranges.

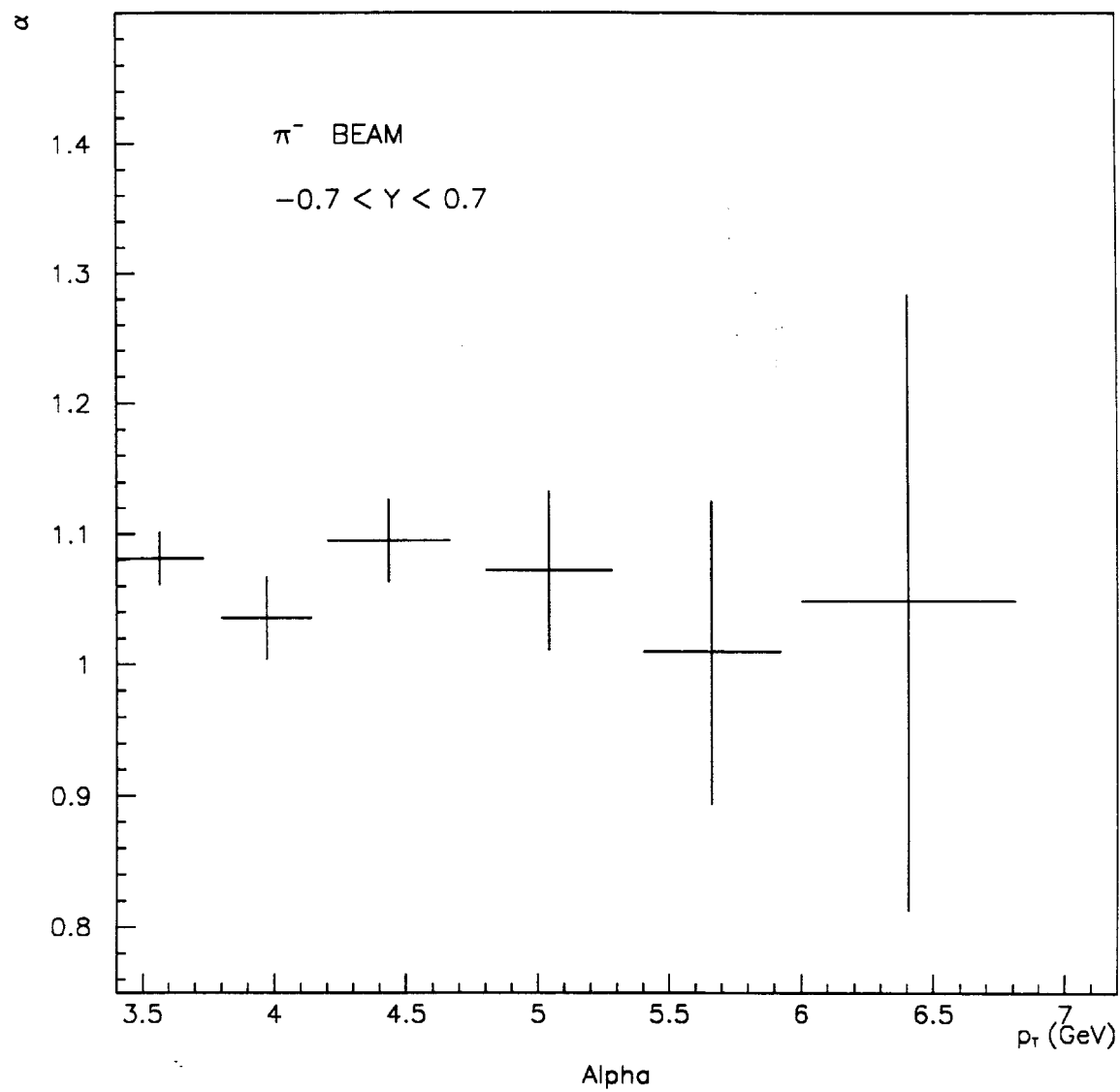


Figure 6.9 α , as a function of p_T , determined from the ratio of π^0 cross sections from π^- interactions on beryllium and copper.

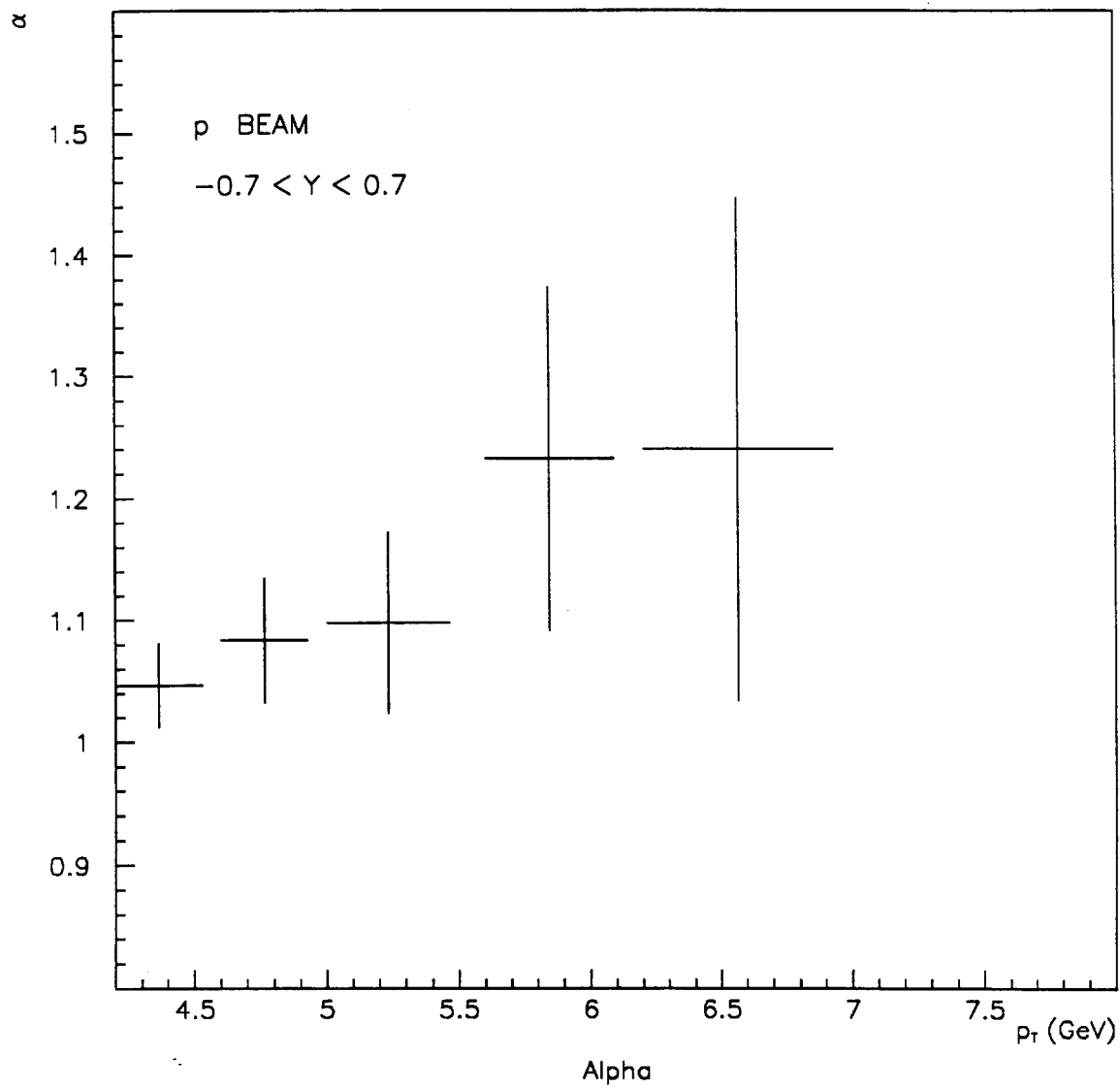


Figure 6.10 α , as a function of p_T , determined from the ratio of π^0 cross sections from p interactions on beryllium and copper.

seem to have a small systematic dependence on rapidity, while no such effect is seen in the proton data. Table 6.4 gives the values of α for three different rapidity ranges for both beams.

	$-0.7 < Y < -0.2$	$-0.2 < Y < 0.2$	$0.2 < Y < 0.7$
π^- Beam	1.168 ± 0.051	1.077 ± 0.046	1.053 ± 0.046
p Beam	1.072 ± 0.053	1.047 ± 0.043	1.078 ± 0.042

Table 6.4 α dependence on rapidity for positive and negative beams.

6.3 RATIO OF CROSS SECTIONS FOR π^- AND PROTON BEAMS

The ratio of cross sections per nucleon for incident π^- and p beams on beryllium targets is shown in Fig. 6.11. The ratio is greater than one for all p_T . A possible reason for this is that the proton has one more quark than the π^- , and consequently, each quark gets less momentum on average. Thus, quarks in the π^- would tend to produce higher p_T π^0 s than would protons. This should be particularly enhanced at larger p_T , which seems to be the trend in the data.

The π^-/p ratio has been studied for different ranges of rapidity, averaged over p_T above 4.2 GeV/c. The three rapidity ranges chosen were $-0.7 < Y < -0.2$, $-0.2 < Y < 0.2$ and $0.2 < Y < 0.7$. The values for the ratios in each region are: 1.063 ± 0.064 , 1.108 ± 0.054 and 1.408 ± 0.066 . The variation of the ratio can be understood on the basis of the rapidity dependence of the cross sections (Figs. 6.2 and 6.6). Both cross sections tend to rise by about a factor of 2 in going from -0.6 to 0.0 units of rapidity. Thus we would not expect a

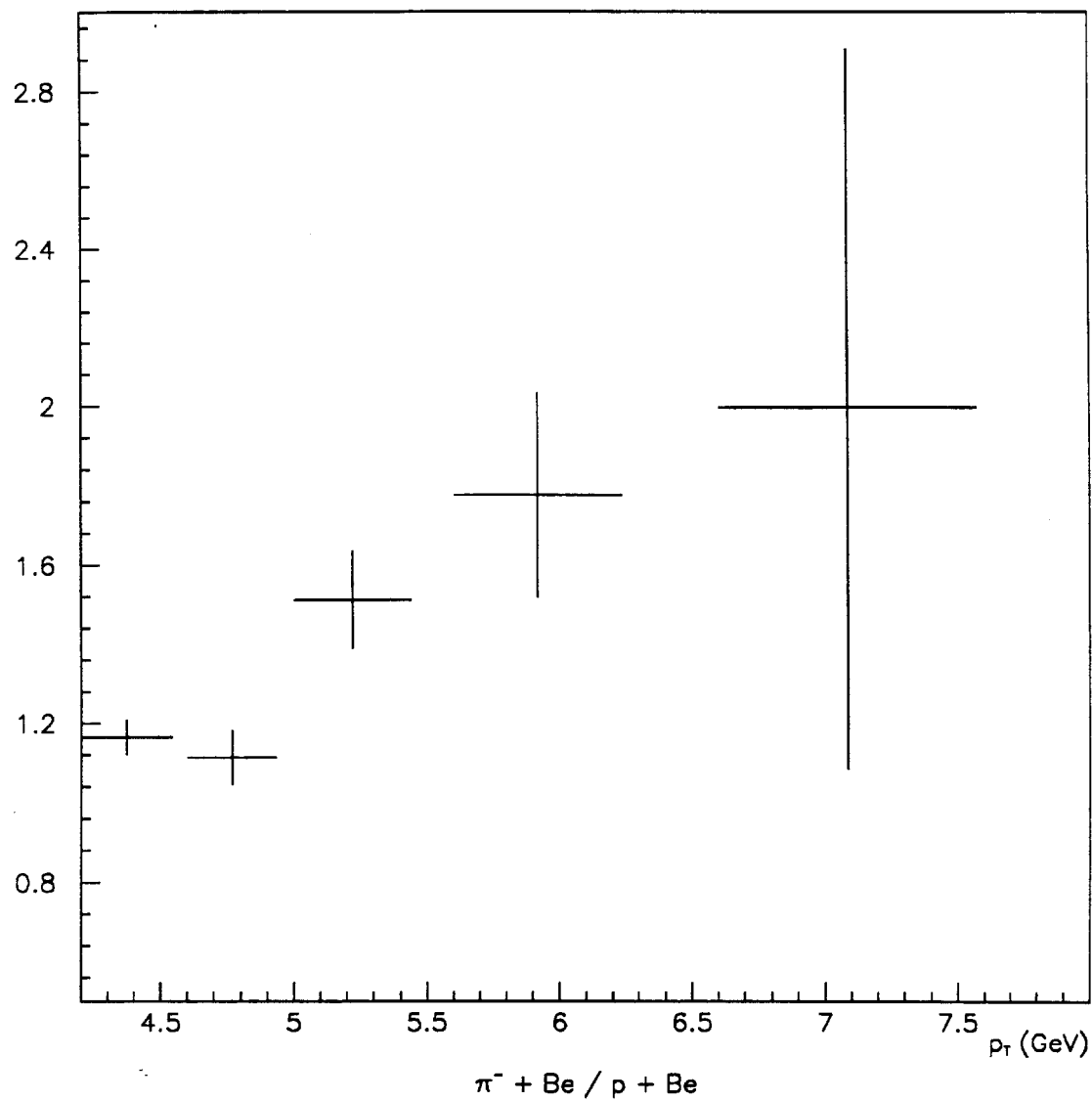


Figure 6.11 Ratio of the π^0 cross section measured from π^- interactions to that measured from p interactions. The cross sections are averaged over the full rapidity interval ($|y| < 0.7$).

significant change in the ratio between $-0.7 < Y < -0.2$ and $-0.2 < Y < 0.2$, and in fact do not see one. As we continue to move into the forward rapidity region, the proton cross section starts to drop, while the π^- continues to rise until it peaks at ~ 0.35 units of rapidity. We can therefore expect a significant increase in the ratio going from $-0.2 < Y < 0.2$ to $0.2 < Y < 0.7$, as is observed to be the case. Again, this can be attributed to the difference in the internal structure of the π^- and p.

6.4 COMPARISON TO OTHER EXPERIMENTS

Many experiments have published π^0 cross sections for various p_T and x_T ranges. Table 6.5 lists some of those experiments. The table gives the beam particle type used on a given target material, and the center of mass energy for the experiment. Also given is the p_T and rapidity range over which the experiment collected data.

Experiments E706, E629 (Ref. 37), and CP (Ref. 42 and 43) were performed at Fermilab. Experiments WA70 (Ref. 38, 39), NA24 (Ref. 40), and NA3 (Ref. 41) were performed at the CERN SPS and R806 (Ref. 44) at the CERN ISR. The data taken for incident π^- beams are plotted as a function of p_T in Fig. 6.12. As can be seen, experimental data at similar center of mass energies are in essential agreement. In order of increasing cross section, the experiments are: CP, NA3, WA70, NA24 and E706. It should be pointed out that this also follows the increasing trend in center of mass energies, as one would expect. The data from E706 and NA3 have been scaled down by A/A^α where A is the appropriate nucleus, and $\alpha = 1.073$ is the average value measured for all p_T .

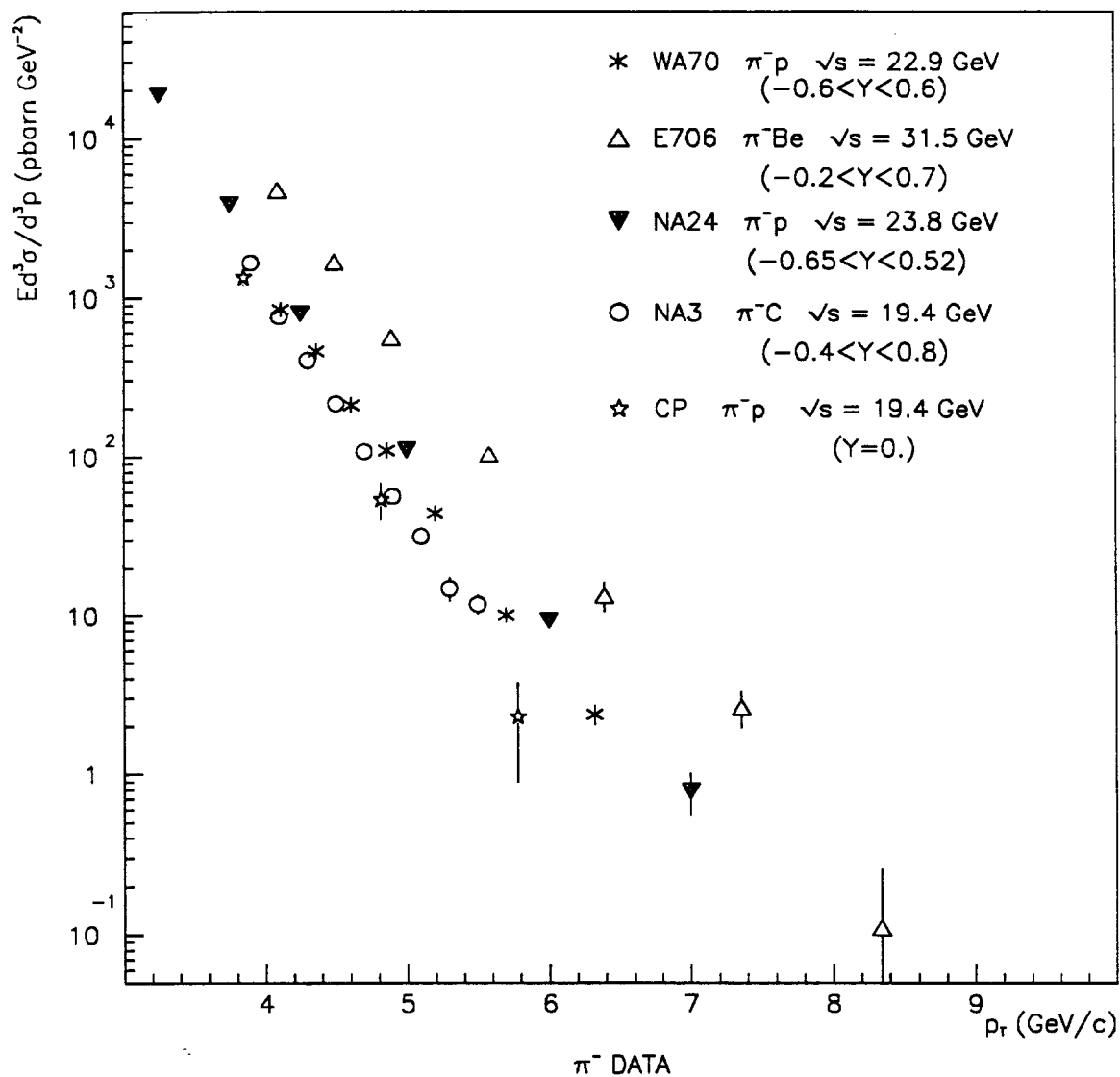


Figure 6.12 π^0 cross sections as a function of p_T , for π^- interactions, from several experiments. The magnitude of the cross section is seen to increase with increasing center of mass energy. Cross sections from nuclear targets have been scaled using the value of α previously determined.

EXP.	Beam Particle	Target	Y	p_T (GeV/c)	\sqrt{s} (GeV)
E706	π^-, K^- π^+, p	Be, Cu, Al	$-0.9 \rightarrow 0.9$	$3 \rightarrow 10$	31.5
E629 ^[37]	π^+, p	Be, C, Al	$-0.75 \rightarrow 0.2$	$2 \rightarrow 5$	20.0
WA70 ^{[38] [39]}	π^-, π^+, p	p	$-1. \rightarrow 1.$	$4 \rightarrow 7$	22.9
NA24 ^[40]	π^-, π^+, p	p	$-0.8 \rightarrow 0.8$	$1 \rightarrow 5$	23.8
NA3 ^[41]	π^-, π^+, p	C	$-0.4 \rightarrow 1.2$	$2.9 \rightarrow 6$	19.4
CP ^[42]	p	p, H ₂ , D ₂ Be, Ti, W	~ 0	$1 \rightarrow 7$	19.4, 23.8, 27.4 19.4, 23.8, 27.4
CP ^[43]	π^-	H, Be Cu, W	~ 0	$1 \rightarrow 7$	19.4, 23.8
R806 ^[44]	p	p	~ 0	$6.5 \rightarrow 15$	52.7, 62.4

Table 6.5 Selected experiments to have published π^0 production cross sections.

For beryllium this reduces the cross section per nucleon by $\sim 15\%$ relative to division by $A = 9$.

To properly compare data at different energies, one should plot the cross sections as a function of a scaling variable such as x_T , in the hope of eliminating any energy dependence. A trial function used to compare data at different \sqrt{s} , similar in form to relation (6.1), is:

$$E \frac{d\sigma}{d^3p} = C (x_T^2 + a)^{j/2} \frac{(1 - x_D)^n}{p_T^k} \quad (6.3)$$

where the parameters are defined as in relation (6.1). The major difference is the addition in the first term. Here, a dependence on the center of mass energy, via the variable x_T , has been added to alter the magnitude of the cross section, and

a parameter a has been added to constrain the dependence at low x_T . Figure 6.13 shows the data plotted as a function of x_T . The cross section is multiplied by p_T^k to extract a possible dependence on x_T . The smooth curve represents the cross section given by relation (6.3), using a best guess for the parameters. A fit was not done because systematic errors for each experiment were not available. The parameters used for this are: $C = 2.0 \times 10^9 \text{ pbarn/GeV}^2$, $a = 0.5$, $j = -1.1$, $n = 5.5$ and $k = 8.5$.

π^0 cross sections from experiments using proton beams are plotted in Fig. 6.14 as a function of p_T . Once again, we see the increase in cross section with larger center of mass energies. As in the case for negative-beam data, experiments E706, NA3, and E629 were scaled by A/A^α where $\alpha = 1.072$ for the proton beam. Figure 6.15 shows the data plotted as a function of x_T and overlaid with relation (6.3), as before. In this case, the parameters have the values: $C = 4.0 \times 10^9 \text{ pbarn/GeV}^2$, $a = 0.4$, $j = -1.1$, $n = 7.5$ and $k = 9.0$. All the data are consistent with one another except for the data published by R806. The R806 data lie above the rest of the data; with the data set at $\sqrt{s} = 62.4 \text{ GeV}$ above the set taken at $\sqrt{s} = 52.7 \text{ GeV}$. This is due to the fact that cross sections do not scale with \sqrt{s} , but have a Q^2 dependence as stated in Chapter 1.

6.5 COMPARISON WITH PHENOMENOLOGICAL PREDICTIONS

Owens (Ref. 5) has written a program which integrates inclusive differential cross sections for hadron production using the leading-log approximation (Eq. 1.7). Structure functions and fragmentation functions are needed to carry out such integrations. We have used the standard Duke-Owens^[45] set 1 for the

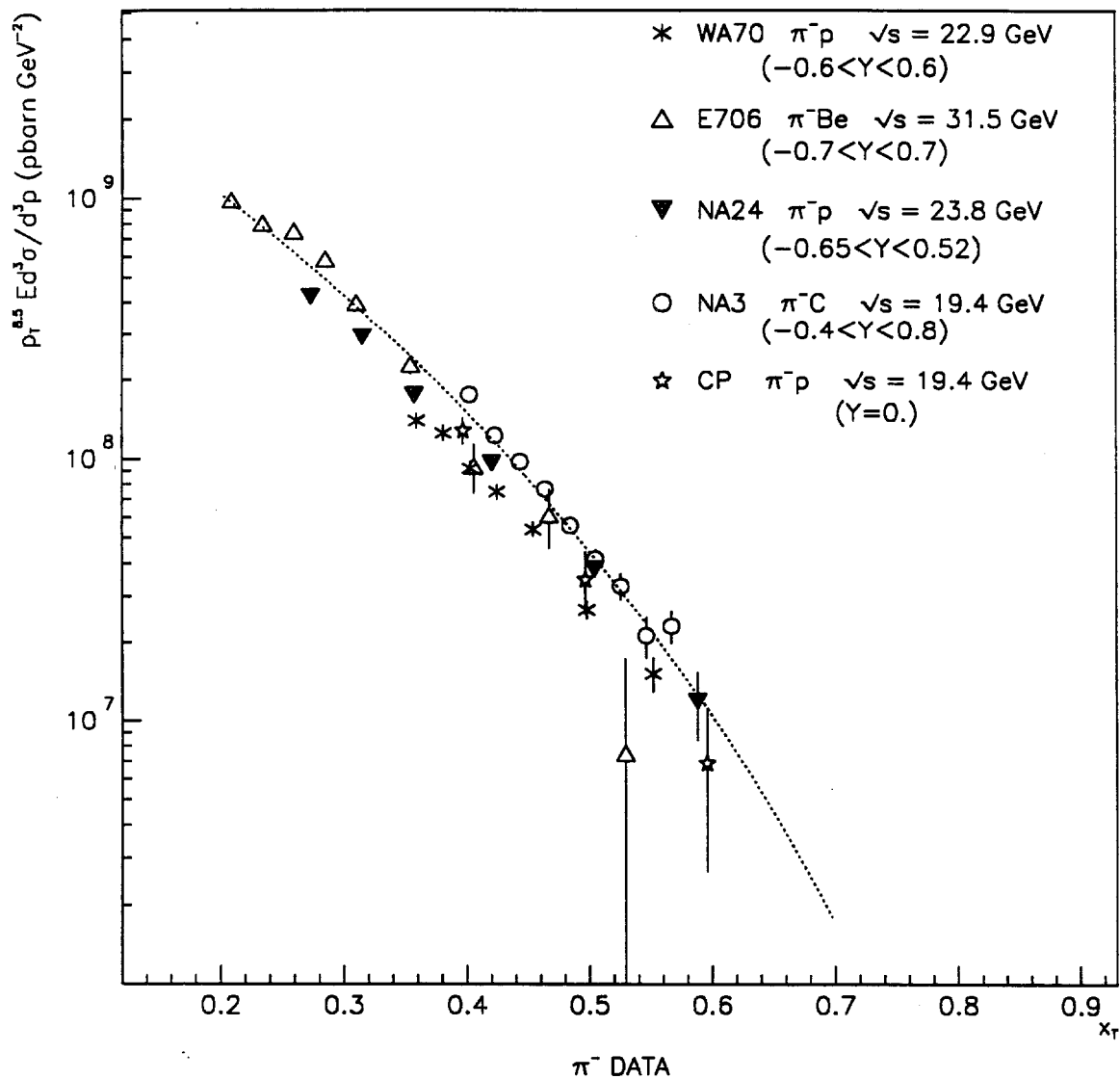


Figure 6.13 π^0 cross sections as a function of x_T , for π^- interactions, from several experiments. Cross sections from nuclear targets have been scaled using the value of α previously determined. The curve represents Eq. (6.3), with the parameters listed in the text.

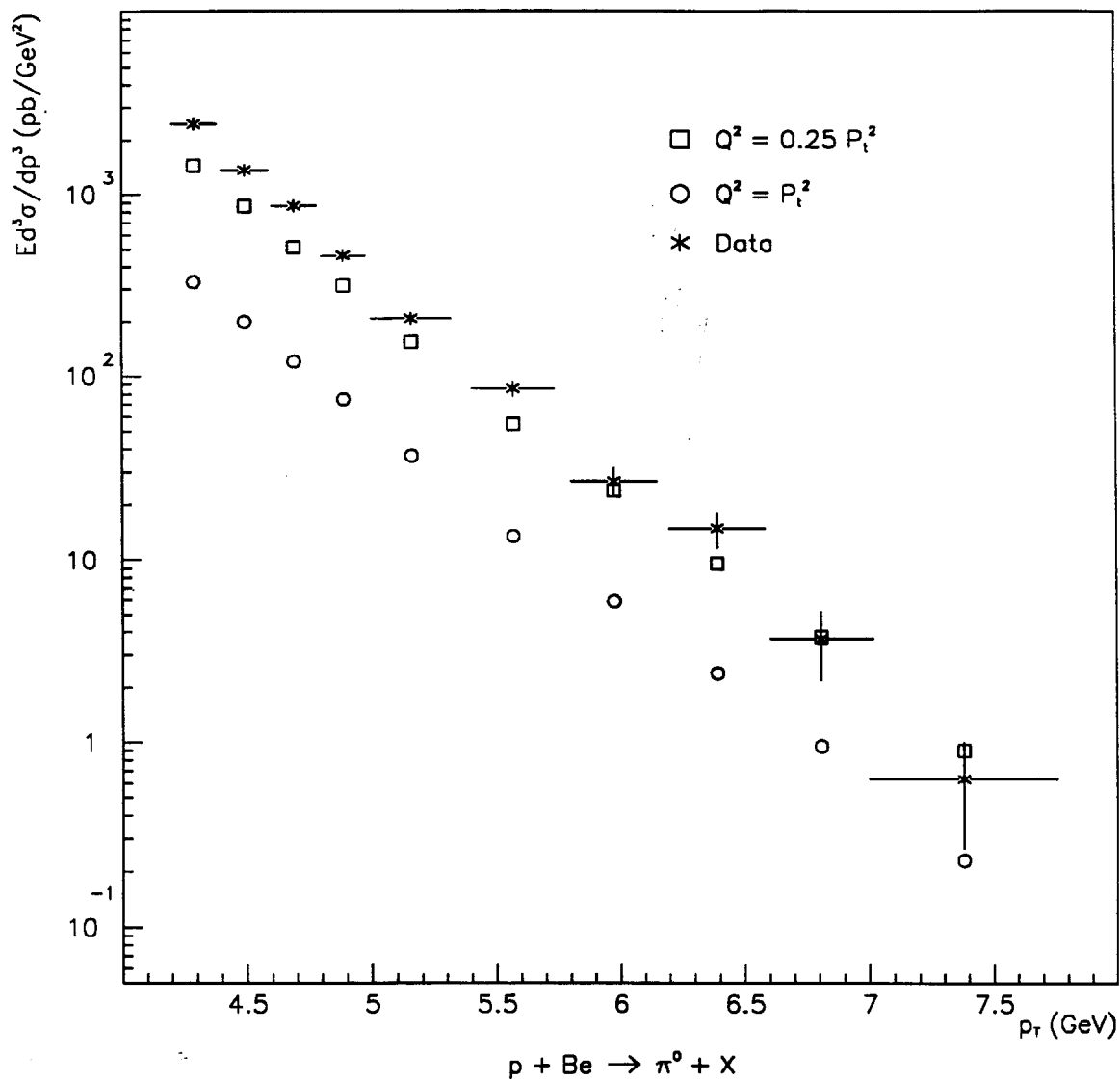


Figure 6.18 Comparison of π^0 data from p interactions on Be to that predicted from the integration of Eq. (1.7). Duke-Owens set 1 for nucleons and Owens set 1 for pions were used with $\Lambda = 200$ MeV. Two choices of Q^2 are used to compare to data.

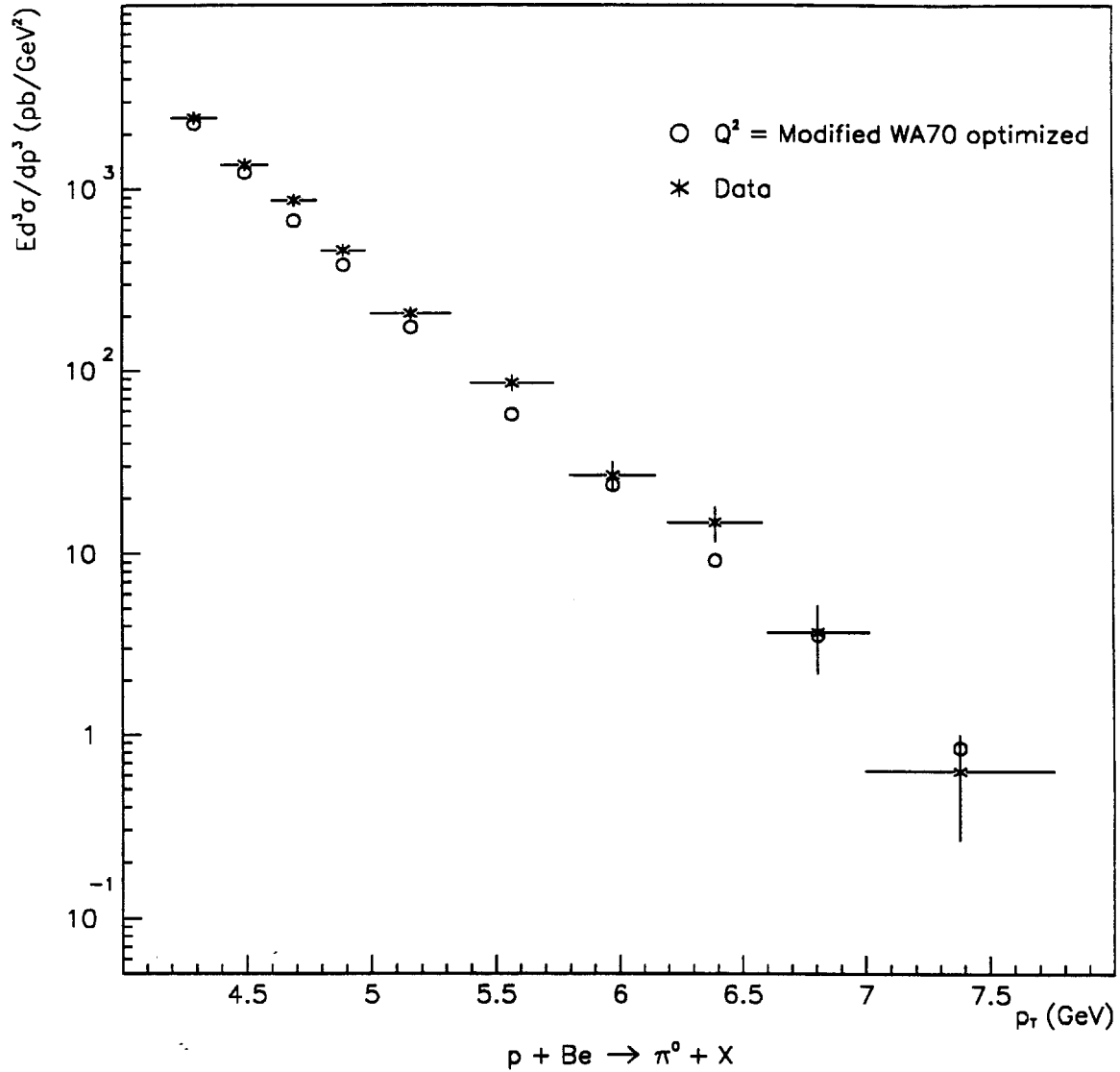


Figure 6.19 Comparison of π^0 data from p interactions on Be to that predicted from the integration of Eq. (1.7). Duke-Owens set 1 for nucleons and Owens set 1 for pions were used with $\Lambda = 200 \text{ MeV}$. A modified version of the WA70 optimized Q^2 was used.

values of α in our kinematic range are: 1.073 ± 0.014 for π^- interactions and 1.072 ± 0.026 for proton interactions.

The ratio of the cross sections for π^- and p interactions rises with increasing p_T , as expected based on the number of quarks contained within each beam particle. The ratio depends on the rapidity interval chosen. This rapidity dependence can be explained by the fact that the cross sections for each beam particle peak at different values of rapidity, again, as expected from the constituent structure of the hadrons.

Comparison with other experiments indicates that all measured cross sections, after correcting for an A^α dependence for nuclear targets, lie near a common curve, indicating good agreement between experiments, and a phenomenological form of scaling over some energy range.

The data were also compared to leading-log predictions from QCD. Since the form of the momentum transfer scale is not determined by theory, several functions were examined. The results indicate that a p_T^2 dependence on Q^2 can be chosen that yields agreement with the data. This, in itself, is not entirely reassuring since the form of Q^2 (Eq. 6.4) is not very intuitive. It is hoped that forthcoming higher-order corrections will constrain the dependence of the cross section on different momentum scales, much as was the case for direct photon calculations.

Finally, we anticipate that the next run of E706 will provide a factor of over 10 in data. The improvements in statistics will allow a more detailed comparison with QCD and extraction of hadron fragmentation functions and structure functions. This comparison will be of particularly great interest once

the next-to-leading-log calculations for jet production become available.

REFERENCES

1. M. R. Pennington, *Rep. Prog. Phys.* **46**, 393 (1983)
2. R. K. Ellis, 1987 Theoretical Advanced Study Institute, Sante Fe, New Mexico, July 1987, Fermilab preprint 79507
3. S. D. Ellis, 1987 Theoretical Advanced Study Institute, Sante Fe, New Mexico, July 1987, Fermilab preprint 79556
4. E. Reya, Lectures given at the Herbstschule fur Hochenergiephysik, Maria Laach, Sept. 1978, DESY 79/88 DO-TH 79/20
5. J. F. Owens, *Rev. of Mod. Phys.* **59**, 465 (1987)
6. T. Ferbel and W. R. Molzon, *Rev. of Mod. Phys.* **56**, 181 (1984)
7. T. Ferbel, Physics in Collision, Capri, Italy, 1988, UR Preprint 1097, Proceedings to be published, P. Strolin ed.
8. L. Camilleri, 19th Symposium on Multiparticle Dynamics, Arles, France, June 1988, World Scientific Pub. Co., D. Schiff and J. Tran Thanh Van eds.
9. M. Gell-Mann, *Phys. Lett.* **8**, 214 (1964)
10. G. Altarelli and G. Parisi, *Nucl. Phys.* **B126**, 298 (1977)
11. M. Zielinski, Private communication.
12. P. Aurenche, A. Douiri, R. Baier, M. Fontannaz and D. Schiff, *Phys. Lett.* **140B**, 87 (1984)
13. P. Aurenche, R. Baier, M. Fontannaz and D. Schiff, *Nucl. Phys.* **B286**, 509 (1987)

14. P. Aurenche, R. Baier, A. Douiri, M. Fontannaz and D. Schiff, *Nucl. Phys. B* **286**, 553 (1987)
15. P. Aurenche, R. Baier, M. Fontannaz and D. Schiff, *Nucl. Phys. B* **297**, 661 (1988)
16. F. Aversa, P. Chiappetta, M. Greco and J. Ph. Guillet, *Phys. Lett.* **210B**, 225 (1988) and, *Phys. Lett.* **211B**, 465 (1988).
17. H. J. Frisch, et al., *Phys. Rev. D* **27**, 1024 (1983)
18. A. Lanaro, π^0 Production with K^- and π^+ Beams at 530 GeV/c, PhD Dissertation, University of Rochester (1989)
19. C. Lirakis, A study of High Transverse Momentum η production in 530 GeV/c Hadronic Interactions, PhD Dissertation, Northeastern University (1989)
20. M. Glaubman, Internal E706 note #144, Jan. 1986
21. W. DeSoi, Construction and Operation of a Liquid Argon Calorimeter for use in the High Energy Experiment E-706 at the Fermi National Accelerator Laboratory, PhD Dissertation, University of Rochester (1989)
22. P. Lukens, Internal E706 Note #141, Dec. 1985
23. C. Fabjan, in *Experimental Techniques in High Energy Physics*, Addison-Wesley Publishing Company 1987, T. Ferbel ed.
24. Review of Particle Properties, 1988
25. W. Hoffmann et. al., *Nucl. Instr. and Meth.* **135**, 151 (1976)
26. VAXONLINE System, FNAL Computer Department publication PN 252

27. C. Yosef, High Transverse Momentum Neutral Pion Production in Hadronic Interactions, PhD Dissertation, Northeastern University (1989)
28. D. Skow, η production from 530 GeV/c Hadron Beams, PhD Dissertation, University of Rochester (1989)
29. H. J. Klein and J. Zoll, PATCHY reference manual, CERN Computer Centre program library Oct. 1983
30. ACP Software User's Guide for Event Oriented Processing, FNAL Computer Department publication #GA0001.
31. R. Brun, M. Goossens and J. Zoll, ZEBRA user guide, CERN Computer Centre program library DD/EE/85-6
32. J. Zoll, ZEBRA reference manuals, CERN Computer Centre program library
33. S. Easo, Structure of Events Containing a Direct Photon or Neutral Pion in Hadronic Interactions, PhD Dissertation, Pennsylvania State University (1989)
34. R. Brun, F. Bruyant, M. Maire, A. C. McPherson and P. Zancarini, GEANT3 User's Guide, CERN Data Handling Division, DD/EE/84-1, 1987
35. E. Prebys, Private communication.
36. A. Sinanidis, Particles Produced in Association with High Transverse Momentum Single Photons and π^0 s in Hadronic Collisions, PhD Dissertation, Northeastern University (1989)

37. J. Polvis, A Measurement of Neutral Meson and Direct Photon Production at Large Transverse Momentum, PhD Dissertation, University of Minnesota (1984)
38. M. Bonesini et. al., *Z. Phys. C* **37**, 39 (1987)
39. M. Bonesini et. al., *Z. Phys. C* **38**, 371 (1988)
40. C. De Marzo et. al., *Phys. Rev. D* **36**, 16 (1987)
41. J. Badier et. al., *Z. Phys. C* **30**, 45 (1986)
42. C. Antreasyan et al., *Phys. Rev. D* **19**, 764 (1979)
43. H. Frisch et al., *Phys. Rev. D* **27**, 1001 (1983)
44. C. Kourkouvelis et. al., *Phys. Lett.* **84B**, 271 (1979)
45. D. W. Duke and J. F. Owens, *Phys. Rev. D* **30**, 49 (1984)
46. J. F. Owens, *Phys. Rev. D* **30**, 943 (1984)
47. J. F. Owens, *Phys. Rev. D* **19**, 3279 (1979)
48. H.-U. Bengtsson and T. Sjöstrand, Pythia version 4.8, CERN LU TP 87-3, Jan. 1987
49. H.-U. Bengtsson and G. Ingelman, *Comp. Phys. Comm.* **34**, 251 (1985)